**João Miguel
Gomes de Sousa**

**Estudos de Monte Carlo de transições de fase e
adsorção: Aplicação a sistemas de Lennard-Jones
n-6, C_{60} e zeólitos**

**Monte Carlo studies of phase transitions and
adsorption: Application to n-6 Lennard-Jones, C_{60}
and zeolite systems**

João Miguel Gomes de Sousa

Estudos de Monte Carlo de transições de fase e adsorção: Aplicação a sistemas de Lennard-Jones n-6, C_{60} e zeólitos

Monte Carlo studies of phase transitions and adsorption: Application to n-6 Lennard-Jones, C_{60} and zeolite systems

Dissertação apresentada à Universidade de Aveiro para cumprimento dos requisitos necessários à obtenção do grau de Doutor em Física, realizada sob a orientação científica do Doutor António Luís Campos de Sousa Ferreira, Professor Associado do Departamento de Física da Universidade de Aveiro.

para os meus pais

o júri / the jury

presidente / president

Prof. Doutor Aníbal Guimarães da Costa
professor catedrático da Universidade de Aveiro

vogais / examiners committee

Prof. Doutor Jorge Manuel dos Santos Pacheco
professor catedrático da Escola de Ciências da Universidade do Minho

Prof.ª Doutora Maria Augusta Oliveira Pereira dos Santos
professora associada da Faculdade de Ciências da Universidade do Porto

Prof. Doutor António Luís Campos de Sousa Ferreira
professor associado da Universidade de Aveiro

Prof. Doutor Paulo Ivo Cortez Teixeira
professor adjunto com agregação do Instituto Superior de Engenharia de Lisboa

Prof. Doutor Manuel António dos Santos Barroso
professor auxiliar da Universidade de Aveiro

agradecimentos

Agradeço ao meu orientador, António Luís Ferreira, pelo papel que desempenhou na minha formação e a disponibilidade e abertura, pessoal e profissional, que demonstrou ao longo destes anos.

Agradeço a todos com quem colaborei e que contribuíram, em vários momentos, para que este trabalho pudesse existir. Em particular ao professor Barroso, à professora Elby Titus e ao Mário Mira.

Agradeço aos organizadores, docentes e colegas do programa doutoral MAP-Fis, pela oportunidade concedida de participar nesta experiência enriquecedora.

Agradeço aos amigos que me acompanharam neste processo, principalmente ao Cláudio, Rosa, Carlos, Teresa, Narciso e Tiago, mas sem esquecer todos os outros que mereciam muito mais do que umas reticências. Uma palavra de apreço para o Francisco Reis, sem o qual as viagens à impressora do 3º andar teriam sido muito mais aborrecidas.

Agradeço aos meus pais e aos meus irmãos, por razões que ficam além do que consigo descrever. E aos meus sobrinhos só por serem adoráveis.

Por fim, sem querer minimizar as contribuições já referidas, não consigo deixar de achar que uma palavra de agradecimento não é, por vezes, suficiente, por isso deixo duas. *Muito* obrigado, Susana.

palavras-chave

Métodos de Monte Carlo, transição sólido-fluido, energia livre, Lennard-Jones n-6, adsorção de hidrogénio, zeólitos, fulerenos, C_{60}, transição de fase rotacional.

resumo

Neste trabalho, as propriedades da transição sólido-fluido do sistema de Lennard-Jones n-6 são determinadas recorrendo a cálculos intensivos de energias livres. Vários valores do parâmetro n que regula a intensidade da interacção repulsiva do potencial são investigados. As energias livres dos sistemas com $n < 12$ são calculadas usando o sistema com $n = 12$ como referência, recorrendo a uma generalização do método dos histogramas que permite combinar simulações canónicas independentes realizadas com diferentes Hamiltonianos e calcular diferenças de energia livre entre elas. O comportamento de fases do sistema de fulerenos C_{60} é investigado a partir de simulações de Monte Carlo *NPT* e utilizando uma classe de potenciais atomísticos que consideram cada átomo da molécula como um centro de interacção distinto. Adicionalmente, podem incluir cargas parciais localizadas nas ligações interatómicas. Em particular, a transição de uma fase com ordem orientacional para uma fase rotacionalmente livre, que acontece com o aumento da temperatura, é estudada em função da pressão. A adsorção de hidrogénio no zeólito NaA é simulada numa gama alargada de temperaturas e pressões recorrendo ao algoritmo de Monte Carlo no ensemble macrocanónico. Os resultados são comparados com dados experimentais. É utilizado um potencial que incluiu termos de van der Waals, Coulomb e de polarização induzida devido à presença de um campo eléctrico permanente no zeólito.

abstract The solid-fluid transition properties of the n-6 Lennard-Jones system are studied by means of extensive free energy calculations. Different values of the parameter n which regulates the steepness of the short-range repulsive interaction are investigated. Furthermore, the free energies of the $n < 12$ systems are calculated using the $n = 12$ system as a reference. The method relies on a generalization of the multiple histogram method that combines independent canonical ensemble simulations performed with different Hamiltonians and computes the free energy difference between them.

The phase behavior of the fullerene C_{60} solid is studied by performing *NPT* simulations using atomistic models which treat each carbon in the molecule as a separate interaction site with additional bond charges. In particular, the transition from an orientationally frozen phase at low temperatures to one where the molecules are freely rotating at higher temperatures is studied as a function of applied pressure.

The adsorption of molecular hydrogen in the zeolite NaA is investigated by means of grand-canonical Monte Carlo, in a wide range of temperatures and imposed gas pressures, and results are compared with available experimental data. A potential model is used that comprises three main interactions: van der Waals, Coulomb and induced polarization by the permanent electric field in the zeolite.

Contents

Chapter 1

Introduction

The first computer simulation of a dense liquid dates back to the seminal work of Metropolis, Rosenbluth, Rosenbluth, Teller and Teller [1], who in 1953, while working at the Los Alamos laboratory, introduced the Metropolis Monte Carlo (MC) algorithm. In the original work, the aim was to solve the problem of drawing important samples from the Boltzmann distribution, which describes a system of a fixed number of classical particles at constant temperature and volume. If it could do so, then the properties of the system at these conditions could be inferred by looking only at a limited number of statistically relevant samples.

In order to draw from a generic high dimensional distribution $\rho(x)$, the algorithm defines a stochastic dynamic which generates, iteratively, a Markov chain of states whose distribution approximates $\rho(x)$, for sufficiently long times. More so, it does not require the full knowledge of $\rho(x)$, but merely that the ratio between the probability of two states, $\rho(x_1)/\rho(x_0)$, can be computed. This aspect is crucial since obtaining the normalizing factor of $\rho(x)$ is often impossible in practice, and indeed most times equates to solving the whole problem. For instance, the normalizing factor in the Boltzmann distribution is the canonical partition function or, equivalently, the Helmholtz free energy, which, if known *a priori,* would immediately give pressures, chemical potentials or other relevant thermodynamic quantities, or would allow solving phase stability problems in a trivial way.

Much has changed in the world of both science and, perhaps more drastically, computers, since the 1950s. Remarkably, the MC algorithm has remained fundamentally the same, and is in widespread use even today. This is not surprising. The method is simple, flexible and provides essentially exact results for problems in statistical physics. Which is not to say that no room was left for innovation in the field, rather the opposite. Alternative and complementary techniques have been devised over the years which extend the range of applicability of the method and attempt to solve some of its limitations.

Extensions were soon proposed that saw the application of the algorithm to new statistical ensembles, such as the isothermal-isobaric [2] or the grand-canonical ensembles [3], both of which are applied to investigate separate problems in this thesis. The former is used to study

closed systems at constant pressure and temperature, a natural choice which replicates the conditions of most real world experiments, while the latter imposes a temperature and volume while allowing the system to exchange particles with a reservoir at a fixed chemical potential.

Significant effort has been devoted to the development of alternative methods to overcome some efficiency problems of the original algorithm. In some situations, biased MC methods are a good way to accelerate the convergence of the chain. In essence, these algorithms introduce a bias in the state perturbation scheme that leads to states being generated which are *a priori* more likely to be accepted. For instance, virial bias Monte Carlo [4, 5] is a variation of the isothermal-isobaric MC algorithm where the new proposed volume is biased by the virial sum. In Hybrid Monte Carlo [6, 7], in every step, a whole new configuration is created by giving the particles random initial velocities, computing its forces and solving the equations of motion in a small timestep, essentially performing a mini MD simulation every time. The Boltzmann weights of the starting and final configurations are used to accept or reject the proposal and corrections must be included to account for the non-uniform selection of states.

A different approach is taken by methods which use non-Boltzmann sampling, a class of algorithms which has received significant attention in the last decades. The idea is to draw samples from distributions other than the ensemble distribution, which potentially allows the system to visit a wider region of phase space (the multidimensional space of variables that define the state of the particles in the system). Examples of methods which are, in one way or another, built on this premise include umbrella sampling [8, 9], replica exchange MC [10, 11, 12], multicanonical ensemble [13, 14] or transition matrix MC [15, 16]. The scope of these methods and their applications is vast but this subject is not expanded further in this thesis, which deals exclusively with Boltzmann sampling.

The main limitation of the traditional Monte Carlo method is actually a testament to how well it handles the problem it sets out to solve: keep the sampling limited to the important states in a distribution. This restricts the evolution of the system to those regions of the phase space which have the highest probability in the target distribution. Attempts to drive it away from these regions are rejected. Obviously, this is useful if one intends to compute ensemble averages, but limiting in some situations. This behavior is particularly problematic when dealing with first-order phase transitions, in two ways.

First, systems near or at phase coexistence are characterized by phase spaces with very rough free energy landscapes, with deep local minima and high barriers separating domains. Transitions between these domains would require visiting interphase states with very low Boltzmann weight, and, consequently, low probability. The result is that the sampling is unphysically limited to a non-representative region of the phase space, with a large bias towards the initial state of the chain. One can say that the system becomes stuck in a metastable phase, never reaching the equilibrium macroscopic phase expected of the thermodynamic state under investigation.

Second, while the problem of phase determination would be solved by computing and

comparing the free energy of the different phases, this function is not accessible in a standard simulation, because it depends on the *whole* volume of the phase space, and the limited region the algorithm is designed to sample is a poor estimator of that. Free energy *differences* relative to another state, on the other hand, can be computed by ensemble averages, with some limitations.

For these reasons, the study of phase coexistence problems requires specialized techniques. For the vapor-liquid transition, the Gibbs ensemble method has proved very popular since it was first proposed by Panagiotopoulos [17, 18] in the late 1980s. In this method, a simulation is prepared with a gas and a liquid phase in thermodynamic equilibrium but not in direct contact, which avoids dealing with an interface explicitly and the associated effects which are hard to quantify. The result is a simple, efficient and conceptually direct approach to the problem, which explains its appeal.

Determining the properties of solid-fluid[1] equilibria is a more challenging task. The Gibbs ensemble method, in its standard form, is not efficient enough when one of the phases is a crystalline solid or a dense fluid. Other direct methods have been proposed,such as the phase switch method of Wilding and Bruce [19] which uses multicanonical ensemble simulations to simultaneously sample from both fluid, solid and interphase states. These methods, in line with the Gibbs ensemble technique, take a commendably direct approach to the problem, but are non-trivial to implement when compared to standard MC methods, and are limited to study specific types of transitions.

The staple technique to study the solid-fluid transition, which is both more general, simple and based on sound thermodynamic principles, instead relies on free energy calculations. The basic idea is to perform simulations of both phases, in a range of temperatures, densities or other thermodynamic variables (even unphysical ones, such as a parameter that transforms the Hamiltonian of the system) and then perform thermodynamic integration to yield the free energy along these paths. The paths themselves may be direct, linking the two phases, or indirect, linking each phase to reference states of known free energy on each side of the transition, avoiding interphase states. Transforming from a fluid to a solid phase in a reversible way is difficult, due to the high hysteresis associated with this transition. The usual solution is to carry free energy calculations in the two phases *independently* and then determine the absolute value of the free energies from auxiliary techniques. This process is reviewed in detail in Chapter 3 of this thesis.

In that chapter, the solid-fluid transition of a more general form of the Lennard-Jones potential is investigated. The standard Lennard-Jones (LJ) potential [20], (in this context, known as $12-6$ LJ) is a simple interaction model that captures, with good approximation, the fundamental interactions between neutral atoms or molecules. It functions as a basic building

---

[1]In this manuscript, the term 'fluid' is used as a general denomination for a disordered, non-crystalline, phase, above or below the critical temperature, while 'liquid' refers only to the high density fluid at subcritical temperatures and 'vapor' or 'gas' to the low density, subcritical, one.

block for many force fields as well as a first physically important test case for new theories and methods. This potential includes an attractive term, proportional to r^{-6}, theoretically derived from the interactions of induced dipoles, and a strong repulsion term at short distances, to account for electron orbital overlap, described by the Pauli exclusion principle. This repulsive term was chosen to be proportional to r^{-12} mostly for reasons of computational efficiency, as it can be computed easily by repeated multiplication. An exponentially increasing repulsive term, as in the Buckingham potential, is a more realistic description of this effect which is why it can be found in many force fields, but comes with a cost of increased computational effort (which may be up to 4 times that of the standard $12 - 6$ LJ [21]). Some authors have used the alternative $n - 6$ Lennard-Jones, where the repulsive term is proportional to r^{-n} while the attraction term remains the same. For instance, some molecular force fields use the $9 - 6$ [22] and $8 - 6$ LJ [21] versions to describe non-bonded interactions because they are better approximations to Buckingham type potentials while being much more efficient. Very recently, a united-atom model of alkanes and perfluorocarbons was proposed that uses the $n - 6$ LJ to model interactions between pseudo-atoms, where n is a fitted parameter, and it was found that it matches or outperforms other force fields [23]. Softer potentials (which use a smaller value of n) are also useful to model polymer chains using a coarse-grained approach [24, 25]. Thus, there has been enough interest in the $n - 6$ Lennard-Jones potential to merit investigation into its properties and how they are affected by the change in the exponent n which regulates the steepness of the atomic core. The present work focuses on the phase behavior of this system, specifically, the solid-fluid transition is investigated for different values of n between 7 and 12. Only recently have the properties of this transition been investigated [26, 27], and this work provides independent results. This is the subject of Chapter 3.

The fullerene C_{60} exhibits a rich phase behavior, which has been investigated in some depth ever since this molecule was first discovered in 1985 by a team at Rice University [28]. At atmospheric pressure it is a crystal of monomer molecules, which are locked into specific orientations at low temperatures but, at around $260\,\mathrm{K}$, suffer a sudden transition into a phase with orientational disorder where they are rotating rapidly. For high pressures, polymerized phases begin to emerge, with the formation of 1D, 2D and even 3D polymers depending on the conditions. Additionally, there is an open question of whether a stable liquid phase is possible for this system.

In Chapter 4, the rotational phase transition of C_{60} fullerite is investigated by means of isothermal-isobaric MC simulations. This transition is easy to observe due to a sudden change in the lattice parameter [29]. This is readily visible in the isothermal-isobaric ensemble, where the pressure is fixed and the size of the simulation cell is allowed to fluctuate. In the standard algorithm, this change is isotropic, i.e., the same in all directions and at constant cell shape, usually cubic. In this work, an extension is considered [30] which allows arbitrary changes in both size and shape of the simulation cell. Details of this algorithm are given in Chapter 2. The C_{60} system is studied using atomistic models which consider each atom in each molecule

individually. Additionally, some of the models under investigation include bond charges to account for the inhomogeneous charge distribution on the molecule's surface.

Another area of research where computer simulation methods play a fundamental role is in the testing, development and optimization of materials as storage mediums for a variety of gases. The physical phenomena under investigation is physisorption unto the internal surface of porous materials, which requires relatively low energies and is easily reversible. It is often necessary to study this process at a microscopic scale, to understand how the structure of the material affects its adsorption affinity, which adsorbing sites are the most favorable, what is the preferred size and shape of guest molecules, the rate of diffusion inside the material, etc. This information is very hard to obtain experimentally. Monte Carlo and Molecular Dynamics methods, on the other hand, provide direct access to the microscopic details, and are suited to study relatively large systems. The Monte Carlo method, when using the grand-canonical algorithm (GCMC), is particularly efficient in the study of adsorption phenomena. It is designed to sample configurations where the number of particles fluctuates by performing random insertion and removal operations anywhere on the system. This way, one may focus on the equilibrium properties of a large guest+host system without having to account for an explicit interface between the inside and outside of the adsorbent, or wait for the molecules to disperse to the important regions of the material, which may be a slow process in complex topologies.

In Chapter 5, the adsorption of molecular hydrogen in the zeolite NaA is studied. Hydrogen is the ultimate eco-fuel, with the potential to serve as the perfect renewable energy carrier and solve the dangerous problems associated with the widespread use of fossil fuels today. The use of hydrogen in mobile applications, however, faces critical challenges. In particular, a cheap, safe and efficient solution to the hydrogen storage problem remains elusive. Storage by physisorption in microporous materials is a prominent candidate [31, 32, 33]. Zeolites [34, 35], in particular, are cheap, chemically and structurally stable, and widely available in a variety of configurations, which may be further fine-tuned to fit the application. In this work, the hydrogen adsorption uptake of the zeolite NaA is measured in equilibrium by the GCMC algorithm, for a wide range of pressures and temperatures. The potential model used considers the interaction between zeolite atoms and hydrogen molecules to be comprised of three terms: van der Waals, Coulomb and induced polarization.

This manuscript is organized as follows. In Chapter 2, the fundamentals of the MC algorithm in the various ensembles and the supporting principles of statistical physics are given. Some implementation details relevant to the work developed in this thesis are also explored. Following that, the three main topics under investigation are presented in separate chapters, in order: the determination of phase coexistence properties and application to the $n-6$ Lennard-Jones system; the rotational phase transition of solid C_{60}; and the adsorption of hydrogen in the zeolite NaA. Chapter 6 presents the concluding remarks and lays out

prospects of future research.

Chapter 2

Monte Carlo Methods in Statistical Mechanics

2.1   Introduction

A many-particle system of classical interacting particles, such as the ones that are the subject of this thesis, is completely described from the coordinates and momenta of each particle. A specific configuration of atomic positions and velocities defines a microscopic state of the system, and this, in turn, determines the properties of the system at a macroscopic scale. From an experimental point of view, atomic-scale pictures such as this are rarely attainable but even admitting that they were possible, understanding and predicting the behavior of the system at a macroscopic scale would still require solving a system of Hamilton's equations which, for even a very small amount of matter, is insurmountably complex. On the other hand, it is perfectly reasonable to study a real world system by observing its macroscopic properties directly, such as temperature, density or pressure, which are usually well behaved and predictable.

It is the domain of statistical mechanics to derive this macroscopic description from a probabilistic treatment of the underlying microscopic system.

Let a particular microscopic state be identified by a point P in the multidimensional phase space. The system, initially at this point at time t, P (t), will evolve according to the usual equations of motion, to different states P $(t + \Delta t)$, P $(t + 2\Delta t)$,... Let A (P) be the value that some physical observable quantity A takes when the system is in state P. When an experiment is performed to measure the macroscopic value of A, what is being measured, in effect, is the average of A over all points P that the system visited in the time scale of the observation,

$$\bar{A} = \lim_{T \to \infty} \frac{1}{T} \int_0^T A\left[P\left(t\right)\right] \mathrm{d}t, \tag{2.1}$$

where the observation time is, for all purposes, infinitely long. The Molecular Dynamics (MD)

technique approaches the problem from this perspective. In broad strokes, an MD program numerically solves the equations of motion of the system in discrete, but small, time steps, and accumulates a time average of the quantities of interest for a large enough number of steps.

A different approach is taken by conventional statistical mechanics, which introduces the concept of ensemble. First proposed by Gibbs [36], an ensemble consists of a very large, ideally infinite, number of copies of a system prepared in the same macroscopic state, but where each one may be in a different microstate P. These microstates are distributed according to a probability function $\rho_{\mathrm{ens}}(\mathrm{P})$ which is characteristic of the chosen thermodynamic state. These systems will evolve in time themselves, independently, but, once the equilibrium distribution has been reached, ρ_{ens} is independent of time.

Now, instead of averaging over the trajectory that a single system takes as it moves through phase space driven by its intrinsic dynamics, an average is taken over all the systems in the ensemble. Formally, an ensemble average of the observable A is defined as

$$\langle A \rangle = \int_{\mathrm{PS}} A\left(\mathrm{P}\right) \rho_{\mathrm{ens}}\left(\mathrm{P}\right) \mathrm{d}\mu, \qquad (2.2)$$

where PS means that the integral is taken over all points P in phase space and $\mathrm{d}\mu$ is the infinitesimal volume unit of that space. The form of ρ_{ens} is determined by a set of fixed macroscopic variables. The following sections provide further details on the most common ensembles. The Metropolis Monte Carlo (MC) technique attempts to sample states from an ensemble with the appropriate distribution and compute ensemble averages.

It remains to be shown that equations (2.1) and (2.2) are equivalent. This is known as the ergodic problem, and it is unsolved for most systems. If it was possible to demonstrate that a system may, eventually, reach all points of the phase space where $\rho_{\mathrm{ens}}\left(\mathrm{P}\right) > 0$ from any starting point, then, taking an average over the ensemble or following the system along its time evolution would be equivalent. Statistical mechanics is based on the ergodic hypothesis, the assumption that this is true for the system under study.

In the following subsections, the statistical ensembles relevant to this work will be introduced. The results pertain to a system of classical interacting particles in three dimensions. The details of the derivation of the probability densities and state functions are available on any introductory resource on statistical mechanics (e.g. [37]).

2.1.1   Canonical ensemble

The canonical, or constant-NVT ensemble, is the collection of states available to a closed system, with fixed walls, in thermal equilibrium with a heat bath. The system and bath may exchange energy but the bath is large enough that the temperature does not fluctuate. The

number of particles (N), the volume (V) and temperature (T) of the system under study are thus fixed, while the energy fluctuates. In these conditions, the probability that a system can be found in the neighborhood $d\mu$ of a given state P, with total energy $\mathcal{H}$ (P), is given by the well known Boltzmann distribution,

$$\rho_{NVT}\left(\text{P}\right)\text{d}\mu = \frac{\exp\left[-\beta\mathcal{H}\left(\text{P}\right)\right]\text{d}\mu}{Z_{NVT}}, \tag{2.3}$$

where Z_{NVT} is known as the partition function. For a classical system, Z is obtained by integrating the density function over all phase space,

$$Z_{NVT} = \int_{\text{PS}}\exp\left[-\beta\mathcal{H}\left(\text{P}\right)\right]\text{d}\mu. \tag{2.4}$$

Z_{NVT} is a function of the inverse temperature $\beta = 1/k_B T$, as well as volume and number of particles. $\mathcal{H}$ is the Hamiltonian of the system and can be split into two independent terms, separate functions of either the spatial coordinates or momenta of the particles.

Let $\mathbf{r}^N = \{\mathbf{r}_1, \mathbf{r}_2, ..., \mathbf{r}_N\}$, where $\mathbf{r}_i = (x_i, y_i, z_i)$, be a set of coordinates of the N particles of the system, and $\mathbf{p}^N = \{\mathbf{p}_1, \mathbf{p}_2, ..., \mathbf{p}_N\}$, with $\mathbf{p}_i = (p_{x,i}, p_{y,i}, p_{z,i})$, the corresponding momentum vectors. $\mathbf{r}^N$ and $\mathbf{p}^N$ define, at a given moment, a microscopic configuration of the system. The total energy of that configuration is

$$\mathcal{H}\left(\mathbf{r}^N, \mathbf{p}^N\right) = K\left(\mathbf{p}^N\right) + U(\mathbf{r}^N), \tag{2.5}$$

where K is the kinetic energy and a function of $\mathbf{p}^N$ only, and U is the potential energy, function of $\mathbf{r}^N$ only. Equation (2.4) thus becomes

$$\begin{aligned} Z_{NVT} &= \frac{1}{N!}\frac{1}{h^{3N}}\int_{-\infty}^{+\infty}\text{d}\mathbf{p}^N\exp\left[-\beta K\left(\mathbf{p}^N\right)\right]\int_V\text{d}\mathbf{r}^N\exp\left[-\beta U\left(\mathbf{r}^N\right)\right]\\ &= Z_{NVT}^k Z_{NVT}^c, \end{aligned} \tag{2.6}$$

where the superscript k (c) indicates the kinetic (configurational) part of the partition function. The term $1/N!$ is introduced to account for the indistinguishability of the particles, and h is the Planck's constant. The inclusion of h reflects a quantization of phase space imposed by the principle of uncertainty: the uncertainty in the simultaneous measurement of momenta and coordinates is given by $\Delta x \Delta p \geq h$, which means that two states measured inside these limits are, from a quantum mechanical perspective, indistinguishable. Thus, the integration over a volume in phase space should be normalized by the smallest quanta of this space: h^{3N}.

The kinetic energy term is $K = \sum_i \mathbf{p}_i^2/2m$, where m represents the mass of a particle, and so the integration over the momenta can be solved analytically. The kinetic part of the partition function is

$$Z_{NVT}^k = \frac{1}{N!\Lambda^{3N}}, \tag{2.7}$$

where Λ is the thermal de Broglie wavelength,

$$\Lambda = \left(\frac{h^2}{2\pi m k_B T}\right)^{1/2}.$$ (2.8)

The configurational part of the partition function follows,

$$Z^c_{NVT} = \int_V \mathrm{d}\mathbf{r}^N \exp\left[-\beta U\left(\mathbf{r}^N\right)\right].$$ (2.9)

Due to the extension of the configuration space ($3N$ variables extending the whole volume of the system), it is usually impossible to compute this term, either analytically or numerically, for any relatively large system. Notwithstanding, there are situations where some form of simplification is justifiable which allows for this calculation. For example, a system at very low densities may be approximated by a gas of non-interacting particles, the ideal gas. Since $U = 0$, the partition function of the ideal gas is simply

$$Z^{\mathrm{id}}_{NVT} = V^N Z^k_{NVT}.$$ (2.10)

Because the integral over the momenta is known, the distribution probability as a function of $\mathbf{p}^N$ can be computed exactly, and the ensemble averages of functions $A\left(\mathbf{p}^N\right)$ that depend only on the moment are usually easy to solve. The problem of calculating the ensemble average of equation (2.2) facing any Monte Carlo algorithm is thus reduced to probing just the space of the $3N$ spatial coordinates. The probability distribution to consider is simply a function of the potential energy of the configuration,

$$\rho_{NVT}\left(\mathbf{r}^N\right)\mathrm{d}\mathbf{r}^N = \frac{\exp\left[-\beta U\left(\mathbf{r}^N\right)\right]\mathrm{d}\mathbf{r}^N}{Z^c_{NVT}}.$$ (2.11)

The Helmholtz free energy F is related to the canonical partition function by

$$\beta F = -\ln Z_{NVT}.$$ (2.12)

The free energy of the ideal gas follows from equation (2.10) and the Stirling approximation $\ln N! \approx N \ln N - N$ where higher order terms are ignored,

$$\beta F^{\mathrm{id}} = N\left(\ln \rho \Lambda^3 - 1\right).$$ (2.13)

2.1.2 Isothermal-isobaric ensemble

A system with moving walls in contact with a thermal reservoir at constant pressure (P), constant number of particles and constant temperature is part of the isothermal-isobaric, or constant-NPT, ensemble. The partition function of this ensemble is obtained by integrating the canonical partition function, Z_{NVT}, over all volumes,

$$Z_{NPT} = \frac{1}{V_0} \int Z_{NVT} \exp\left(-\beta PV\right) dV, \tag{2.14}$$

where V_0 is a normalizing constant that makes Z_{NPT} dimensionless. Frenkel and Smit [38] choose $V_0 = (\beta P)^{-1}$ but other choices are possible and differences vanish in the thermodynamic limit.

The probability of finding a configuration $\mathbf{r}^N$ with a volume V in this ensemble is

$$\rho_{NPT}\left(\mathbf{r}^N, V\right) d\mathbf{r}^N dV = \frac{\exp\left(-\beta PV\right)\exp\left[-\beta U\left(\mathbf{r}^N\right)\right] d\mathbf{r}^N dV}{\int dV' \exp\left(-\beta PV'\right) \int_{V'} d\mathbf{r}'^N \exp\left[-\beta U\left(\mathbf{r}'^N\right)\right]}. \tag{2.15}$$

The thermodynamic function characteristic of the isothermal-isobaric ensemble is the Gibbs free energy G, which is related to the partition function by

$$\beta G = -\ln Z_{NPT}. \tag{2.16}$$

2.1.3 Grand-canonical ensemble

The grand-canonical, or constant-μVT, ensemble is the collection of all possible states of a system with a fixed volume which is allowed to exchange, not only energy, but also particles with a reservoir. This exchange happens at constant temperature and chemical potential (μ), which are set by the larger system, the reservoir. The grand-canonical partition function of a one component system is obtained by a weighted sum of the canonical partition function over all values of N,

$$Z_{\mu VT} = \sum_{N=0}^{\infty} e^{\beta \mu N} Z_{NVT}. \tag{2.17}$$

The probability of a microscopic state of N particles with positions $\mathbf{r}^N$ on the ensemble is

$$\rho_{\mu VT}\left(\mathbf{r}^N, N\right) d\mathbf{r}^N = \frac{\frac{1}{N!\Lambda^{3N}} \exp\left[\beta\mu N\right]\exp\left[-\beta U\left(\mathbf{r}^N\right)\right] d\mathbf{r}^N}{\sum_{N'=0}^{\infty} \frac{1}{N'!\Lambda^{3N'}} \exp\left[\beta\mu N'\right] \int_{V'} d\mathbf{r}'^{N'} \exp\left[-\beta U\left(\mathbf{r}'^{N'}\right)\right]}, \tag{2.18}$$

where, unlike before, the terms $N!$ and Λ^{3N} must be explicitly included in the definition of the probability density function due to the dependence with the number of particles.

The characteristic state function of this ensemble is the grand potential, Ω, which is given by

$$\Omega = -PV = -\frac{1}{\beta} \ln Z_{\mu VT}. \tag{2.19}$$

2.2 Metropolis Monte Carlo

2.2.1 Importance sampling

Central to the idea of the Metropolis Monte Carlo [1] algorithm is the concept of importance sampling. In order to solve an ensemble average, equation (2.2), one can either generate samples P with uniform probability and weigh them with $\rho_{\text{ens}}(\text{P})$ or generate samples P with probability $\rho_{\text{ens}}(\text{P})$ and weigh them evenly. The former idea is, for any but the simplest systems, impossible. Considering the very modest case of a system with 10 particles in a 3D volume and a scheme involving sampling positions on a discrete mesh of 10 points for each dimension, that would require evaluating 10^{30} configurations. An hypothetical very fast super computer capable of evaluating one configuration every picosecond would still take about roughly twice the age of the Universe to compute this average. In most applications in statistical physics, the phase space is more likely to extend over thousands of dimensions. To make matters worse, ρ_{ens} is very sharply peaked, and only a very limited region of that space actually has a non-negligible weight. It is unlikely that any of the configurations that contribute to the integral would even be included in a uniform sampling set, randomly chosen or otherwise. Finally, computing the weight $\rho_{\text{ens}}(\text{P})$ requires *a priori* knowledge of the normalizing factor, the partition function Z, which is a function of the whole volume of the phase space, and thus, an even harder problem.

The second approach is to devise a scheme able to generate the samples with probability ρ_{ens}. This way, the more important a configuration is (in the sense that its ensemble weight is larger) the more likely it is to appear on the sampled set. This procedure is known as importance sampling.

Let $\langle A \rangle_M$ be an estimator of the ensemble average $\langle A \rangle_{\text{ens}}$ taken by evaluating $A(\text{P})$ for M points P in phase space. If those states are chosen with a specific probability distribution $p(\text{P})$, then

$$\langle A \rangle_{\text{ens}} \simeq \langle A \rangle_M = \frac{\sum_{i=1}^{M} \left[p(\text{P}_i) \right]^{-1} A(\text{P}_i) \rho_{\text{ens}}(\text{P}_i)}{\sum_{i=1}^{M} \left[p(\text{P}_i) \right]^{-1} \rho_{\text{ens}}(\text{P}_i)}, \qquad (2.20)$$

where P_i is the i-th generated sample from the set with M total. If the sampling distribution is $p = \rho_{\text{ens}}$, then equation (2.20) becomes

$$\langle A \rangle_{\text{ens}} \simeq \langle A \rangle_M = \frac{1}{M} \sum_{i=1}^{M} A(\text{P}_i), \qquad (2.21)$$

and the ensemble average is obtained by a simple arithmetic mean of the sampled values. An important point of this formulation is that it is sufficient to choose p *proportional* to ρ_{ens}, since the normalizing factor is canceled out. This means that it is not necessary to know

the value of the partition function to obtain ensemble averages. The downside is that it is also impossible to know it. The partition function, and related quantities that depend on the whole volume of phase space, cannot be expressed as a simple ensemble average (in way that can be computed with any degree of efficiency). Special techniques have been designed to work around this limitation in various ways, and this will be discussed further in Chapter 3.

Additionally, it is also sometimes useful to use a sampling distribution p that merely *approximates* ρ_{ens}, the real distribution, which can be done, within some constraints of efficiency, as long as the proper corrections that result from equation (2.20) are included. This can be used to enhance the sampling (by forcing a scheme which samples from interesting regions of phase space) or even compute the ratio between partition functions of different systems.

The remaining problem is that of generating a sequence of M states distributed according to the chosen probability function p, which is solved by a class of Monte Carlo algorithms known as Markov Chain Monte Carlo.

2.2.2 Markov chains

A Markov chain is a sequence of states of a system generated by what is know as a Markov process, a stochastic mechanism that, given an initial state v, randomly generates a new state w with a certain transition probability $\Gamma(v \rightarrow w)$ which is independent of the history of the process up to that point [39]. The Markov process has the property of being memoryless. Γ defines a stochastic matrix, the Markov matrix, describing the transition probabilities between any two states. Here, the discussion is limited to time-homogenous Markov matrices.

Since the Markov process is random, a different state w may be generated every time the chain is given the same input state v, but the normalization condition is necessary to guarantee that some state is always generated from v,

$$\sum_w \Gamma(v \rightarrow w) = 1. \tag{2.22}$$

There is also a possibility that the system remains in the same state after a Markov step, i.e.,

$$\Gamma(v \rightarrow v) = 1 - \sum_{w \neq v} \Gamma(v \rightarrow w). \tag{2.23}$$

In a Monte Carlo simulation, a Markov chain of states, $\{v, w, \alpha, ...\}$, is constructed sequentially, such that, for sufficiently long times, the distribution of states will reach a limiting stationary distribution, which is the target distribution of the algorithm. In these conditions the system is said to have reached equilibrium. To guarantee this outcome, constraints are imposed on the choice of transition probabilities: balance and ergodicity.

To see this, first, the "time" evolution of the Markov process is stated as [37]

$$p(v, t+1) = \sum_w \Gamma(w \to v) \, p(w, t) \,, \tag{2.24}$$

where $p(v, t)$ is the probability of finding the system in state v at "time" t (here, the variable t is meant to describe the evolution along the chain in discrete steps, and not an actual physical time). Equation (2.24) is simply a realization of the stated property of Markov processes that the next state in a chain depends only on the current state, i.e., it holds no memory of its history. This can be expressed in matrix form. Let Π be the transition matrix with elements $\Pi_{vw} = \Gamma(w \to v)$ and $\mathbf{p}(t)$ the column vector with elements $p(v, t)$, then equation (2.24) becomes

$$\mathbf{p}(t) = \Pi \mathbf{p}(t-1) \,, \tag{2.25}$$

which can be iterated back to the initial distribution,

$$\mathbf{p}(t) = \Pi^t \mathbf{p}(0) \,, \tag{2.26}$$

where Π^t is the product of t matrices Π. For sufficiently long times, the Markov process reaches a simple stationary distribution,

$$\mathbf{p} = \lim_{t \to \infty} \Pi^t \mathbf{p}(0) \,. \tag{2.27}$$

For a generic choice of Π is it not guaranteed that this limit exists, but for now it is assumed so. Since this distribution is stationary it obeys the steady-state condition [37]

$$\mathbf{p} = \Pi \mathbf{p} \tag{2.28}$$

or

$$p(v) = \sum_w \Gamma(w \to v) \, p(w) \,, \tag{2.29}$$

where the omission of t reflects the fact that this distribution is now stationary.

By applying the normalization condition equation (2.22) to the left side of equation (2.29), the following relation is obtained,

$$\sum_w \Gamma(v \to w) \, p(v) = \sum_w \Gamma(w \to v) \, p(w) \,. \tag{2.30}$$

This a balance condition which shows that, for a system in equilibrium, the rate of transitions going into a state is the same as the rate of transitions going out of it. A stronger condition is conventionally used in Monte Carlo methods,

$$\Gamma(v \to w) \, p(v) = \Gamma(w \to v) \, p(w) \,, \tag{2.31}$$

which is called detailed balance or microscopic reversibility. This condition not only imposes that the rates of transitions in and out of a state are equal, since it obeys equation (2.30), but also that the transition rates between any two states is the same in both directions. Imposing detailed balance on the transition probability matrix is sufficient to guarantee that p is a stationary distribution of the chain, but not strictly necessary [40].

An additional constraint must be imposed to guarantee that equation (2.27) holds, that a limiting distribution can be reached and that it is unique. Equation (2.28) shows that this distribution is the eigenvector of Π with eigenvalue 1. If the Markov chain observes the property of ergodicity, defined as

$$\forall v, w \ \exists t \in \mathbb{N} \ : \ \left(\Pi^t\right)_{wv} > 0, \tag{2.32}$$

or, in other words, that any state w can be reached from any state v in a finite number of steps, then it can be shown there is only one eigenvector with corresponding eigenvalue 1 and thus, only a single limiting distribution, and that the chain necessarily approaches this distribution for sufficiently long times, independently of the initial state [39, 41].

Therefore, if the Markov process is ergodic (which is not trivial to prove for a generic algorithm) and the transition probabilities obey equation (2.31), with p given by the probability distribution of the ensemble, then it is guaranteed that, for any initial state and after a finite number of steps, the process will sample states with the correct distribution.

2.2.3 Simulations in the canonical ensemble

The original algorithm of Metropolis *et al.* [1] was the first solution to the problem of generating a Markov chain with the desired distribution of states. It can be seen as a random walk in the region of phase space where the probability of the sampled states is highest. At any point in the process, a move to a different point in this space is proposed which can either be accepted or rejected, depending on the ratio between the probabilities of the final and initial state. If the probability of the new state is too low, the move is rejected, keeping the system within the important regions of phase space.

In practice, this is achieved by splitting the transition probability from state v to state w into two independent terms,

$$\Gamma\left(v \rightarrow w\right) = sel\left(v \rightarrow w\right) acc\left(v \rightarrow w\right), \tag{2.33}$$

where *sel* and *acc* are, respectively, the selection and acceptance probabilities. *sel* defines the likelihood that a move is proposed that may transform v into w. In the original Metropolis scheme, this probability is uniform over a set of neighboring states w of v, and symmetric, i.e., $sel\left(v \rightarrow w\right) = sel\left(w \rightarrow v\right)$. *acc* is the probability of accepting the trial move from v to w, and was chosen by Metropolis *et al.* to be

$$acc\left(v \rightarrow w\right) = \begin{cases} \frac{\rho(w)\mathrm{d}\mu}{\rho(v)\mathrm{d}\mu} & \text{if } \rho\left(w\right) < \rho\left(v\right) \\ 1 & \text{if } \rho\left(w\right) \geq \rho\left(v\right) \end{cases}, \tag{2.34}$$

where ρ is the ensemble distribution density and $\mathrm{d}\mu$ the infinitesimal unit volume of phase space that converts it to a probability, as defined in the previous sections.

The move from v to w is accepted or rejected by comparing *acc* to a random number generated from a uniform distribution in the interval $[0, 1]$. If the random number is less than $acc\left(v \rightarrow w\right)$, then it is accepted and the state w is added to the chain; otherwise, it is rejected and v must be counted again.

It is straightforward to show that the Markov transition matrix defined by a symmetric selection probability and the acceptance criteria of equation (2.34) obeys the condition of detailed balance, equation (2.31).

The original application of the Metropolis algorithm was a system of two dimensional hard disks in the canonical ensemble, but it is easy to extended to three dimensions, an arbitrary potential model and other ensembles. Here, the general case of a system of N particles confined to a three dimensional volume V, with a potential energy given by function U, is considered.

In a step of the algorithm, one particle i, at position $\mathbf{r}_i$, is chosen with equal probability from the total N, and then displaced randomly to a point chosen with uniform probability inside a cube of side $2\delta r$, centered in the original position of i,

$$\mathbf{r}'_i = \mathbf{r}_i + \left[(2\mathcal{R}_1 - 1)\hat{\mathbf{x}} + (2\mathcal{R}_2 - 1)\hat{\mathbf{y}} + (2\mathcal{R}_3 - 1)\hat{\mathbf{z}}\right]\delta r, \tag{2.35}$$

where $\mathbf{r}'_i$ is the new position of the particle after the operation and $\mathcal{R}_i$, $i = 1, 2, 3$, are three independent uniform random numbers between 0 and 1. A new configuration $\mathbf{r}'^N$, where only the position $\mathbf{r}_i$ was changed, is generated. This procedure constructs the symmetric trial move matrix $sel\left(\mathbf{r}^N \rightarrow \mathbf{r}'^N\right)$.

Plugging in the configurational distribution function for the canonical ensemble, given by equation (2.11), into equation (2.34), results in the acceptance probability for the move from $\mathbf{r}^N$ to $\mathbf{r}'^N$,

$$acc\left(\mathbf{r}^N \rightarrow \mathbf{r}'^N\right) = \min\left[1, \exp\left(-\beta\Delta U\right)\right], \tag{2.36}$$

where $\Delta U = U\left(\mathbf{r}'^N\right) - U\left(\mathbf{r}^N\right)$ is the difference between the energy of the two states. This means that a move that results in a decrease in energy (leading to a larger value of $\exp\left(-\beta U\right)$ and consequently more weight on the ensemble average) is always accepted, while the probability of accepting an increase in energy (and decrease in weight) drops exponentially with the magnitude of that increase.

The algorithm is straightforward, but some care must be taken in the choice of some free

parameters. For example, the maximum distance that a particle can move in a trial operation, δr defined above, can have a significant effect on the efficiency of the method. Too large a value and the resulting configuration will be significantly different from the initial one, likely with a much higher energy, which will lead to a high rate of rejections. If the value is too low, the trial moves are frequently accepted but the resulting states are very similar and the chain will be highly correlated. Both cases lead to a very inefficient sampling of the phase space. For this reason, this parameter is often set to yield a 50% acceptance ratio, although that is not necessarily the best choice [38]. This adjustment can be performed iteratively at the beginning of the simulation.

Another important point is that the system requires a non-negligible number of steps before it reaches the equilibrium distribution. These states must be discarded from the final set of samples. Additionally, some care must be taken when preparing the initial state. In principle, as mentioned above, the Markov process is guaranteed to reach an equilibrium distribution if it obeys the balance and ergodic conditions. However, problems may arise if the system suffers from long relaxation times and slow evolution, in which case the equilibrium distribution may never be reached within finite simulation time, if the initial state is chosen arbitrarily. This problem is particularly evident near first-order phase transitions, and will be addressed in more detail in Chapter 3.

2.2.4 Simulations in the isothermal-isobaric ensemble

The isothermal-isobaric ensemble (constant-NPT) is a popular ensemble in which to carry simulations since it emulates the normal conditions of an experiment in a laboratory, where observations are usually made on a fixed amount of matter at a constant pressure and temperature. In this ensemble, the volume of the box is allowed to fluctuate under the influence of an applied pressure P. This algorithm was first presented by Wood [2] in the context of hard-disks and later applied to a Lennard-Jones fluid by McDonald [42]. In this section, the most common isothermal-isobaric algorithm will be presented which is limited to isotropic pressures and isotropic volume updates. In the following section, a more general algorithm will be presented.

In order to sample from the $\left(\mathbf{r}^N, V\right)$ multidimensional phase space, an MC trial operation is defined that changes the volume of the simulation box from V to V'. The simulation cell, assumed cubic, is expanded to this new volume isotropically and the particle positions are scaled to accommodate the new volume,

$$\mathbf{r}'^N = \left(\frac{V'}{V}\right)^{1/3} \mathbf{r}^N.$$
(2.37)

The ratio between the probabilities of the starting and final states follows from equation (2.15),

$$\frac{\rho_{NPT}\left(\mathbf{r}'^N, V'\right) d\mathbf{r}'^N dV'}{\rho_{NPT}\left(\mathbf{r}^N, V\right) d\mathbf{r}^N dV} = \frac{\exp\left(-\beta PV'\right)}{\exp\left(-\beta PV\right)}\left(\frac{V'}{V}\right)^N \exp\left(-\beta \Delta U\right), \qquad (2.38)$$

where ΔU is again the difference between the energies of the two states, $d\mathbf{r}'^N/d\mathbf{r}^N = (V'/V)^N$ and dV'/dV was assumed to be 1.

It is common practice to generate a new trial volume by a random walk in the space of $\ln V$ instead of V. The appropriate volume update rule is given by

$$\ln V' = \ln V + (2\mathcal{R} - 1)\delta\left(\ln V\right), \qquad (2.39)$$

where $\mathcal{R}$ is a uniform random number in the interval $[0, 1]$ and $\delta\left(\ln V\right)$ is the maximum displacement of $\ln V$ in one step. This parameter plays a similar role to δr of equation (2.35) and is adjusted in the same manner to reach an adequate balance between the number of accepted and rejected trials. It is trivial to show that changing the integration variable from V to $\ln V$ introduces an additional V'/V term in equation (2.38), but the effect is irrelevant in the thermodynamic limit ($N \gg 1$).

The selection matrix *sel* is, again, symmetric. The acceptance probability for the volume update move is

$$acc\left(\mathbf{r}^N, V \to \mathbf{r}'^N, V'\right) = \min\left[1, \exp\left\{-\beta\left[\Delta U + P\left(V' - V\right)\right] + (N+1)\ln\frac{V'}{V}\right\}\right]. \qquad (2.40)$$

where the case of the random walk in $\ln V$ space was considered.

In addition to this operation, the usual particle displacement moves are performed at fixed volume. Usually, a volume update is performed, on average, every N displacements.

Recalculating the energy in the new volume V' is an expensive operation (it scales, approximately, with N^2), which limits the efficiency of the sampling in the space of volumes. Fortunately, for those potentials that can be written as a linear combination of sums of powers of the interparticle distances, the new energy terms can be obtained by simply scaling the old ones by $(V'/V)^{n/3}$, where n is the power of one term. An important class of such potentials are those in Lennard-Jones family. The $n - 6$ Lennard-Jones will be discussed in Chapter 3. Ferreira and Barroso [43] also demonstrated how to approximate a potential with an arbitrary dependence on distance by a sum of powers, thus generalizing the applicability of this energy scaling.

2.2.5   Simulations in the isothermal-isobaric ensemble with anisotropic volume updates

There are some circumstances where the isotropic volume update scheme presented in §2.2.4 is insufficient and it is necessary to account for fluctuations in both volume and shape of the simulation box. In these situations, it is more appropriate to define the simulation cell

as a parallelepiped whose lengths in different directions and internal angles may vary. This is essential when dealing with systems under shear or uniaxial stress, or solids that may undergo a structural phase transition.

A method which allows general deformations of the simulation cell was derived by Parrinello and Rahman [44, 45] for Molecular Dynamics simulations. It complements the extended Lagrangian of Andersen [46] with the introduction of 9 additional dynamical variables, the Cartesian components of the 3 basis vectors of the cell. Let $\mathbf{a}_i$, $i = 1, 2, 3$, be the three vectors that define the periodicity of the cell, and let $\mathbf{e}_a$, $a = 1, 2, 3$ be the three orthogonal Cartesian unit vectors. The basis matrix h is a 3-by-3 matrix with elements

$$h_{ai} = \mathbf{e}_a \cdot \mathbf{a}_i. \tag{2.41}$$

For the case of a cubic simulation cell, h is a diagonal matrix, $h_{ij} = V^{1/3}\delta_{ij}$. The volume of the cell is given by

$$V = |\det h|. \tag{2.42}$$

In the variable shape scheme, it is more convenient to represent the position of a particle by its scaled, or lattice, coordinates, $\mathbf{s}$. The transformation from one coordinate system to the other is achieved by the matrix operation

$$\mathbf{r} = h\mathbf{s}, \tag{2.43}$$

where $\mathbf{r}$ is the position of the particle in world coordinates and both $\mathbf{r}$ and $\mathbf{s}$ are column vectors.

Souza and Martins [47] later proposed a modification to the method of Parrinello and Rahman that considers only 6 dynamical variables associated with the cell, instead of 9, which are the elements of the symmetrical tensor g defined by

$$g_{ij} = \mathbf{a}_i \cdot \mathbf{a}_j = g_{ji}. \tag{2.44}$$

This approach effectively removes the dependence of the dynamics on the absolute orientation of the cell, which is irrelevant to the thermodynamics of the system, solving many problems associated with the original method. It is still convenient to work with the basis matrix h directly, instead of the metric tensor, as it provides a simple relationship between scaled and world coordinates, as given by equation (2.43). For this, one simply needs to construct a symmetric matrix h compatible with g [38, 47]. The anti-symmetric part of h is related to the orientation of the basis in space which is unimportant for most purposes.

The framework developed by Souza and Martins in the context of Molecular Dynamics has been applied to a Monte Carlo setting by Lee [30]. Here, the case of an external isotropic pressure P will be considered, but the author also presents similar expressions for an external

anisotropic stress. In that work, the extended Hamiltonian of the Souza-Martins formalism is used to construct a probability density for an ensemble with $6N + 12$ dimensions (which are the $3N$ particle coordinates, $3N$ particle momenta, 6 components of the metric tensor and the 6 components of the momentum tensor canonically conjugate to g). All the momentum degrees of freedom can be integrated out resulting in the partition function for the extended ensemble given by [30]

$$Z_{NPT}^{\text{aniso}} = \frac{1}{N! \Lambda^{3N} V_g^6} \int \mathrm{d}\mathbf{s}^N \int \mathrm{d}h \gamma \left(h \right) \exp \left(-\beta \left\{ U \left(\mathbf{s}^N, h \right) + P \left(\det h \right) \right\} \right), \qquad (2.45)$$

where, for convenience, the basis matrix h was used instead of the metric tensor g. The integration is restricted to the symmetric elements of h and the infinitesimal unit of measure is

$$\mathrm{d}h = \mathrm{d}h_{11} \mathrm{d}h_{22} \mathrm{d}h_{33} \mathrm{d}h_{23} \mathrm{d}h_{13} \mathrm{d}h_{12}. \qquad (2.46)$$

V_g is a constant related to the (fictitious) dynamics of the cell and has a similar role to the constant V_0 defined in equation (2.14), having no contribution to any thermodynamic quantity. γ is given by

$$\gamma \left(h \right) = J \left(\frac{g_{ij}}{h_{ak}} \right) \frac{\left(\det h \right)^N}{\det_{4s} \left(H_{ab,ij} \right)}, \qquad (2.47)$$

where $H_{ab,ij}$ is a four-rank tensor defined as

$$H_{ab,ij} = \frac{h_{ai} h_{bj}}{\det h}. \qquad (2.48)$$

$H_{ab,ij}$ can be viewed as a 2D matrix with indices ab and ij. There are only 6 independent pairs of indices ab or ij, making this a 6×6 matrix. The determinant $\det_{4s} \left(H_{ab,ij} \right)$, where the $4s$ notation means the determinant is taken over pairs of indices, is

$$\det_{4s} \left(H_{ab,ij} \right) = \frac{\det_{4s} \left(h_{ai} h_{bj} \right)}{\left(\det h \right)^6}$$

$$= \begin{vmatrix} h_1 & h_6 & h_5 \\ h_6 & h_2 & h_4 \\ h_5 & h_4 & h_3 \end{vmatrix}^{-6} \times \begin{vmatrix} h_1^2 & h_6^2 & h_5^2 & h_6 h_5 & h_1 h_5 & h_1 h_6 \\ h_6^2 & h_2^2 & h_4^2 & h_2 h_4 & h_6 h_4 & h_6 h_2 \\ h_5^2 & h_4^2 & h_3^2 & h_4 h_3 & h_5 h_3 & h_5 h_4 \\ h_6 h_5 & h_2 h_4 & h_4 h_3 & h_2 h_3 & h_6 h_3 & h_6 h_4 \\ h_1 h_5 & h_6 h_4 & h_5 h_3 & h_6 h_3 & h_1 h_3 & h_1 h_4 \\ h_1 h_6 & h_6 h_2 & h_5 h_4 & h_6 h_4 & h_1 h_4 & h_1 h_2 \end{vmatrix}, (2.49)$$

where the Voigt index notation ($1 = 11$, $2 = 22$, $3 = 33$, $4 = 23 = 32$, $5 = 13 = 31$,

$6 = 12 = 21$) was used. The Jacobian J is included due to the transformation of the integration variable from g to h,

$$J\left(\frac{g_{ij}}{h_{ak}}\right) = \det_{4s}\left(\frac{\partial g_{ij}}{\partial h_{ak}}\right) = \begin{vmatrix} 2h_1 & 0 & 0 & 0 & 2h_5 & 2h_6 \\ 0 & 2h_2 & 0 & 2h_4 & 0 & 2h_6 \\ 0 & 0 & 2h_3 & 2h_4 & 2h_5 & \\ 0 & h_4 & h_4 & h_2+h_3 & h_6 & h_5 \\ h_5 & 0 & h_5 & h_6 & h_1+h_3 & h_4 \\ h_6 & h_6 & 0 & h_5 & h_4 & h_1+h_2 \end{vmatrix}. \tag{2.50}$$

The Monte Carlo sampling of the variable cell shapes is implemented by an MC trial move that attempts to change the elements of the symmetric matrix h by a small amount, at regular intervals. This update rule is similar to the ones defined in previous sections,

$$h'_{ab} = h_{ab} + (2\mathcal{R} - 1)\,\delta h_{ab}, \tag{2.51}$$

where δh is a 3×3 symmetric matrix whose elements are the maximum possible changes in h, in one step. $\mathcal{R}$ is a uniform random number between 0 and 1. This operation is performed simultaneously for the 6 independent indices, and should not break the symmetry of h.

The acceptance probability for the trial update is

$$acc\,(h \to h') = \min\left[1, \exp\left\{-\beta\left[\Delta U + P\left(\det h' - \det h\right)\right] + \ln\frac{\gamma\,(h')}{\gamma\,(h)}\right\}\right], \tag{2.52}$$

where ΔU is again the difference between the energies of the final and initial states,

$$\Delta U = U\left(\mathbf{s}^N, h'\right) - U\left(\mathbf{s}^N, h\right). \tag{2.53}$$

The standard MC operation of particle displacement remains the same since it is performed at constant cell shape (constant h). It can be shown that this acceptance probability reduces to equation (2.40) for the case of isotropic volume updates, which corresponds to the case where h is a diagonal matrix with only one independent variable [30].

2.2.6 Simulations in the grand-canonical ensemble

The grand-canonical ensemble is the natural choice when the properties that are being studied are directly related to the number of particles that constitute a system. In this ensemble, the system exchanges energy and particles with a gas reservoir which has a fixed temperature and chemical potential. Additionally, the volume is also fixed. The most prominent example of an application for this ensemble is the study of adsorption phenomena, where the quantity of interest is the amount of atoms or molecules that are adsorbed into a given host system, as a function of temperature and chemical potential of the reservoir gas, which

is related to applied pressure by an equation of state.

An algorithm designed to sample from this ensemble must include operations which change the number of particles. Norman and Filinov, in 1969 [3], first implemented this idea by proposing two new operations: trial additions and removals of one particle.

In an insertion operation, $\left(\mathbf{r}^N, N\right) \to \left(\mathbf{r}^{N+1}, N+1\right)$, a new particle is added at a random position in the system volume, uniformly chosen in the simplest of cases. Biased insertion operations may be necessary for more compact or molecular systems [48]. In a removal operation, $\left(\mathbf{r}^N, N\right) \to \left(\mathbf{r}^{N-1}, N-1\right)$, a particle is selected from the total of N with uniform probability, and removed. If the probability of attempting both of these trial operations is the same, then the selection matrix *sel* is symmetric [41].

For the addition of a particle, applying equation (2.18) gives the ratio between the probabilities of the final and starting states,

$$\frac{\rho_{\mu VT}\left(\mathbf{r}^{N+1}, N+1\right)\mathrm{d}\mathbf{r}^{N+1}}{\rho_{\mu VT}\left(\mathbf{r}^N, N\right)\mathrm{d}\mathbf{r}^N} = \frac{V\exp\left(\beta\mu\right)}{\Lambda^3\left(N+1\right)}\exp\left(-\beta\Delta U\right), \tag{2.54}$$

where the term V follows from $\mathrm{d}\mathbf{r}^{N+1}/\mathrm{d}\mathbf{r}^N = V^{N+1}/V^N = V$ and is due to the fact that the integration of the $N+1$ system is carried over an additional 3 spatial dimensions . The term $\Delta U = U\left(\mathbf{r}^{N+1}\right) - U\left(\mathbf{r}^N\right)$ is the energy difference between the states, which, for a pairwise additive potential, is just the energy of particle $i = N+1$ with respect to the remaining N.

The acceptance probability of the insertion trial operation is, then,

$$acc\left(\mathbf{r}^N, N \to \mathbf{r}^{N+1}, N+1\right) = \min\left[1, \frac{V\exp(\beta\mu)}{\Lambda^3(N+1)}\exp\left(-\beta\left\{U\left(\mathbf{r}^{N+1}\right) - U\left(\mathbf{r}^N\right)\right\}\right)\right]. \tag{2.55}$$

For the removal operation, a similar derivation yields

$$acc\left(\mathbf{r}^N, N \to \mathbf{r}^{N-1}, N-1\right) = \min\left[1, \frac{\Lambda^3 N}{V\exp(\beta\mu)}\exp\left(-\beta\left\{U\left(\mathbf{r}^{N-1}\right) - U\left(\mathbf{r}^N\right)\right\}\right)\right]. \tag{2.56}$$

Other choices for the acceptance probabilities are possible [41]. In this algorithm, the particle displacement move is not strictly necessary, as it is equivalent to a removal of a particle at the old site followed by an insertion at the new site. For this reason, it is usually disregarded [49]. When it is included, the probability of attempting it, as opposed to attempting an insertion or removal, is a free parameter. Usually, performing all the three trial operations the same average number of times for each MC step (in random order to ensure detailed balance is respected) gives the best results [41].

The GCMC algorithm is designed to output an average number of particles, at constant volume and temperature, as a function of input chemical potential. In an experimental setup, however, one usually imposes an external pressure on the reservoir. In order to relate the

two quantities it is necessary to know some experimental or theoretical equation of state or use a technique such as the Widom test particle, described later in §3.2.2. In a low pressure regime, it is fairly common to simply assume that the reservoir behaves as an ideal gas and use the relation

$$\beta P^{\mathrm{id}} = \frac{\exp\left[\beta \mu^{\mathrm{id}}\right]}{\Lambda^3}. \tag{2.57}$$

2.3 Simulation of bulk phases

The objective of a Monte Carlo simulation is to provide information about the properties of macroscopic systems from a microscopic description of the configuration of constituent atoms, molecules or other small units. However, a computer cannot, in most relevant cases, be expected to handle more than a few thousand particles within reasonable simulation times. In a finite system of this size, a great fraction of the particles would be located at the surfaces and subject to very significant, and hard to quantify, boundary effects. This is problematic when one is only interested in the properties of the bulk phase. The usual solution is to simulate only a finite number of particles N, in a cell of volume V, and introduce periodic boundary conditions, which will effectively replicate the configuration an infinite number of times in each direction.

If the simulation cell is a cubic box of side L then, for each particle at position $\mathbf{r}_i$, there will be images in every neighboring box at positions $\mathbf{r}_i + \mathbf{n}$, where $\mathbf{n} = (n_x L, \, n_y L, \, n_z L)$ with n_x, n_y, n_z being three arbitrary integers. If the box is non-cubic, as is required, for example, by the anisotropic NPT algorithm of §2.2.5, then coordinates may simple be reduced to a cubic box of unit size. Other space filling polyhedra are also sometimes used [41]. If, during the course of the simulation, a particle leaves the box from one side, a replica will enter on the opposite side, which means the number of particles in the cell will remain constant.

The potential energy U of the total system must take into account interactions between all particles, not only those inside the central cell, but also all replicas, which are in infinite number. For pairwise additive potentials, this means that the total energy of the N-particle system is

$$U_{\mathrm{tot}} = \frac{1}{2} \sum_{\mathbf{n}}' \left\{ \sum_{i=1}^{N} \sum_{j=1}^{N} u_{ij}\left(\mathbf{r}_{ij} + \mathbf{n}\right) \right\}, \tag{2.58}$$

where $u_{ij}\left(\mathbf{r}_{ij}\right)$ is the potential energy between particles i and j, separated by the vector $\mathbf{r}_{ij} = \mathbf{r}_j - \mathbf{r}_i$. The prime over the sum means that for $\mathbf{n} = \overrightarrow{0}$, $i \neq j$.

The sum in equation (2.58) is, in principle, infinite but it is almost always limited to only the first box. This must be done with proper handling of the periodic boundary conditions by using the minimum image convention, wherein each particle in the box only interacts with

the nearest image of another particle.

2.3.1   Short-range interactions: the Lennard-Jones potential

For short-range interactions, the potential energy in equation (2.58) can be safely truncated by imposing that $u_{ij} = 0$ for particles that are separated by a distance larger than a finite cutoff length r_c. This introduces systematic errors which can be accounted by the inclusion of a correction term in the final energy. In three dimensions, that correction can be estimated by assuming a uniform distribution of the particles for distances larger than r_c, leading to [38]

$$U_{\text{tot}}\left(\mathbf{r}^N\right) = \sum_{i<j} u_{\text{trunc}}\left(r_{ij}\right) + \frac{N\rho}{2} \int_{r_c}^{\infty} u_{ij}\left(r\right) 4\pi r^2 \mathrm{d}r, \tag{2.59}$$

where u_{trunc} is the truncated potential and $\rho = N/V$ the density of particles in the system.

The standard Lennard-Jones (12-6) is an example of a short-range potential. It is spherically symmetric and defined for a pair of particles separated by a distance r as

$$u^{\text{LJ}}\left(r\right) = 4\epsilon \left[\left(\frac{\sigma}{r}\right)^{12} - \left(\frac{\sigma}{r}\right)^{6}\right], \tag{2.60}$$

where ϵ is the depth of the potential well, and σ the positive distance at which the energy is zero. The corrections to the total energy due to spherical truncation at distance r_c follows from equation (2.59)

$$U_{\text{corr}}^{\text{LJ}} = \frac{8N}{3}\rho\pi\epsilon\sigma^3 \left[\frac{1}{3}\left(\frac{\sigma}{r_c}\right)^{9} - \left(\frac{\sigma}{r_c}\right)^{3}\right]. \tag{2.61}$$

Similar corrections can be derived for the pressure [38]. For compatibility with the minimum image convention, the cutoff radius must be equal or less than half the smallest dimension of the cell.

2.3.2   Long-range interactions: the Ewald summation method

There is a class of potentials whose range of interactions is much larger than the scale of the simulation box and cannot be treated with the truncation and correction scheme of the previous section. In particular, if the strength of the interaction decays with distance at a slower rate than r^{-3} then the integral in equation (2.59) does not converge.

A common example of a long-range potential is the Coulomb interaction, which is proportional to r^{-1}. For two particles with charges q_i and q_j separated by a distance r, it is given by

$$u_{ij}^{\text{C}}\left(r\right) = \frac{1}{4\pi\varepsilon_0}\frac{q_i q_j}{r}, \tag{2.62}$$
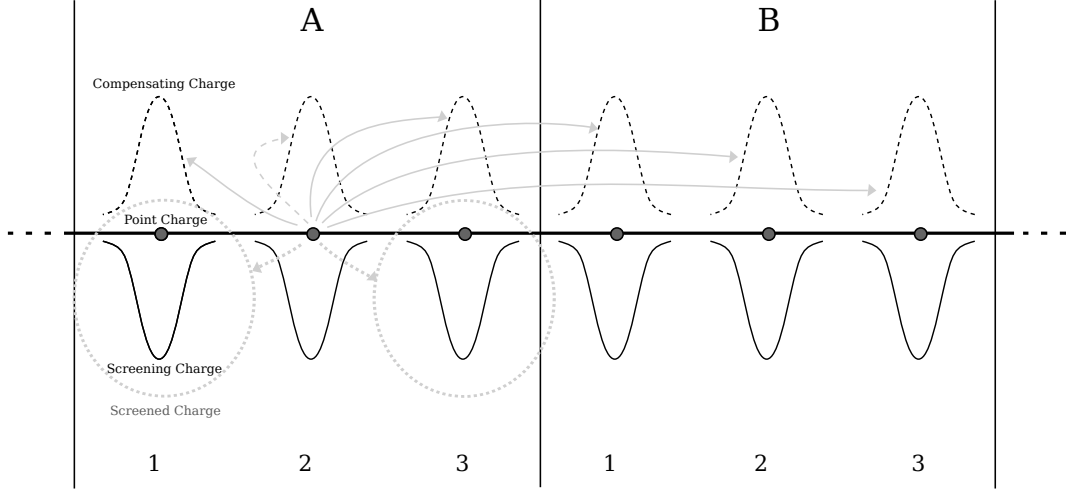
Figure 2.1: Visualization of the interactions in the Ewald summation method in one dimension. Three point charges, numbered 1 to 3 are represented in unit cell A and replicated in image B. Represented are also the diffuse screening (solid Gaussian curves) and compensating charges (dashed curves). The interactions of particle 2_A with the system are explicitly shown: interactions Φ_{dir} (gray dotted arrows) are limited to the two nearest images of the screened charges 1 and 3, 1_A and 3_A in this case; and the interactions Φ_{rec} (gray solid and dashed arrows) with an infinite number of periodic compensating Gaussians, 1_A, 2_A, 3_A, 1_B, 2_B, 3_B,... The contribution of the interaction of 2_A with its own Gaussian (dashed arrow) should be removed from the sum; this is the term $\frac{2\kappa}{\sqrt{\pi}}q_i^2$ in equation (2.65).

where ε_0 is the vacuum permittivity. In the following analysis, the constant $1/4\pi\varepsilon_0$ will be omitted for simplicity of notation. This class of long-range interactions also includes the dipole-dipole, charge-dipole and charge-quadrupole interactions.

The Ewald summation method [50], originally used in the study of ionic crystals, is a common technique for handling long-range interactions. A brief description of the ideas behind this method and some implementation considerations will be given in this section. A more detailed presentation can be found in the book by Frenkel and Smit [38] and in a series of papers by de Leeuw *et al.* [51, 52, 53] which provide an in-depth mathematical analysis of the method. These references also show how to apply this technique to handle charge-dipole, dipole-dipole and charge-quadrupole interactions.

The fundamental idea behind the Ewald method is that it is possible to split the electrostatic interaction between two charges into a short-range term, which is handled in the usual way of truncation, and a long-range term which is summed over in Fourier space, where it is rapidly convergent.

To achieve this, around every point charge q_i, a smoothly varying charge distribution, usually a Gaussian, of opposite sign $-q_i$ is created. The interactions between point charges are now mostly screened by this diffuse charge and drop rapidly with distance, meaning that they are now short-ranged. Let $\Phi_{\mathrm{dir}}(\mathbf{r}, \kappa)$ be the potential energy due to a partially screened unit charge and all of its images, measured at a distance $\mathbf{r}$ from the charge site. In these conditions, it can be shown that

$$\Phi_{\text{dir}}\left(\mathbf{r}, \kappa\right) = \sum_{\mathbf{n}}{}' \frac{\text{erfc}\left(\kappa \left|\mathbf{r} + \mathbf{n}\right|\right)}{\left|\mathbf{r} + \mathbf{n}\right|}, \tag{2.63}$$

where κ is an adjustable parameter related to the width of the Gaussian charge distribution. The prime in the sum over $\mathbf{n}$ means that for $\mathbf{n} = \vec{0}$, $\left|\mathbf{r}\right| \neq 0$, so as to ignore interactions between a particle and itself. $\text{erfc}\left(x\right) = 2\pi^{-1/2} \int_x^\infty \exp\left(-t^2\right) \mathrm{d}t$ is the complementary error function and here returns the fraction of the charge which is not screened by the Gaussian. It drops rapidly with x so if the parameter κ is chosen to be large enough, a simple minimum image convention can be applied to calculate $\Phi_{\text{dir}}\left(\mathbf{r}, \kappa\right)$, ignoring all distant images. The subscript *dir* is meant to convey the fact that the sum in equation (2.63) is carried over in direct space.

The useful, yet artificial, introduction of the screening Gaussian charge $-q_i$ around each site must be compensated. In order to do this, diffuse charges with the same distribution but opposite sign, $+q_i$, are introduced at the same locations. Their effect on the potential field is calculated and added to the final result, canceling the spurious contribution due to the screening charges. The advantage of this construction is that the sum of smoothly varying and periodic Gaussian functions converges rapidly in reciprocal space and can be calculated by performing a Fourier transform. Let $\Phi_{\text{rec}}\left(\mathbf{r}, \kappa\right)$ be the potential energy due to a unit Gaussian charge, and all of its images, measured at a distance $\mathbf{r}$ from the charge site. It can be shown that

$$\Phi_{\text{rec}}\left(\mathbf{r}, \kappa\right) = \frac{4\pi}{V} \sum_{\mathbf{k} \neq 0} \frac{\exp\left(-k^2/4\kappa^2\right)}{k^2} \exp\left(i\mathbf{k} \cdot \mathbf{r}\right), \tag{2.64}$$

where $\mathbf{k}$ are vectors in reciprocal space (for the cubic box, $\mathbf{k} = \frac{2\pi}{L}\left(k_x, k_y, k_z\right)$ with k_x, k_y, k_z arbitrary integers) and $k = \left|\mathbf{k}\right|$ The label *rec* is used to indicated that the sum is carried over in reciprocal space.

The final energy of particle i becomes

$$U_i^{\text{C}} = q_i \left\{ \sum_{j \neq i} q_j \Phi_{\text{dir}}\left(\mathbf{r}_{ij}\right) + \sum_j q_j \Phi_{\text{rec}}\left(\mathbf{r}_{ij}\right) - \frac{2\kappa}{\sqrt{\pi}} q_i + U_i^{\text{surf}} \right\}, \tag{2.65}$$

where the term $\frac{2\kappa}{\sqrt{\pi}}q_i^2$ is introduced to compensate for the inclusion, in the second sum, of the interaction Φ_{rec} between the charge q_i and its own compensating Gaussian $+q_i$ [38]. The last term in equation (2.65), U_i^{surf}, is known as the surface term and was derived by de Leeuw *et al.* [51]. It depends quadratically on the dipole moment of the unit cell, as well as the boundary conditions at the infinite and external dielectric constant. For an ionic system, where the infinite number of cells is summed in spherical shells around the unit box[1], and

---

[1]In equation (2.58) this corresponds to first taking the term $\mathbf{n}/L = (0, 0, 0)$; then $(\pm 1, 0, 0)$, $(0, \pm 1, 0)$ and $(0, 0, \pm 1)$; then $(\pm 1, \pm 1, 0)$, etc.

which is embedded in a medium with dielectric constant ϵ_s, the term is [54]

$$U_i^{\text{surf}} = \frac{4\pi}{(2\varepsilon_s + 1) V} \left[\mathbf{r}_i \cdot \sum_{j=1}^{N} q_j \mathbf{r}_j \right].$$ (2.66)

This term is usually ignored in simulations which is equivalent to considering that the system is embedded in a conductor ($\varepsilon_s = \infty$).

The total energy of a system of N charges is obtained by summing equation (2.65) over all particles and dividing by 2 to compensate counting of repeated pairs. While U^{C} is independent of the parameter κ, this must be adjusted in order to minimize the extent of the sum in real and reciprocal spaces. It should be large enough that the term in real space can be limited to the minimum image terms, but not too large that many k-vectors are needed for the sum over Fourier-space. Tests should be carried at the beginning of the simulation to optimize the value of κ.

Other methods for handling long-range interactions are available in the literature, such as, the reaction field method [41], the fast-multipole method [55, 56, 38], or the particle-particle/particle-mesh algorithm [57] and related techniques.

2.3.3 Electric field

In this work, the formalism of the Ewald method was extended to allow for the computation of the electric field in a system, which also drops slowly with distance (with r^{-2}).

The electric field at position $\mathbf{r}$ is given by the gradient of the electrostatic potential at that point,

$$\mathbf{E}(\mathbf{r}) = -\nabla U^{\text{C}}(\mathbf{r}),$$ (2.67)

which, using equation (2.65) and setting q_i to unity, gives

$$\mathbf{E}(\mathbf{r}) = -\sum_j q_j \nabla \Phi_{\text{dir}}(\mathbf{r} - \mathbf{r}_j) - \sum_j q_j \nabla \Phi_{\text{rec}}(\mathbf{r} - \mathbf{r}_j),$$ (2.68)

where $\mathbf{r}_j$ are the positions of the point charges. The surface term is ignored in this discussion, as it is not used in most works, including the present one.

The derivative of the direct summation term, Φ_{dir}, equation (2.63), assuming only the first image is considered (implying $\mathbf{n} = \overrightarrow{0}$ and the use of the minimum image convention), is

$$\begin{aligned} \nabla \Phi_{\text{dir}}(\mathbf{r}, \kappa) &= \frac{\partial}{\partial r} \left(\frac{\text{erfc}(\kappa r)}{r} \right) \hat{\mathbf{r}}, \\ &= -\left(\frac{\text{erfc}(\kappa r)}{r^2} + \frac{2\kappa}{\sqrt{\pi}} \frac{\exp(-\kappa^2 r^2)}{r} \right) \hat{\mathbf{r}}, \end{aligned}$$ (2.69)

where $\mathbf{r}$ is the position to evaluate the electric field in, relative to the location of a point charge, $r = |\mathbf{r}|$ and $\hat{\mathbf{r}} = \mathbf{r}/r$. Equation (2.69) is short-ranged and can be safely truncated.

For the derivative of the reciprocal term, Φ_{rec}, equation (2.64), it is first observed that

$$
\begin{aligned}
\nabla \exp\left(i\mathbf{k}.\mathbf{r}\right) &= i\exp\left(i\mathbf{k}\cdot\mathbf{r}\right)\mathbf{k} \\
&= -\sin\left(\mathbf{k}\cdot\mathbf{r}\right)\mathbf{k} + i\cos\left(\mathbf{k}\cdot\mathbf{r}\right)\mathbf{k}.
\end{aligned} \tag{2.70}
$$

Since only the real part of equation equation (2.70) is important, this leads to

$$
\nabla\Phi_{\text{rec}}\left(\mathbf{r},\kappa\right) = -\frac{4\pi}{V}\sum_{\mathbf{k}\neq 0}\frac{\exp\left(-k^2/4\kappa^2\right)}{k^2}\sin\left(\mathbf{k}\cdot\mathbf{r}\right)\mathbf{k}. \tag{2.71}
$$

In the work of Chapter 5, the electric field is an important component to the final potential energy of the system. The formalism developed in this section should provide an estimate of $\mathbf{E}$ that is more accurate and efficient than numerically solving the gradient of equation (2.67) or other approximation schemes. Additionally, equations (2.69) and (2.71) can be computed, with little overhead, on top of the usual calculations for the Ewald summation method, avoiding the need of pre-calculating the electric field and wasting large amounts of memory.

2.4   Simulations of molecular systems

When simulating molecules, rather than point particles, it is necessary to introduce new MC operations that can adequately sample the different molecular orientations and, for non-rigid molecules, the internal degrees of freedom. Additionally, the operations of displacement, insertion, removal and volume expansion are applied to the molecule as a whole.

In practice, it is convenient to redefine the coordinate positions of each atom in the system relative to the center of mass of its corresponding molecule. For a system of M molecules and a total of N atoms, the full configuration can be rewritten as

$$
\mathbf{r}^N \equiv \left(\mathbf{r}_{\text{cm}}^M, \mathbf{p}^{N_o}, \mathbf{p}^{N_1}, ..., \mathbf{p}^{N_M}\right), \tag{2.72}
$$

where $\mathbf{r}_{\text{cm}}^M$ are the coordinates of the centers of mass of the M molecules, and $\mathbf{p}^{N_i}$ is the set of positions of the N_i atoms of molecule i with respect to its center of mass. When calculating the interatomic interactions between the atoms in the system, the coordinates of each atom must be unwrapped back to global coordinates.

A displacement move is performed on $\mathbf{r}_{\text{cm}}^M$ only, changing the positions of a molecular center of mass, $\mathbf{r}_{\text{cm},i}$, randomly chosen from the set of M possibilities, while keeping the relative positions $\mathbf{p}^{N_i}$ unmodified.

An insertion operation attempts to add a whole molecule to the system, by putting a new center of mass in a random position in the box. Likewise, a removal trial operation will attempt to remove the molecule as a whole. The efficiency of an insertion/removal operation is

very low for large anisotropic molecules such as long alkane chains and aromatic compounds, and statistical biasing schemes are usually necessary to overcome the sampling problems. Fuchs and Cheetham review the most usual forms of biasing used in GCMC simulations of complex molecules [48].

A cell volume/shape update move operates on $\mathbf{r}_{cm}^M$ only, changing the positions of the center of mass of all molecules, while keeping their shape and orientation intact [38].

2.4.1 Rotational moves

There are different ways to generate a new random orientation for a rigid molecule but care must be taken in order to maintain detailed balance. Central to this discussion is the choice of variables used to describe the orientation of a molecule. For linear molecules, as is the case of hydrogen in Chapter 5, the natural choice is the normalized vector parallel to the molecular axis. Generating a new orientation is simply a matter of selecting a unit vector with uniform probability in all directions. This is not straightforward and different methods exist to achieve proper uniform random distribution. Details for the algorithm used in this work are given in Appendix A.

For non-linear molecules, the choice is more involved. The Euler angles are often used to study the dynamics of rigid bodies. They represent a sequence of three rotations about the Cartesian axes, in a specific order. To generate a small rotational displacement relative to a starting orientation, a simple recipe such as the one in equation (2.35) can be used to change each of the three angles by a random delta, while making sure that the angular densities are accounted for in either the selection or acceptance matrices [41]. An issue often associated with the use of Euler angles is the loss of a degree of freedom for certain angles, a problem known as "gimbal lock" in some fields [58].

A more numerically stable representation of orientation, and one that avoids expensive trigonometric calculations, is the unit quaternion, a four-element vector whose elements sum to 1:

$$\tilde{\mathbf{q}} = (q_0, q_1, q_2, q_3).$$ (2.73)

Alternatively, it can also be represented as a complex sum of a 3D vector $\mathbf{q}$ and a scalar q_0,

$$\tilde{\mathbf{q}} = q_0 + i\mathbf{q}.$$ (2.74)

Let $\mathbf{p}_j$ and $\mathbf{p}'_j$ be the positions of atom j relative to the molecular center of mass, respectively before and after a rotation given by the quaternion $\tilde{\mathbf{q}}$. The auxiliary complex quantities $\tilde{\mathbf{p}}_j = 0 + i\mathbf{p}_j$ and $\tilde{\mathbf{p}}'_j = 0 + i\mathbf{p}'_j$ are also defined. The position after the rotation is given by

$$\tilde{\mathbf{p}_j}' = \tilde{\mathbf{q}}\mathbf{p}_j\tilde{\mathbf{q}}^\star,$$ (2.75)

where $\tilde{\mathbf{q}}^\star = q_0 - i\mathbf{q}$.

A multiplication of two quaternions yields a new quaternion that represents the composite rotation. A rotation by an angle α around an axis with the direction of the unit vector $\mathbf{u}$ corresponds to the quaternion [59]

$$\tilde{\mathbf{q}}_{\mathbf{u},\alpha} = \cos\left(\frac{\alpha}{2}\right) + i\sin\left(\frac{\alpha}{2}\right)\mathbf{u}. \tag{2.76}$$

Generating a new rotational configuration from an old one can be achieved by first generating the vector $\mathbf{u}$ with uniform probability in the unit sphere, using the algorithms discussed in Appendix A, and then applying a small random rotation α,

$$\alpha = (2\mathcal{R} - 1)\,\delta\alpha, \tag{2.77}$$

where $\delta\alpha$ is the usual adjustable parameter. Equation (2.76) is then used to form the appropriate quaternion, which may then be applied to generate new atomic positions with (2.75).

Generating a completely new random orientation for a molecule is done by creating a new unit quaternion with equal probability in all four dimensional directions, which is equivalent to generating a point in a 4D hypersphere of radius 1 [60].

A particularly useful representation for an orientation in 3D space is a 3×3 rotation matrix, $\mathbf{R}$. This is similar to the scaling matrix h of §2.2.5, except now the transformation is purely rotational as opposed to the scale and/or shear transform of the symmetric h. Using this representation has the advantage that applying a rotation to a large number of particles can be accomplished with a simple matrix multiplication,

$$\mathbf{p}' = \mathbf{R}\mathbf{p}, \tag{2.78}$$

where $\mathbf{p}$ is a $3 \times N$ matrix where each column is the position of an atom relative to the molecular center of mass. Highly efficient matrix operations are readily available in a large number of programming languages, natively or as third party libraries. The rotation matrix, while useful, is never sampled directly, as its 9 elements are not independent. Instead, it can be constructed from (and deconstructed into) Euler angles and quaternions, making it ideal as an intermediary representation. The rotation matrix $\mathbf{R}$ is related to the elements of $\tilde{\mathbf{q}}$ by [59]

$$\mathbf{R}\left(\tilde{\mathbf{q}}\right) = 2\begin{bmatrix} q_0^2 + q_1^2 - \frac{1}{2} & q_1 q_2 + q_0 q_3 & q_1 q_3 - q_0 q_2 \\ q_1 q_2 - q_0 q_3 & q_0^2 + q_2^2 - \frac{1}{2} & q_2 q_3 + q_0 q_1 \\ q_1 q_3 + q_0 q_2 & q_2 q_3 - q_0 q_1 & q_0^2 + q_3^2 - \frac{1}{2} \end{bmatrix}. \tag{2.79}$$

2.4.2 Internal deformation

The rotational moves defined in the previous section are performed at constant molecular shape, that is, the molecule is treated as rigid while the operation is being carried. If the application under study requires that the molecule's shape changes during the course of the

simulation, then it is necessary to sample the internal positions of the atoms, relative to each other. This is made difficult by the fact that the potentials that describe intramolecular interactions are, commonly, more complicated than those that model intermolecular forces or interactions in simple atomic fluids. They are often described in terms of a different set of variables, such as bond lengths and bending and torsion angles, which are severely constrained to a set of very few favorable configurations. The simple displacement operation described in §2.2.3, applied to an individual atom of the molecule at a time, is not an adequate approach to sample this space. One could instead carry the sampling in the space of bond lengths and angles, by implementing MC operations which select a bond and change its length or angle relative to neighboring atoms. However, it is easy to see how a small local modification like this may cause large displacements of other atoms in the molecule, especially in chain molecules, leading to a very low acceptance ratio. Usually, some form of biasing is necessary to guarantee that the next generated conformation has a non-negligible Boltzmann weight. Configurational-bias Monte Carlo is a popular solution to this problem [38].

One interesting alternative is the Hybrid Monte Carlo method [6, 7]. The idea of this technique is to combine the power of Molecular Dynamics with the flexibility of the Monte Carlo method. In summary, a new configuration is generated by calculating the forces on the system, giving each particle some initial random velocity, and solving the usual equations of motion for a few timesteps. It can be shown that the acceptance probability of a move from state v to w proposed by this operation is simply given by

$$acc\left(v \to w\right) = \min\left[1, \exp\left\{-\beta\left(\Delta U + \Delta K\right)\right\}\right], \tag{2.80}$$

where ΔU (ΔK) is the change in the potential (kinetic) energy after the MD step. The Hamiltonian is, in principle, invariable under this operation, $\Delta U + \Delta K = 0$, but deviations naturally arise due to the discretization of the equations of motion. These are, nevertheless, exactly accounted for by the acceptance criterion of equation (2.80), so a timestep larger than what would be acceptable in an MD simulation may be used. The obvious constraint is that a timestep that is too large will lead to configurations with small final probabilities. The advantage of the Hybrid MC operation is that all particle positions are updated simultaneously, and the generated conformations are, in principle, close to the equilibrium configurations, meaning that the acceptance probabilities are controlled. The stochastic nature of the MC procedure is preserved by the random initialization of the momenta in every Hybrid MC trial operation.

Chapter 3

Phase Diagram Determination: the Case of the $n - 6$ Lennard-Jones System

3.1 Introduction

The simplified phase behavior of the Lennard-Jones system is illustrated in Figure 3.1, and is representative of many real-world single component systems, where a gas, liquid and solid phases can be identified, with transitional regions where two or more phases can coexist. This is by no means a comprehensive list of all possible states of matter, which may include several different solid structures, liquid-crystalline phases, magnetic ordering, etc. The gas-liquid-solid phase diagram of a model system, however, is a basic and fundamentally important problem, and its study has prompted the development of many methods and tools which are much more general.

Transitions from one of the phases depicted in Figure 3.1 into another are accompanied by a discontinuity in density and entropy, making them first-order phase transitions, according to the Ehrenfest classification, since these quantities can be expressed as first derivatives of the free energy. For the gas-liquid phase transition, the difference between the densities and entropies of the two phases is a function of temperature. This discontinuity is less pronounced as the temperature is increased and disappears at a critical temperature. As the system approaches this critical point it undergoes a second-order phase transition, which is characterized by anomalies (discontinuities or divergences) in the second derivatives of the free energy, the thermodynamic response functions. Above the critical temperature, there is no essential distinction between the gas and liquid phases. In this regime, one can continuously compress a very dilute gas phase until it freezes. The behavior of the gas-liquid transition contrasts to that of the fluid-solid transformation, which exhibits no critical point.
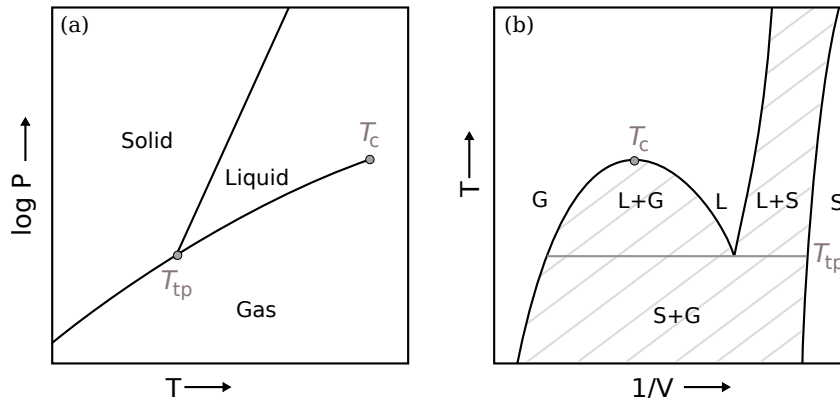
Figure 3.1: Representative phase diagram for a single component system. (a) Projection in a $P-T$ plane where the solid lines represent regions where two phases coexist. (b) Projection in a temperature vs inverse volume (or density) plane where solid lines are the phase boundaries and the shaded regions represent coexistence between two phases. At the triple point (T_{tp}) all three phases coexist. For temperatures above the critical temperature T_{c} there is no longer a distinction between the liquid and gas phases.

The determination of the phase behavior of a system starting from its macroscopic description is an important application of the Metropolis Monte Carlo method. In principle, one would select a thermodynamic state to investigate (a fixed set of values of some macroscopic variables, NVT or NPT for example) and run the appropriate MC algorithm to construct a Markov chain of states with the ensemble distribution. If the process is ergodic and carried for an infinitely long time, the most commonly sampled states would be those that are compatible with the most stable macroscopic phase, independent of the initial state of the chain. This means, that, for a system at very low pressures, microscopic states of low density and low internal energies, i.e., gaseous states, would be more commonly sampled; while for very high pressures, the most likely states would be those where the particles are arranged in a crystalline structure.

From this discussion, one might be tempted to conceive of a straightforward, but naive, way of constructing a phase diagram for a model system: simply initiate several simulations at various points in a range of temperatures, densities or pressures, wait long enough and observe as the system evolves into a gas, liquid, solid or other macroscopic phase. The obvious downfall of this approach is that a simulation can only run for a finite time which, when dealing with systems near phase boundaries, is often not enough for it to reach the true equilibrium phase for that thermodynamic input state. This is a result of the fact that the free energy landscape of the phase space near phase transition is rough, with lots of local minima and high barriers separating different domains. Most MC update rules are local, taking small steps in phase space, and traversing this space requires visiting inter-phase states at the top of these barriers, which, without some sort of biasing, have vanishingly small probabilities. The result is that the sampling will most likely become skewed towards a restricted region of the phase space, with a bias to the initial state. The generated chain of states, while valid in the sub-domain it visited, is not truly representative of the limiting distribution.

For a concrete example, consider the case of a system which is subject to relatively high pressures such that it would be found in a crystalline solid macroscopic phase, but is initiated in a random, liquid-like, configuration. It is easy to see how difficult it would be for the system to transform into a solid phase during the course of a simulation as this would require that all particles, initially disordered, spontaneously rearrange into an highly symmetrical crystalline structure. This transformation requires jumping over a very high free energy barrier (and thus traversing a low probability region of phase space) which results from the competition between entropy and internal energy of the system. The result is that the sampling would be limited to disordered states, even if the states corresponding to the ordered solid have higher probabilities in the ensemble distribution. The more thermodynamically stable phase would not be sampled.

Another example of this limitation can be found when dealing with states that fall inside the region of coexistence between two or more phases. As it will be explained in the next section, a system at these conditions is more stable when it separates into the constituent phases, which will coexist. This, in turn, introduces an interfacial free energy due to the surface separating the coexisting phases, which is non-negligible for finite systems. Because the size of simulated systems is necessarily limited, this increase in free energy may be higher than the decrease due to the phase separation. In that case, the phase-separated state has higher free energy, contrary to what happens at the thermodynamic limit, and the sampling is again unphysical. Even if this separation is possible in a finite system, or the system is explicitly prepared that way, it would still be necessary to know the the properties of this interface, i.e., its free energy, so that its effect can be discounted from the final result. Calculation of this interfacial free energy is involved (for a recent review, see [61] and references therein). A recent example is the work of Schrader *et al.* [62] who studied droplets of liquid surrounded by vapor using up to about 16 000 Lennard-Jones particles and a combination of grand-canonical and canonical MC and derived the interfacial free energy as a function of the droplet radius.

Given these difficulties, it is not surprising that methods have been explicitly devised to study phase coexistence and determination problems. Important reviews are given by Panagiotopoulos [63], who focuses on methods for the study of equilibrium of fluid phases, and, more recently, by Vega [64], with an emphasis on the fluid-solid and solid-solid transitions.

In §3.2 the general approach based on free energy calculations will be explained. Following that, §3.3 reviews specialized, but more direct, algorithms for the determination of phase equilibrium properties. The methodology based on free energy calculations is then applied to study the solid-fluid transition of the $n - 6$ Lennard-Jones system. The results of this work were published in reference [65].
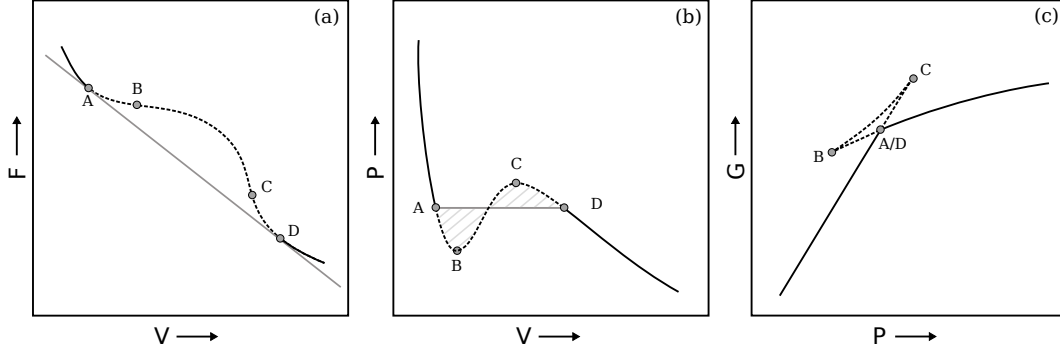
Figure 3.2: Behavior of thermodynamic potentials and variables of a system undergoing a first order phase transition. The dashed portions of the curves represent unstable regimes.

3.2 Phase determination from free energy calculations

For a system in the canonical ensemble, at given values of N,V and T, the most stable phase is the one that minimizes the Helmholtz free energy F, defined in equation (2.12) in terms of the canonical partition function. Likewise the dynamics of the system in the isothermic-isobaric ensemble will drive it to states where the Gibbs free energy G, equation (2.16), is minimized. From thermodynamics, it is also known that two phases, I and II, are in equilibrium when their temperatures, pressures and chemical potentials are the same,

$$T_{\mathrm{I}} = T_{\mathrm{II}}, \quad P_{\mathrm{I}} = P_{\mathrm{II}}, \quad \mu_{\mathrm{I}} = \mu_{\mathrm{II}}. \tag{3.1}$$

These are all well known results that follow from the second law of thermodynamics and can be used to determine the phase behavior at a given state. The discussion in what follows assumes a precise knowledge of the Helmholtz free energy function (this is, of course, not trivial). All other important quantities and relations can be derived from F.

The solid black curve in Figure 3.2(a) represents the Helmholtz free energy, F, of an homogeneous one component system as it is transformed from vapor to liquid at a constant, subcritical, temperature. The pressure, represented in Figure 3.2(b), follows from

$$P = -\left(\frac{\partial F}{\partial V}\right)_{NT}, \tag{3.2}$$

i.e., the slope, with opposite sign, of the free energy curve in (a). In Figure 3.2(c) the Gibbs free energy, G, is also given. This quantity is related to the Helmholtz free energy by the thermodynamic equation

$$G = \mu N = F + PV, \tag{3.3}$$

which shows that G is simply the intersect of the tangent of F with the y-axis in Figure 3.2(a).

It will now be shown that the region of the diagrams between points A and D, represented as dashed black curves, is thermodynamically unstable. First, since phase stability implies a

minimization of the Helmholtz free energy, it must be locally convex, i.e.,

$$\left(\frac{\partial^2 F}{\partial V^2}\right)_{NT} \geq 0. \tag{3.4}$$

Combining this with equation (3.2) one realizes that the pressure of a thermodynamically stable system decreases, or remains constants, with increasing volume, at constant temperature. Consequently, visual analysis of Figure 3.2(b) leads to the conclusion that the regions of the diagrams between B and C are unstable.

The second argument is based on the fact that, at any given state, it is possible to conceive of a configuration of the system that is made up of two macroscopic regions with different densities: one with high density, $\rho_{\mathrm{I}} = 1/v_{\mathrm{I}}$, and another with low density, $\rho_{\mathrm{II}} = 1/v_{\mathrm{II}}$, where v is a specific volume. If the system has a global density $\rho = 1/v$ between ρ_{I} and ρ_{II}, then the total specific volume is

$$v = \frac{N_{\mathrm{I}}}{N}v_{\mathrm{I}} + \frac{N_{\mathrm{II}}}{N}v_{\mathrm{II}}, \tag{3.5}$$

where N_{I} and N_{II} are the number of particles in the high and low density regions, respectively. Imposing $N = N_{\mathrm{I}} + N_{\mathrm{II}}$ leads to an expression known as the lever rule,

$$\alpha\left(v\right) = \frac{N_{\mathrm{I}}}{N} = \frac{v - v_{\mathrm{II}}}{v_{\mathrm{I}} - v_{\mathrm{II}}}, \tag{3.6}$$

which gives the fraction of the particles in phase I when the total system has specific volume v. Taking the limit of infinite system size, where interface effects can be disregarded, the free energy of the phase-separated system is simply

$$F' = \alpha F_{\mathrm{I}} + (1 - \alpha)\, F_{\mathrm{II}}. \tag{3.7}$$

Let point A in Figure 3.2 represent the high density phase, and point D the low density one. Then equation (3.7) plots the solid gray straight line in Figure 3.2(a). Since α only has meaning for values between 0 and 1, this straight line is not physically relevant for $V < V_A$ or $V > V_D$. As the free energy of this line is always lower than that of the black dashed curve corresponding to the homogeonous system, then one can conclude that, for volumes between A and D, the most stable configuration is one where the system will phase separate into two coexisting phases with different densities whose properties are set by the endpoints. Since the slope of F at points A and D is the same and equal to the slope of the straight line F', it can be concluded that the pressures of the two coexisting phases are equal and constant throughout the phase transition, fulfilling the condition of mechanical equilibrium. The tangent construction is also revealing with regards to the condition of chemical equilibrium. Since the tangent is the same at points A and D, the intersect of this line with $V = 0$, which yields G, or μN, is also the same. The whole segment between A and D is represented as a single point in the G vs P diagram of Figure 3.2(c).

This visual method of identifying phase transitions and coexistence properties is known as the common or double tangent construction. From an implementation point of view it might be more convenient (and accurate) to perform the search for the coexistence properties in the G vs P diagram, Figure 3.2(c), which only requires finding a single intersection point, after first obtaining $P(V)$ from derivation of F or other methods. This was the approach taken in this work.

As hinted above, the real practical problem lies with building these free energy curves. In general, these, and other related quantities such as entropy, are not directly available in a standard simulation (or in an experiment). The free energy is related to the whole volume of phase space available to a system, an cannot be expressed in terms of a canonical average that can be determined by MC.[1] Analytical or numerical methods of computing free energies are only available for the simplest of systems, such as the ideal gas (or a very dilute phase) or a solid of independent harmonically oscillating particles. These cases are, nevertheless, important since they can be used as references states. This is to be discussed further in §3.2.2.

While absolute free energies are hard to determine directly, it is feasible to calculate free energy *differences* between two systems at distinct thermodynamic states that are not too far apart. This is accomplished by realizing that derivatives of the free energy with respect to some variables can, in fact, be expressed as canonical averages. This is expanded upon in §3.2.1. If many simulations are setup spanning a wide range of thermodynamic states, these calculations may be chained together, and the free energy can be integrated along this path. Since only the relative free energy of the two phases is necessary to use the double tangent construction outlined above, one simply needs to construct a path between the two phases. However, there is the important caveat that these integration paths must be reversible [38]. This is not the case for the solid-fluid transition, which exhibits considerable hysteresis, and the consequence is that each phase must be studied independently on each side, without crossing the transitional region. In order to relate the two one must then have knowledge of the absolute values of the free energies, and this is where the reference states play an important role. For the liquid-gas phase transition, a direct path may be constructed joining the two phases, but it is commonly recommended that it goes over the critical temperatures, so as to avoid the first-order transition.

The present work focuses on the solid-fluid phase transition, and uses only canonical ensemble simulations followed by an analysis based on free energy calculations. This requires a large number of simulations but has the advantage of being straightforward, easy to implement and precise. The methodology used to determine the conditions of phase equilibrium of the two phases is thus summarized:

---

[1]The Helmholtz free energy may, in fact, be expressed as an ensemble average: $\beta \langle F_c \rangle = \ln \langle \exp (\beta E) \rangle_{\text{NVT}}$. However, since the MC procedure is optimized to sample states where $\exp (\beta E)$ is minimum, instead of maximum, this results in a very poor estimator of F.

1. calculate the absolute free energy of reference states, one (or more) for each phase;

2. construct reversible paths of simulations that connect the reference states to the states near phase boundaries, independently for each side;

3. determine the Helmholtz free energy curves as a function of volume, at constant temperature and number of particles;

4. use the double tangent construction to connect the independent curves and determine the coexistence properties such as densities, pressure and chemical potential.

3.2.1 Calculating free energy differences

Thermodynamic integration

Let two systems with labels 0 and 1 be simulated at different volumes, V_0 and V_1, with the same number of particles N and temperature T. The free energy difference between the two states can be expressed as an integration over the volume change,

$$F_1 - F_0 = \int_{V_0}^{V_1} \left(\frac{\partial F}{\partial V} \right)_{NT} \mathrm{d}V = - \int_{V_0}^{V_1} P \mathrm{d}V, \tag{3.8}$$

where the second equality follows from equation (3.2). A similar expression can be derived where the inverse temperature is the integration variable [38]. This method is known as thermodynamic integration and is not limited to physical paths. A particularly useful extension considers changes in the free energy between two systems simulated at the same thermodynamic state but with different potential functions, U_0 and U_1. If simulations are performed with a generalized potential,

$$\tilde{U} \left(\mathbf{r}^N, \lambda \right) = (1 - \lambda) U_0 \left(\mathbf{r}^N \right) + \lambda U_1 \left(\mathbf{r}^N \right), \tag{3.9}$$

at several different values of λ, then the free energy difference between the two systems is given by the integration of $(\partial F / \partial \lambda)$ for λ from 0 to 1, which can, in turn, be expressed as an ensemble average,

$$\begin{aligned} F_1 - F_0 &= \int_0^1 \left(\frac{\partial F}{\partial \lambda} \right)_{NVT} \mathrm{d}\lambda = \int_0^1 \left\langle \frac{\partial \tilde{U}}{\partial \lambda} \right\rangle_{NVT\lambda} \mathrm{d}\lambda \\ &= \int_0^1 \langle U_1 - U_0 \rangle_{NVT\lambda} \mathrm{d}\lambda, \end{aligned} \tag{3.10}$$

where $\langle ... \rangle_{NVT\lambda}$ represents an average over the samples from a simulation performed at constant NVT and λ.

Histogram reweighting

The histogram reweighting methods of Ferrenberg and Swendsen [66, 67] provide the means with which the results obtained from one or many simulations can be extrapolated to thermodynamic states outside of the simulated dataset. The methods originally made use of the accumulated energy histogram from a simulation to provide an estimate of the density of states of the system. This, in turn, can be used to derive the weight that the samples from this simulation would have when extrapolated to a new state. Since these weights are related to the ratio of the partition functions between the original and extrapolated states, the histogram reweighting technique also allows for the computation of free energy differences. Furthermore, by combining multiple simulations, it does this in a self-consistent way that minimizes statistical error.

In concrete terms, let subscript j denote a canonical simulation performed with N particles at a volume V and at an inverse temperature β_j. The probability of generating a configuration $\mathbf{r}^N$ in this simulation is given by the usual Boltzmann distribution,

$$p_j\left(\mathbf{r}^N\right) = \frac{e^{-\beta_j U\left(\mathbf{r}^N\right)}}{Z_j^c}, \tag{3.11}$$

where Z_j^c is the configurational partition function at inverse temperature β_j.

The probability of observing a configuration with energy E is

$$\begin{aligned} p_j\left(E\right) &= \int_{V^N} \delta\left[U\left(\mathbf{r}^N\right) - E\right] p_j\left(\mathbf{r}^N\right) d\mathbf{r}^N \\ &= \Omega\left(E\right) \frac{e^{-\beta_j E}}{Z_j^c}, \end{aligned} \tag{3.12}$$

where δ is the Dirac delta function and $\Omega\left(E\right) = \int_{V^N} \delta\left[U\left(\mathbf{r}^N\right) - E\right] d\mathbf{r}^N$ is the density of states with energy E. The density of states function Ω is independent of temperature, but changes with V and N.

Let h_j represent the histogram of energies obtained in simulation j, that is, $h_j\left(E\right)$ is the number of samples in the Markov chain, out of a total of M_j, whose potential energy is in the neighborhood of E, as defined by some bin-width. For increasingly larger simulation times, the normalized histogram, $h_j\left(E\right)/M_j$ approximates $p_j\left(E\right)$. This can be used to provide an estimate for the density of states of the system. Substituting $p_j\left(E\right)$ in equation (3.12) yields

$$\Omega\left(E\right) \approx \frac{h_j\left(E\right)}{M_j} e^{\beta_j\left(E - F_j^c\right)}, \tag{3.13}$$

where $F_j^c = -\ln Z_j^c/\beta_j$ is the configurational Helmholtz free energy of system j.

The ensemble average of an observable A may be written as a sum over energies,[2]

$$\langle A(\beta) \rangle_{NVT} = \frac{\sum_E A(E)\,\Omega(E)\,e^{-\beta E}}{\sum_E \Omega(E)\,e^{-\beta E}}. \tag{3.14}$$

Plugging in equation (3.13) into (3.14) yields an estimate of A at a generic inverse temperature β from the samples obtained at state β_j,

$$\langle A(\beta) \rangle_{NVT} \approx \frac{\sum_E A(E)\,h_j(E)\,e^{-(\beta-\beta_j)E}}{\sum_E h_j(E)\,e^{-(\beta-\beta_j)E}}, \tag{3.15}$$

where the sum is carried over the energy bins of the histogram.

The range of temperatures that can be extrapolated with statistical confidence with this method is necessarily limited. A simulation performed at inverse temperature β_j will generate a finite energy histogram, with clear bounds. Attempting to extrapolate the data to a new thermodynamic state with inverse temperature β that is too far from β_j requires that more weight is given to the tails of the histogram, which have poor statistics. This means that most of the sampled microstates in the simulation with β_j have very little actual weight in the distribution of state with β, leading to a poor estimation of the properties of this new state. It is thus important to guarantee that there is a significant overlap between the histograms of the two thermodynamic states. In other words, if one were to carry a simulation with inverse temperatures β and another with β_j, the visited regions of phase space should, to some extent, overlap.

This simple histogram method can be improved upon by combining the estimates of $\Omega(E)$ from multiple simulations, and providing the appropriate weight to each one. This is the multiple histogram [67] method, described next.

For a set of R simulations performed with the same volume and number of particles but at different temperatures, each one yielding an histogram $h_j(E)$, the combined estimate for the density of states is

$$\Omega(E) = \sum_{j=1}^{R} w_j(E)\,\frac{h_j(E)}{M_j}e^{\beta_j\left(E-F_j^c\right)}, \tag{3.16}$$

where $w_j(E)$ is the weight attributed to simulation j, which obeys $\sum_{j=1}^{R} w_j(E) = 1$ for any value of E. The weight function is chosen to minimize the variance of Ω and, for this case, that is achieved by setting [67, 68]

$$w_j(E) = \frac{M_j e^{-\beta_j\left(E-F_j^c\right)}}{\sum_{l=1}^{R} M_l e^{-\beta_l\left(E-F_l^c\right)}}. \tag{3.17}$$

The best estimate for the density of states using histograms from all simulations is then

---

[2]For simplicity, this discussion assumes that A can be expressed as a function of E. If that is not the case, a 2-dimensional histogram of pairs of values (E, A) must be accumulated and used instead

$$\Omega\left(E\right) = \frac{\sum_{j=1}^{R} h_j\left(E\right)}{\sum_{l=1}^{R} M_l e^{-\beta_l\left(E - F_l^c\right)}}, \tag{3.18}$$

which can be used in equation (3.14) to determine the value of A at an arbitrary temperature. The same statistical limitation as before applies, and the extrapolation temperature should not be too different from the simulated ones. In practice, one would use this method to study a continuous range of temperatures within the limits of a discrete dataset, and to enhance results obtained at one point with data from neighboring states.

The free energy at a given temperature follows from the density of states,

$$\begin{aligned} \beta F^c\left(\beta\right) &= -\ln Z^c\left(\beta\right) = -\ln\left[\sum_E \Omega\left(E\right) e^{-\beta E}\right] \\ &\approx -\ln\left[\sum_E \frac{\sum_{j=1}^{R} h_j\left(E\right) e^{-\beta E}}{\sum_{l=1}^{R} M_l e^{-\beta_l\left(E - F_l^c\right)}}\right]. \end{aligned} \tag{3.19}$$

Since F_l^c appears inside equations equation (3.18) and equation (3.19), these must be solved iteratively, given an initial guess. This method allows for the calculation of free energy differences, but it says nothing of its absolute values. The final result is a self-consistent measurement of the free energy of the system at several different temperatures, except for an additive unknown constant.

Histogram reweighting with Hamiltonian extrapolation

The multiple histogram method can be generalized to accommodate changes in other thermodynamic variables or parameters. In this work it is necessary, in order to calculate free energy differences, to combine simulations performed at different temperatures but also different volumes and even different interaction potentials. The extrapolation in temperature was covered in the previous section. An extension of this method that includes volume extrapolation is given by Ferreira and Barroso [43, 68]. This section will focus on the application of the multiple histogram method to systems at the same NVT conditions but where each one is assigned a different form of the potential energy function.

Let R independent canonical simulations be performed at equal NVT but each evolving according to a different potential energy U_j, $j = 1, ..., R$. The probability of generating a state with energy E in system j is given by equation (3.12) where U should now be labeled with the subscript j. Likewise, the density of states, Ω_j, is also different for each system and in a way that is difficult to correlate.

Let $\mathbf{r}_j^N$ be a microstate generated by the simulation with index j. The probability that this configuration has energy E_1 in system 1, E_2 in system 2,... and E_R in system R, i.e.,

$U_k\left(\mathbf{r}^N\right) = E_k$ for all k, is

$$
\begin{aligned}
p_j\left(E_1, E_2, ..., E_R\right) &= \int_{V^N} \left\{\prod_{k=1}^{R} \delta\left[U_k\left(\mathbf{r}_j^N\right) - E_k\right]\right\} p_j\left(\mathbf{r}_j^N\right) d\mathbf{r}^N \\
&= \Omega\left(E_1, E_2, ..., E_R\right) e^{-\beta\left(E_j - F_j^c\right)},
\end{aligned}
\tag{3.20}
$$

where a compound density of states is defined: $\Omega\left(E_1, E_2, ..., E_R\right)$ is the density of microstates that have energy E_1 in system 1, E_2 in 2, ..., E_R in $k = R$. and is independent of which system j is being considered, provided that the volume of integration is the same for all systems.

The notation can be simplified by defining an $R-$dimensional energy space. Let $S = \{E_1, E_2, ..., E_R\}$ denote a point in this space. The next step is to accumulate, for each simulation, a multidimensional histogram $h_j\left(S\right)$ of the sampled energies, i.e., the number of visited states in simulation j whose energies in each system of the series fall in the neighborhood of $\{E_1, E_2, ..., E_R\}$. As before, the approximation $h_j\left(S\right)/M_j \approx p_j(S)$ and equation (3.20) are used to provide one estimate for the multidimensional $\Omega\left(S\right)$. The best approximation to Ω will be a properly weighted average of the estimates from all simulations, that is,

$$
\Omega\left(S\right) = \sum_{j=1}^{R} w_j\left(S\right) \frac{h_j\left(S\right)}{M_j} e^{\beta\left(E_j - F_j^c\right)},
\tag{3.21}
$$

where w_j is the weight of simulation j and obeys the normalization condition $\sum_{j=1}^{R} w_j\left(S\right) = 1$ for all points S in the multidimensional energy space. By minimizing the variance of Ω as before, a similar result to equation (3.17) is obtained,

$$
w_j\left(S\right) = \frac{M_j e^{-\beta\left(E_j - F_j^c\right)}}{\sum_{l=1}^{R} M_l e^{-\beta\left(E_l - F_l^c\right)}},
\tag{3.22}
$$

with the density of states becoming

$$
\Omega\left(S\right) = \sum_{j=1}^{R} \frac{h_j\left(S\right)}{\sum_{l=1}^{R} M_l e^{-\beta\left(E_l - F_l^c\right)}}.
\tag{3.23}
$$

The configurational free energy of system k is obtained from the relation

$$
e^{-\beta F_k^c} = \sum_{S} \Omega\left(S\right) e^{-\beta E_k},
\tag{3.24}
$$

where the sum on S is carried over the entire R-dimensional domain of energies. Instead of computing multidimensional histograms, each individual measured state in each simulation, $\mathbf{r}_j^N$, can be used instead. Thus, the free energy of system k is given by the recursive equation

$$\beta F_k^c = -\ln\left\{\sum_{j=1}^{R}\sum_{\mathbf{r}_j^N}\frac{e^{-\beta U_k(\mathbf{r}_j^N)}}{\sum_{l=1}^{R}M_l e^{-\beta\left[U_l(\mathbf{r}_j^N)-F_l^c\right]}}\right\}, \tag{3.25}$$

where the sum is carried over all microstates $\mathbf{r}_j^N$ sampled in every run j and $U_k\left(\mathbf{r}_j^N\right)$ and $U_l\left(\mathbf{r}_j^N\right)$ are the energies that that microstate would have in systems k and l, respectively. The free energy can then be determined from $k = 1$ to R, except for an additive constant, which again means equation (3.25) can only be used to determine *relative* free energies. In practice, this is done by setting a reference free energy, say $F_1^c = 0$, and solving the remaining $R - 1$ equations iteratively until a convergence criterion is met.

Equation (3.25) calculates configurational free energies across different systems simulated at the same temperature, volume and number of particles. By comparison with the result of Ferreira and Barroso [43, 68], a general expression can be derived which allows for extrapolation in temperature and volume as well:

$$\beta_k F_k^c = -\ln\left\{\sum_{j=1}^{R}\sum_{\mathbf{r}_j^N}\frac{e^{-\beta_k U_k\left[\left(\frac{V_k}{V_j}\right)^{\frac{1}{3}}\mathbf{r}_j^N\right]}}{\sum_{l=1}^{R}M_l\left(\frac{V_l}{V_k}\right)^N e^{-\beta_l U_l\left[\left(\frac{V_l}{V_j}\right)^{\frac{1}{3}}\mathbf{r}_j^N\right]+\beta_l F_l^c}}\right\}. \tag{3.26}$$

The introduction of the scaling factors reflects the fact that simulations may now be performed at different volumes and that extrapolating one microstate $\mathbf{r}_j^N$, obtained at volume V_j, to a new volume V_k, requires rescaling of the particle coordinates by $(V_k/V_j)^{1/3}$, assuming cubic boxes.

3.2.2 Calculating absolute free energies

The absolute Helmholtz free energy of a system is obtained by integrating the Boltzmann factor over the whole volume of phase space that is available to it. For most systems, solving this problem directly is impossible, given the number of degrees of freedom. There are, however, cases where some simplifications are justifiable that greatly reduce the complexity of the task. Namely, two important cases are considered: the ideal or weakly interacting gas and the harmonic crystal. Computing the absolute free energy at an arbitrary thermodynamic state is accomplished by calculating the free energy relative to these reference states, using techniques like those described in §3.2.1.

Virial Expansion

For some thermodynamic state within the fluid region of the phase diagram, the free energy can be obtained starting from a very dilute gas phase and progressively increasing

the density. In the limit where the density is so low that the particles are completely non-interacting, the ideal gas regime, the free energy is given by equation (2.13). In practice, it is not necessary to go all the way down to the ideal gas limit, instead, it is sufficient to consider states of slightly higher densities, and include corrections to the free energy given by the first few terms of the virial expansion.

In the virial expansion scheme, the pressure of the system is given by

$$\beta P = \rho + B_2 \left(T \right) \rho^2 + B_3 \left(T \right) \rho^3 + ... + B_n \left(T \right) \rho^n, \tag{3.27}$$

where the first term on the right hand side is the ideal gas contribution and $B_n \left(T \right)$ is the virial coefficient of order n. The Helmholtz free energy can also be expressed as a virial expansion,

$$F \left(\rho, T \right) = F^{\text{id}} \left(\rho \right) + \frac{N}{\beta} \left[B_2 \left(T \right) \rho + \frac{B_3 \left(T \right)}{2} \rho^2 + ... + \frac{B_n \left(T \right)}{n-1} \rho^{n-1} \right], \tag{3.28}$$

where F^{id} is the ideal gas contribution, equation (2.13). The virial coefficients are directly related to the interaction between particles. The first coefficient, $B_1 = 1$, represents the single particle contribution (ideal gas term) and subsequent terms of order n correspond to the many-body interaction of a group of n particles. These coefficients are expressed in the form of cluster integrals [37].

First it is convenient to redefine the Boltzmann factor associated with the interaction between two particles (for a pairwise additive spherical potential) in terms of the Mayer $f-$function,

$$f_{ij} = e^{-\beta u(r_{ij})} - 1. \tag{3.29}$$

The second virial coefficient is obtained by integrating the two-particle term, f_{12} [69],

$$\begin{aligned} B_2 \left(T \right) &= -\frac{1}{2V} \int \int f_{12} \, \mathrm{d}\mathbf{r}_1 \mathrm{d}\mathbf{r}_2 \\ &= -\frac{1}{2} \int f_{12} \, \mathrm{d}\mathbf{r}_{12} \\ &= -2\pi \int_0^{+\infty} f \left(r \right) r^2 \, \mathrm{d}r, \end{aligned} \tag{3.30}$$

where, in the second line, the position of particle 1 was fixed and, in the last line, a spherical integration around the origin is carried. This can be easily solved by numerical integration.

For the third coefficient, the integration becomes [69]

$$
\begin{aligned}
B_3\left(T\right) &= -\frac{1}{3V}\int\int\int f_{12}f_{13}f_{23}\,\mathrm{d}\mathbf{r}_1\mathrm{d}\mathbf{r}_2\mathrm{d}\mathbf{r}_3 \\
&= -\frac{1}{3}\int\int f_{12}f_{13}f_{23}\,\mathrm{d}\mathbf{r}_1\mathrm{d}\mathbf{r}_2.
\end{aligned} \tag{3.31}
$$

Instead of solving the 6-dimensional integral of equation (3.31), the equations of Barker [70] can be used instead,

$$
B_3\left(T\right) = -\frac{4\pi}{3}\int_0^\infty R^2 f\left(R\right) h\left(R\right)\mathrm{d}R, \tag{3.32}
$$

$$
h\left(R\right) = \frac{2\pi}{R}\int_0^{+\infty} rf\left(r\right)\mathrm{d}r\int_{|R-r|}^{R+r} uf\left(u\right)\mathrm{d}u. \tag{3.33}
$$

Higher order coefficients require solving integrals of increasing dimensionality. Barker *et al.* provide simplified expressions for the fourth [71] and fifth [70] virial coefficients of a spherical pairwise-additive potential and a numerical method to solve them. Results are provided for the $12-6$ Lennard-Jones in those works. More recently, Sun and Teja recalculated those coefficients for a more finely grained range of temperatures [72]. Recent calculations have found coefficients up to the 12-th order for the simplest potential models [73, 74, 75, 76]. A Monte Carlo sampling scheme known as Mayer sampling, proposed by Singh and Kofke [77, 78], can be used to determine higher order coefficients of general potentials. The basic idea is to prepare a set of particles in equal number to the degree of the cluster to be evaluated and then, using umbrella sampling, solve the integral with respect to a reference value. $12-6$ Lennard-Jones coefficients have been calculated up to the eighth order in this manner [79].

Virial coefficients, especially those of lower order which can be calculated with relative ease, have an important role to play in the development and validation of new potential models. Starting from an hypothetical new mathematical function describing the interaction between the elements of a system, a researcher can quickly extract important information about the bulk behavior, an equation of state for example, and test it against experimental data.

Widom test particle

The Widom test particle method [80] (also known as particle insertion method or simply Widom method) is a straightforward way of computing the chemical potential of a fluid, provided it is not too dense. For a simulation in the NVT ensemble, one can then obtain the Helmholtz free energy from the chemical potential by the thermodynamic relation of equation (3.3).

The chemical potential of a one-component system is

$$\mu \;=\; \left(\frac{\partial F}{\partial N}\right)_{VT} \approx -\frac{1}{\beta}\ln\left[\frac{Z\left(N+1,V,T\right)}{Z\left(N,V,T\right)}\right] \tag{3.34}$$

where the approximation holds for $N \gg 1$. Just like the partition function, the chemical potential may be split into ideal gas and excess terms,

$$
\begin{aligned}
\mu \;&=\; \mu^{\mathrm{id}} + \mu^{\mathrm{exc}} \\
&=\; -\frac{1}{\beta}\ln\left[\frac{Z^{\mathrm{id}}\left(N+1,V,T\right)}{Z^{\mathrm{id}}\left(N,V,T\right)}\right] - \frac{1}{\beta}\ln\left[\frac{Z^{\mathrm{exc}}\left(N+1,V,T\right)}{Z^{\mathrm{exc}}\left(N,V,T\right)}\right].
\end{aligned}
\tag{3.35}
$$

The ideal gas term is straightforward. From equations (2.7) and (2.10) and taking the $N \gg 1$ limit,

$$\mu^{\mathrm{id}} = -\frac{1}{\beta}\ln\left[\frac{V}{\Lambda^3\left(N+1\right)}\right] = \frac{1}{\beta}\ln\left[\Lambda^3\rho\right]. \tag{3.36}$$

For the excess part, the partition function is expanded into the integration in phase space,

$$
\begin{aligned}
\mu^{\mathrm{exc}} \;&=\; -\frac{1}{\beta}\ln\frac{\frac{1}{V^{N+1}}\int_V \mathrm{d}\mathbf{r}^{N+1}\exp\left\{-\beta U\left(\mathbf{r}^{N+1}\right)\right\}}{\frac{1}{V^N}\int_V \mathrm{d}\mathbf{r}^N\exp\left\{-\beta U\left(\mathbf{r}^N\right)\right\}} \\
&=\; -\frac{1}{\beta}\ln\frac{1}{V}\int_V \mathrm{d}\mathbf{r}_{N+1}\frac{\int_V \mathrm{d}\mathbf{r}^N\exp\left\{-\beta U\left(\mathbf{r}^N\right)\right\}\exp\left\{-\beta\Delta U\right\}}{\int_V \mathrm{d}\mathbf{r}^N\exp\left\{-\beta U\left(\mathbf{r}^N\right)\right\}} \\
&=\; -\frac{1}{\beta}\ln\frac{1}{V}\int_V \mathrm{d}\mathbf{r}_{N+1}\left\langle\exp\left\{-\beta\Delta U\right\}\right\rangle_{NVT},
\end{aligned}
\tag{3.37}
$$

where $\Delta U = U\left(\mathbf{r}^{N+1}\right) - U\left(\mathbf{r}^N\right)$ is the energy due to the interaction of particle $N+1$ with the others. In practice, the term inside the logarithm in equation (3.37) is solved by performing the following steps at regular intervals in the simulation: 1) randomly place a test particle with uniform probability in the cell volume, 2) calculate the interaction energy of the particle with the rest of the system, ΔU, and associated Boltzmann factor, and 3) discard the particle. The excess chemical potential is obtained by the simple average

$$\mu^{\mathrm{exc}} \approx -\frac{1}{\beta}\ln\frac{1}{M}\sum_{i=1}^{M}\exp\left(-\beta\Delta U_i\right), \tag{3.38}$$

where ΔU_i is the i-th sample of ΔU, out of a total of M.

When dealing with molecules with rotational degrees of freedom, rather than point particles, the integration should include additional angular variables. For molecules with internal interactions, the calculation is more involved [38]. The method was presented here in the context of NVT simulations but can be extended to other ensembles as well [38].

This method, and related methods based on particle insertion (grand-canonical MC, Gibbs ensemble MC) will only work for fluids that are not too dense. If the particles in the system are too tightly compacted, the energy of a particle inserted at random will most likely be high and the associated Boltzmann factor too small. The distribution is sharply peaked and difficult to sample. For solid phases, the problem is only aggravated by the fact that a new particle in the system would break the crystalline symmetry.

Einstein crystal method

The first method devised to calculate the free energy of a solid was the single occupancy cell method of Hoover and Ree [81], introduced in 1968. In it, each particle in the solid is confined to a unique artificial cell, which it cannot leave. The constrained solid can then be expanded to a dilute gas phase, of known free energy, in a reversible way. Today, however, the most common method of computing free energy of solids is the Einstein crystal method [82, 38], or Frenkel-Ladd method due to their authors. In this technique, the reference system is the Einstein crystal, a system of independent particles, each coupled to a lattice site by a classical harmonic potential. The energy of a such a system is

$$U^{\text{eins}} = U^{\text{lat}} + k \sum_{i=1}^{N} (\mathbf{r}_i - \mathbf{r}_{0,i})^2 = U^{\text{lat}} + k \sum_{i=1}^{N} \Delta \mathbf{r}_i^2, \tag{3.39}$$

where $\mathbf{r}_{0,i}$ is the position of the crystal lattice site for particle i and k is the spring constant, which in this case is assumed to be the same for all particles. U^{lat} is the potential energy of the lattice, $U^{\text{lat}} = U\left(\mathbf{r}_0^N\right)$, constant for a given density. Since the particles are independent, the Helmholtz free energy is straightforward,

$$
\begin{aligned}
F^{\text{eins}} &= -\frac{1}{\beta} \ln \left\{ \exp\left(-\beta U^{\text{lat}}\right) \left[\int_{-\infty}^{+\infty} \exp\left(-\beta k x^2\right) \mathrm{d}x \right]^{3N} \right\} + F^{\text{kin}} \\
&= U^{\text{lat}} - \frac{3N}{2\beta} \ln\left(\frac{\pi}{\beta k}\right) + F^{\text{kin}},
\end{aligned} \tag{3.40}
$$

where F^{kin} is the kinetic contribution to the free energy which depends on temperature only.

In order to relate this reference state to the real system of interacting particles in the solid phase, a reversible path must be created that gradually transforms one into the other. The method, proposed by Frenkel and Ladd [82], is based on the idea of performing simulations with a generalized potential which is a linear combination of the potential of interest and the harmonic oscillator, in the way of equation (3.9), with the parameter λ controlling the degree of coupling of the particles to the lattice sites. Several simulations are then performed, at the same NVT state, for values of λ between 0 and 1. The free energy is integrated as per equation (3.10), where now system $\lambda = 1$ represents the target system with potential energy

U and $\lambda = 0$, the Einstein crystal,

$$F = F^{\text{eins}} + \int_0^1 \left\langle U - U^{\text{eins}} \right\rangle_{NVT\lambda} \, \mathrm{d}\lambda. \tag{3.41}$$

Histogram reweighting can also be used to compute differences across the path of simulations with different values of λ, applying the method outlined in §3.2.1. This type of integration may be avoided altogether by an alternative method, proposed by Chang and Sandler [83], in which extended ensemble simulations are performed where λ is a dynamic variable and is allowed to take any value between 0 and 1, following the usual Metropolis MC acceptance scheme. The difference in free energy between the $\lambda = 0$ and $\lambda = 1$ states is related to the probability of finding the simulation at one state or the other, after properly accounting for the necessary added weights.

When λ approaches unity, the harmonic potential coupling the particles to their lattice sites is very weak, and the main driving force is the interparticle interaction, which poses no restriction on the drifting of the center of mass of the system in the simulation box. The consequence of this is that the mean-square particle displacement becomes of the order of L^2, where L is the side of the simulation box, resulting in large values of U^{eins} and a sharply peaked distribution of the integrand in equation (3.41) around $\lambda = 1$. The usual fix for this problem is to carry the simulations with the restriction of fixed center of mass [82, 38]. In this scheme, the positions of a particle relative to its lattice site is redefined as $\Delta \mathbf{r}_i = \mathbf{r}_i - \mathbf{r}_{0,i} - \Delta \mathbf{r}_i^{\text{cm}}$ where $\Delta \mathbf{r}_i^{\text{cm}} = \mathbf{r}^{\text{cm}} - \mathbf{r}_0^{\text{cm}}$ is the accumulated displacement of the center of mass of the system relative to the initial position.

When this restriction is applied, the integration of equation (3.41), returns the free energy difference between two systems with fixed center of mass. To obtain the free energy of the unconstrained real system, it is necessary to link the constrained and unconstrained Einstein crystals and also the constrained and unconstrained "real" systems. The derivation of the free energy deltas in each step is given in detail in [84] and [38]. Here, the final result for the free energy of the system of interest is presented,

$$\beta F = \beta \Delta F^{\text{cm}} + \beta F^{\text{eins}} + \ln \rho - \frac{3}{2} \ln N - \frac{3}{2} \ln \left(\frac{\beta k}{\pi} \right), \tag{3.42}$$

where ΔF^{cm} is the free energy difference calculated from the integral of equation (3.41) using the restriction of fixed center of mass. Polson *et al.* [84] also performed a study of the finite size effects on this calculation. Based on the work of Hoover [85], who had previously established that the leading contribution to the free energy per particle of the harmonic crystal is $\beta^{-1} \ln N / N$, they concluded that $\beta \Delta F / N$ should scale as $\ln N / N$. By analyzing equation (3.42) one then realizes that the quantity $\beta F / N + \ln N / 2N$ will be proportional to N^{-1}, if higher order contributions are ignored. This provides a straightforward way of

extrapolating the absolute free energy to the thermodynamic limit: 1) apply the method described in this section to obtain estimates of F for different system sizes; 2) plot $\beta F/N + \ln N/2N$ against N^{-1}, which will be approximately linear and 3) extract the value of the free energy at the origin of the x-axis, i.e., when $N^{-1} = 0$ or $N = \infty$, the thermodynamic limit.

A more detailed analysis of this method as well as its application to molecular solids is given in the book by Frenkel and Smit [38] and in the review of Vega *et al.* [64].

3.3   Other methods for phase determination

So far the discussion on phase determination has been centered on explicit free energy calculations. This requires 1) reference points where this free energy can be known analytically or determined using some approximation and 2) methods to integrate the free energy along a reversible path connecting these references to the states of interest. To avoid crossing regions of phase transitions, a different free energy branch (reference + path) is constructed for each phase, separately.

Notwithstanding the positive aspects of these indirect methods, namely their simplicity and precision, and their widespread use, there have been, over the decades, attempts to tackle this problem by taking a more direct approach, one which dispenses with the need of computing reference states and avoids the computational effort required to simulate these often long paths in thermodynamic space. This section presents some of the most interesting and popular techniques in this category.

Gibbs ensemble Monte Carlo

A popular simulation technique for the study of gas-liquid coexistence is the Gibbs ensemble Monte Carlo (GEMC) of Panagiotopoulos [17, 18, 86]. In GEMC two systems (or two phases) are simulated separately, with no interface, but they are allowed to exchange particles and volume at a constant total number of particles, total volume (or pressure [18]) and temperature. The chemical potential is the same for both phases, although the absolute value is unknown. In practice, this is achieved by implementing MC moves that 1) attempt to swap particles from one system to the other and 2) increase the volume in one system while decreasing the same amount in the other (when operating at total constant volume). This is done while also performing the standard displacement moves in each phase separately.

The result of this setup is that both the gas and liquid phases are being simulated in thermodynamic equilibrium with each other, but each at different densities. These are the coexistence densities characteristic of the fixed thermodynamic variables. By fitting the dependence of these densities with temperature by a power law, the results can also be extrapolated to yield an estimate of the critical point parameters.

Since this method relies on particle insertions (or rather, particle jumps between the two systems), it suffers from the same limitations as the Widom test particle, namely, it fails when

one of the phases is too dense, i.e., a solid or compact liquid.

Phase switch Monte Carlo

The phase switch Monte Carlo method, pioneered by Bruce and Wilding [19], is a method devised to study the solid-fluid transition directly. It makes use of extended sampling techniques to artificially drive the system to those regions of phase space where it can leap across the two phases freely, the so-called "gateway states". Both phases are visited in a course of a single MC simulation.

For this discussion, it is useful to start with a previous iteration of the phase-switch method: the lattice switch MC of Bruce *et al.* [87, 88]. In the lattice switch method, instead of a solid and fluid phases, the transition between two crystalline structures is studied. For the same reason that a spontaneous transformation from a liquid to an ordered crystal is impossible to observe in a standard MC simulation, so is the transition between two solid phases with different underlying structures. So, extended sampling methods are used to drive the system to gateway states which facilitate this transition.

First, the coordinate space to explore is redefined in terms of the displacements vectors relative to the lattice sites of some underlying structure α,

$$\mathbf{u}^N = \mathbf{r}^N - \mathbf{r}_{0,\alpha}^N, \tag{3.43}$$

where $\mathbf{r}_{0,\alpha}^N$ are the coordinate positions of the crystal lattice sites of phase α.

Now, an MC algorithm must be constructed which allows the system to transition from one phase to the other. For this, a new MC operation is defined, the lattice switch: given some state in phase α, obtain a new state in phase β by swapping the underlying lattice to $\mathbf{r}_{0,\beta}^N$ while keeping the displacement vectors $\mathbf{u}^N$ intact. The energy of the system will change by an amount ΔE as a result of the change in the relative positions between particles. The final configuration is very likely to have much higher energy, and so, the *unbiased* probability of acceptance, proportional to $\exp(-\Delta E)$, will be very low.

To address this problem, it is necessary to add a bias to the sampling. This is done by first introducing an order parameter. In the original works of Bruce *et al.* [87, 88], which was focused on a system of hard-spheres and compared the hcp and fcc phases, this parameter was the number of particle overlaps. Specifically,

$$\mathcal{M}\left(\mathbf{u}^N\right) = M\left(\mathbf{u}^N, \text{hcp}\right) - M\left(\mathbf{u}^N, \text{fcc}\right), \tag{3.44}$$

where $M\left(\mathbf{u}^N, \alpha\right)$ is the number of particle overlaps of the configuration with displacement vectors $\mathbf{u}^N$ in phase α. A system of hard spheres simulated in the hcp phase, for example, will, by design, generate states $\mathbf{u}^N$ with zero overlaps in this phase, $M\left(\mathbf{u}^N, \text{hcp}\right) = 0$. On the other hand, the same configuration will most likely have particle overlaps when the dis-

placement vectors are transfered to the fcc lattice, $M\left(\mathbf{u}^N, \text{fcc}\right) > 0$, the result of which is that this configuration of hard spheres will have infinitely large energy in this phase. From equation (3.44), it follows that typical configurations of the hcp phase will lead to negative values of $\mathcal{M}$. Likewise, typical configurations of the fcc phase will result in positive values of $\mathcal{M}$. Only when $\mathcal{M} = 0$ will there be no overlaps in either phase and the lattice switch operation can be accepted.

The missing piece in the scheme is a mechanism to direct the simulation to states where $\mathcal{M} = 0$. The solution of Bruce *et al.* is to use multicanonical sampling with a distribution that favors these gateway states. The introduced bias must be accounted for and corrected in the final result.

The ratio between the probability of finding the system in phase α and phase β is an estimate of the ratio between the partition functions of each phase, and thus, the free energy difference between them. The one with the lowest free energy is the most stable structure at the given conditions.

The lattice switch method was extended to soft-potentials by Jackson *et al.* [89].

In phase switch MC, this recipe is extended to the case where one of the phases is a fluid. For disordered phases, it is not possible to define the displacement vectors in terms of a "lattice" basis, the term $\mathbf{r}_{0,\alpha}^N$ in equation (3.43), because there is no underlying structure. Instead, a typical configuration of phase α, one that can be reached when simulating the system in that phase, is used. The displacement vectors $\mathbf{u}^N$ are then defined relative to the positions of the particles in this representative configuration.

In a fluid, however, particles may drift arbitrarily far from their representative positions, resulting in large values of some $\mathbf{u}$ which, when a phase switch to the solid is attempted, will result in a configuration with large deviations from the crystalline structure. To avoid this problem, an additional MC operation was suggested by Wilding and Bruce [19] in which two particles, in the same phase, will attempt to swap the identity of the representative site they are tethered to. The phase switch operation is carried out in the same way as before.

The order parameter M is defined as the number of overlaps that would occur if a phase switch was attempted, but now the authors included a dependence with the length of the displacement vectors as well, which is important for the fluid phase. The further a particle is from its representative position, the higher the value of M. Once again, a bias is introduced to favor states where $M = 0$.

Application of the phase switch method to soft potentials is due to Errington [90].

Constrained fluid λ-integration

In 2004, Grochola [91] proposed a method for determining the solid-liquid coexistence by calculating free energy differences across a reversible non-physical path which explicitly traverses the region of phase transition. This is accomplished in a 3-step process which directly

links the liquid and solid states:

1. Transform the liquid state into a weakly attractive arbitrary fluid, while contracting the cell volume. For this, a scaling factor λ is applied to the potential function which gradually decreases its magnitude down to 10% of its initial value.

2. Gradually turn on lattice contributions in the potential, regulated by another λ parameter, bringing the particles closer to the intended target lattice sites. The result is a constrained solid state. In this procedure, Grochola originally used a 3D Gaussian potential to bind the particles to the lattice sites.

3. Transform the constrained solid into the freely interacting solid state by decreasing the magnitude of the lattice contribution (reverse step 2) while simultaneously turning the real potential of the system back on (reverse step 1).

For each leg of the 3 part thermodynamic path, several simulations are performed for different values of λ and standard thermodynamic integration over the λ variable is performed to calculate free energy differences. This method has the conceptual advantage of relating the bulk solid and liquid states directly, without use of independent reference states in each phase. It has also been extended to calculate surface free energies [92].

Gibbs-Duhem integration

The Gibbs-Duhem integration method, proposed by Kofke [93, 94], is a numerical technique to trace the coexistence curve starting from a single known coexistence point, which must be calculated from some other method. It is based on the integration of the Clausius-Clapeyron equation, which states that, along the coexistence curve,

$$\frac{\mathrm{d}P}{\mathrm{d}T} = \frac{\Delta s}{\Delta v} = \frac{\Delta h}{T \Delta v}, \tag{3.45}$$
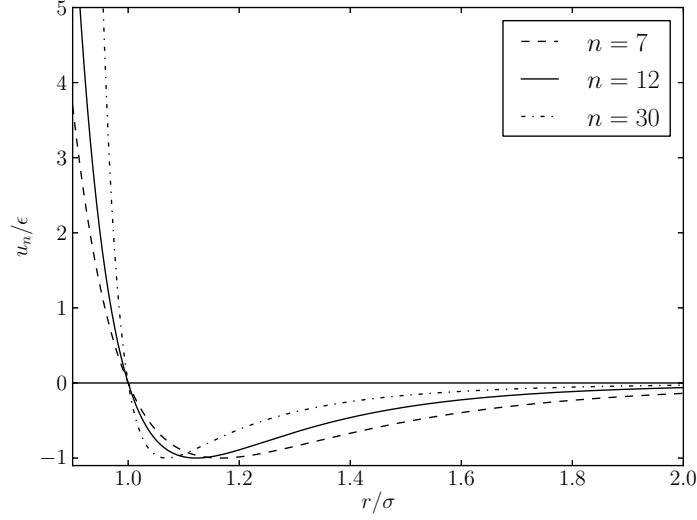
where Δs is the difference in specific entropies between the two phases, Δv the difference in specific volumes and $\Delta h = T \Delta s$ is the latent heat, per particle, of the phase transformation. Since the quantities on the right hand side of equation (3.45) are readily available in an NPT simulation, the equation can be integrated numerically to yield estimates for new points along the coexistence line.

The Clausius-Clapeyron equation is easily derived by recalling, from §3.2, that at coexistence, for a given P and T, the chemical potential of phase I and II is the same,

$$\mu_{\mathrm{I}}(P, T) = \mu_{\mathrm{II}}(P, T). \tag{3.46}$$

Moving along the coexistence line by an infinitesimal amount $\mathrm{d}P$ and $\mathrm{d}T$ leads to

$$\mu_{\mathrm{I}}(P, T) + \left(\frac{\partial \mu_{\mathrm{I}}}{\partial P}\right)_T \mathrm{d}P + \left(\frac{\partial \mu_{\mathrm{I}}}{\partial T}\right)_T \mathrm{d}T = \mu_{\mathrm{I}}(P, T) + \left(\frac{\partial \mu_{\mathrm{II}}}{\partial P}\right)_T \mathrm{d}P + \left(\frac{\partial \mu_{\mathrm{II}}}{\partial T}\right)_T \mathrm{d}T. \tag{3.47}$$

Figure 3.3: The $n-6$ Lennard-Jones potential as a function of interparticle distance, for some values of exponent n, in reduced units.

The Gibbs-Duhem equation, $N\mathrm{d}\mu = V\mathrm{d}P - S\mathrm{d}T$, is then used, and equation (3.47) becomes

$$v_{\mathrm{I}}\mathrm{d}P - s_{\mathrm{II}}\mathrm{d}T = v_{\mathrm{II}}\mathrm{d}P - s_{\mathrm{II}}\mathrm{d}T, \tag{3.48}$$

which is equivalent to equation (3.45).

An interesting extension of this method considers changes in the expression of the potential energy of the system by some parameter λ, and performs the integration along the coexistence line in (P, λ) or (T, λ) space. Originally, Agrawal and Kofke [95] used this method to trace the solid-fluid coexistence line of inverse power law potentials (IPL), $u_n^{\mathrm{IPL}} = \epsilon\,(\sigma/r)^n$, as a function of parameter n. In another work [96], the same authors studied the coexistence properties of the Lennard-Jones potential by starting from the IPL with $n = 12$ and progressively turning on the LJ attraction term. A derivation of the relevant equations for a potential of the type of equation (3.9) is given in [64].

The range of techniques available to study phase coexistence problems is vast and the discussion on this chapter is not meant to exhaust all possibilities. Other alternatives include the NPT + test particle method [97, 98], GCMC simulations near coexistence with histogram reweighting [99], methods based on estimation of the density of states [13, 100, 101], transition matrix Monte Carlo [15, 16, 102] or direct simulation of the two-phase system with an explicit interface [103, 104, 105].

3.4   Application to the $n-6$ **Lennard-Jones system**

In this work, the solid-fluid equilibrium properties of a system of particles interacting with the $n-6$ Lennard-Jones pair potential is investigated. This is a variation of the more common $12-6$ Lennard-Jones, previously defined in equation (2.60), with the difference that the repulsive term is now proportional to a generic n-th power of the inverse distance between particles,

$$u_n\left(r\right) = \epsilon A_n \left[\left(\frac{\sigma}{r}\right)^n - \left(\frac{\sigma}{r}\right)^6 \right], \tag{3.49}$$
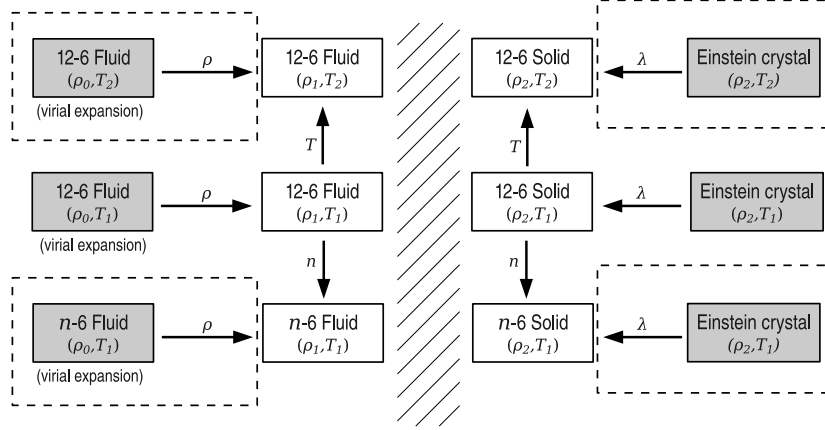
with

$$A_n = \frac{n}{n-6}\left(\frac{n}{6}\right)^{\frac{6}{n-6}}, \tag{3.50}$$

where ϵ is the depth of the potential well and σ is the finite value of the interparticle separation at which $u_n = 0$. The total energy of a configuration $\mathbf{r}^N$ is given by the sum over the pairs of particles. The value of the parameter n will define the steepness of the repulsive part of the potential, with more aggressive repulsion with increasing values of n, up to the limit $n = \infty$ (hard-spheres with a soft attraction term). As can be seen in Figure 3.3, this also has an effect on the attractive tail of the potential which approaches zero at a slower rate for smaller values of n.

The phase behavior of the monoatomic $12-6$ LJ has been well studied, with many results available in the literature for the coexistence properties in the various regions of the phase diagram. Different Monte Carlo methods have been employed for the determination of the vapor-liquid coexistence properties of this system, such as the Gibbs ensemble MC [17, 86], Gibbs-Duhem integration [94], grand-canonical ensemble with histogram reweighting [99] or the $NPT +$ test particle method [97, 98, 106]. Likewise, some data is available for the generalized $n-6$ potential in this region of the phase diagram [107, 108, 109, 110]. Comparatively, the solid-fluid transition has received much less attention. This is, no doubt, due to the difficulties associated with this region of the phase diagram mentioned in previous sections of this chapter, which means that no single methodology has emerged with clear advantage in terms of precision, efficiency and simplicity. Results are available for the solid-fluid coexistence properties of $12-6$ LJ system by methods such as phase switch Monte Carlo method [111, 90], constrained λ-fluid integration [91], Gibbs-Duhem integration [96], among others. Very recently, Pedersen *et al.* proposed the "pinned interface" method [105], which is based on direct simulation of solid and liquid phases with an explicit interface. Using this technique, Pedersen obtained melting and freezing lines for the $12-6$ LJ and provided a comparison with the results presented in this work, finding good agreement [112].

In 2003, Ge *et al.* [113], proposed a method to determine the freezing point at a given tem-

Figure 3.4: Conceptual representation of the methodology used in this work to compute free energies in thermodynamic space, with fluid phases on the left and solid on the right. The arrows represent the integration of the free energy along a path of simulations where the indicated variable changes. The filled boxes represent reference states where the absolute free energy can be determined. ρ_0 is some low density state where the virial expansion to the ideal gas law can be safely applied and ρ_1 and ρ_2 are arbitrary densities near the coexistence region, on each side. T_1 and T_2 are supercritical temperatures. The calculations enclosed within the dashed boxes are not strictly necessary, but are useful for consistency checks.

perature by observing the behavior of the pressure as a function of the strain rate, computed from non-equilibrium Molecular Dynamics (NEMD), which suffers a sudden discontinuity at the freezing density. This is then combined with equilibrium Molecular Dynamics to determine the corresponding melting density. This method has been recently applied to the $n-6$ LJ system by Ahmed and Sadus [114, 115].

Nevertheless, the most straightforward way to study solid-fluid coexistence is based on independent absolute free energy calculations on each phase, which avoids the region of phase coexistence altogether. Using the techniques outlined in §3.2, two (or more) free energy curves are constructed starting from independently calculated reference states and are then analyzed together with the double tangent construction, resulting in values for the thermodynamic variables at coexistence. This methodology has the advantage of being conceptually simple, relying on standard canonical ensemble simulations only and yielding coexistence properties with high precision. The phase diagram of the $12-6$ Lennard-Jones [116] and the fullerene-C_{60} [117] systems have been studied in this manner. In this work, this methodology is applied to study the solid-fluid transition of the $n-6$ LJ system, with n between 7 and 12. For $n=12$ the procedure is the same and the system is brought all the way down to the low density gas on one side and the harmonic crystal on the other. However, for n from 7 to 11, instead of using similar reference states, a shortcut is taken by using the $n=12$ system as the reference. The free energy difference due to the change in n is calculated using the generalization of the multiple histogram method that includes Hamiltonian extrapolation, described in §3.2.1. The diagram of Figure 3.4 shows a simplified overview of this process. Details are given in the following sections.

3.5 Simulation details

All simulations were performed in the canonical ensemble, at constant NVT as well as constant n and, where it applies, constant λ (the switching parameter in the Einstein crystal method). Unless otherwise stated, all the simulations were performed with $N = 500$ particles, as this was deemed sufficiently accurate to determine coexistence properties before [116]. After initial equilibration, 10^5 Monte Carlo steps (MCS) were carried, and sampling results were registered every 10 MCS. One MCS is comprised of N trial displacement moves, where particles are selected at random, rather than sequentially. Common MC simulation conventions are used throughout: cubic periodic boundary conditions, minimum image and potential truncation at half the box length. Following the standard practice, all quantities are presented in reduced units [41], which will be indicated by the superscript $*$, by setting ϵ, σ and k_{B} equal to one.

It is useful to define the auxiliary quantity

$$R_m^* \left(\mathbf{r}_j^N \right) = \frac{1}{2} \sum_{\alpha=1}^{N} \sum_{\gamma=1}^{N} \left(\frac{1}{r_{\alpha\gamma}^*} \right)^m , \tag{3.51}$$

where the sum is carried over all pairs of particles. The energy of configuration $\mathbf{r}^N$ in a system with exponent n is redefined as

$$U_n^* \left(\mathbf{r}^N \right) = A_n \left[R_n^* \left(\mathbf{r}^N \right) - R_6^* \left(\mathbf{r}^N \right) \right] , \tag{3.52}$$

and the instantaneous pressure, as given by the virial theorem [41, 38], is

$$P_n^* \left(\mathbf{r}^N \right) = \rho^* T^* + \frac{A_n}{3V^*} \left[n R_n^* \left(\mathbf{r}^N \right) - 6 R_6^* \left(\mathbf{r}^N \right) \right] . \tag{3.53}$$

In practice, R_m^* was truncated at a cutoff distance of half the side of the simulation box, which changes with density, $r_c^* = 0.5 \times (N/\rho)^{1/3}$, and long-range corrections were added at the end of the simulation. For the fluid side, these corrections follow the standard practice of assuming an uniform distribution of the particles for $r^* > r_c^*$, as explained in §2.3.1, and are given by

$$R_{m,\mathrm{corr}}^* = 2\pi \rho^* N \frac{1}{m-3} \left(\frac{1}{r_c^*} \right)^{m-3} . \tag{3.54}$$

For the solid phase, an alternative correction term was considered where all particles beyond r_c^* are positioned at the fcc lattice sites. This required knowledge of the untruncated lattice energy which was computed, for all n, by a procedure similar to that described by Stillinger [118]. The final value of the long-range corrections for simulations in the solid phase was taken as an average of the uniform and lattice contributions [116].

In every simulation, in every sample, the values of $\left\{ R_m^* \left(\mathbf{r}_j^N \right) \right\}$, for all m between 12 and

Table 3.1: Absolute configurational free energy per particle, f_c^*, at two thermodynamic states in the liquid phase, calculated from different methods, as described in the text: virial expansion ("virial exp."), varying density and varying temperature integration paths (paths "a" and "b") and multiple histogram method with Hamiltonian extrapolation ("from $n = 12$"). The values calculated relative to the $n = 12$ system use the following references: $f_c^*(n = 12) = -6.848897$ for state $(0.1, 2.0)$ and $f_c^*(n = 12) = 2.130$ for state $(1.0, 3.0)$.

(ρ^*, T^*)	therm. path.	$n = 12$	$n = 11$	$n = 10$	$n = 9$	$n = 8$	$n = 7$
(0.1, 2.0)	virial exp.	−6.848897	−6.89292	−6.94842	−7.02093	−7.12038	−7.26648
	from $n = 12$	...	−6.89274(1)	−6.94798(1)	−7.02011(2)	−7.11898(3)	−7.26430(5)
(1.0, 3.0)	path (a)	2.130(2)	1.581(1)	0.914(1)	0.074(1)	−1.038(1)	−2.599(1)
	path (b)	2.128(1)	1.582(1)	0.914(1)	0.074(1)	−1.032(1)	−2.596(1)
	from $n = 12$	...	1.584(2)	0.917(2)	0.078(2)	−1.030(2)	−2.593(2)

6 inclusive, were stored. It is then possible to extrapolate the energy of a sample obtained in run j (for which $n = n_j$) for all values of n. Extrapolating a sample from a volume V_j to a generic volume V is a simple matter of realizing the scaling relations of R_m^*,

$$U_n\left(\left(\frac{V}{V_j}\right)^{\frac{1}{3}} \mathbf{r}^N\right) = A_n\left[\left(\frac{V}{V_j}\right)^{-\frac{n}{3}} R_n^*\left(\mathbf{r}^N\right) - \left(\frac{V}{V_j}\right)^{-2} R_6^*\left(\mathbf{r}^N\right)\right]. \qquad (3.55)$$

With equations (3.55) and (3.26), the free energy can be integrated across any reversible path in thermodynamic space involving a change in volume, temperature or the parameter n.

3.6   Free energy calculations with n-extrapolation

This section presents test cases that validate the method outlined in §3.2.1 to compute the relative free energy of systems with $n < 12$ using the $n = 12$ as reference. Consistency checks similar to these were performed throughout the work.

In order to apply the multiple histogram method with Hamiltonian extrapolation, one standard canonical simulation is performed for each value of n between 12 and 7, all at the same NVT thermodynamic point. Equation (3.25) is then solved, iteratively, to determine free energies except for an additive constant. In practice, when calculating differences between systems with integer exponents n and $n + 1$, it may be necessary to also simulate with intermediate values of n. The step Δn should be chosen such that there is significant histogram overlap between consecutive systems in the series. It was found that $\Delta n = 0.5$ is enough for the range of densities and temperatures considered in this work, but higher values of temperature, density and number of particles would require increasingly smaller steps.

In Tables 3.1 and 3.2 some results are presented for this calculation. A comparison is made with the absolute free energy obtained from standard thermodynamic integration paths, calculated for each n independently. States are identified by a reduced density and temperature: (ρ^*, T^*).

Table 3.2: Absolute configurational free energy per particle, f_c^*, at two thermodynamic states in the solid phase, calculated from different methods, as described in the text: Frenkel-Ladd Einstein crystal method ("FL"); varying density and varying temperature integration paths starting at $T^* = 3.0$ (paths "c" and "d") and multiple histogram method with Hamiltonian extrapolation ("from $n = 12$"). The values calculated relative to the $n = 12$ system use the following references: $f_c^*\,(n = 12) = -2.538$ for state $(1.1, 1.0)$ and $f_c^*\,(n = 12) = 54.367$ for state $(1.8, 5.0)$.

(ρ^*, T^*)	therm. path.	$n = 12$	$n = 11$	$n = 10$	$n = 9$	$n = 8$	$n = 7$
	FL	$-2.538(2)$	$-2.861(2)$	$-3.290(2)$	$-3.881(3)$	$-4.737(4)$	$-6.0630(7)$
$(1.1, 1.0)$	path (c)	$-2.537(1)$	$-2.860(1)$	$-3.289(1)$	$-3.880(1)$	$-4.737(1)$	$-6.064(2)$
	from $n = 12$	...	$-2.861(2)$	$-3.290(2)$	$-3.882(2)$	$-4.740(2)$	$-6.068(2)$
	FL	$54.367(1)$	$50.060(1)$	$45.640(1)$	$40.995(2)$	$35.935(2)$	$30.102(4)$
$(1.8, 5.0)$	path (d)	$54.364(3)$	$50.058(3)$	$45.641(4)$	$40.998(4)$	$35.937(6)$	$30.107(9)$
	from $n = 12$	...	$50.060(1)$	$45.642(2)$	$40.997(2)$	$35.934(2)$	$30.095(2)$

For the fluid side (Table 3.1), at reduced density $\rho^* = 0.1$, the absolute free energy was determined from virial expansion up to the third coefficient, using the coefficients calculated in the manner described in §3.2.2, for each n independently. This is the first row in Table 3.1. The second line was obtained by calculating differences relative to the absolute value of the $n = 12$ system.

For the higher density liquid state, $\rho^* = 1.0$, series of NVT simulations were performed along an isotherm starting from $\rho^* = 0.1$ and $T^* = 2.0$ up to $\rho^* = 1.0$, followed by another set of simulations in an isochoric line connecting the path to the final state at $(\rho^*, T^*) = (1.0, 3.0)$. This path is labeled path (a) in Table 3.1. To check for consistency, a second path, (b), was built. This path follows a similar route but starts at a higher temperature: $(0.1, 4.0) \rightarrow (1.0, 4.0) \rightarrow (1.0, 3.0)$, where the absolute free energy of the starting point was again calculated from virial expansion. The free energy along both of these paths was integrated using the multiple histogram equation (3.26) at constant n. The construction of these two paths was repeated, independently, for each n. The last line in Table 3.1 was obtained from the integration over n, at fixed $(\rho^*, T^*) = (1.0, 3.0)$. The absolute free energies at this state obtained from two independent thermodynamic integration paths in (ρ^*, T^*) space and from the $n-$extrapolation method are in good agreement.

For the solid side, the Einstein crystal method of Frenkel and Ladd (FL), described in §3.2.2, followed by extrapolation to infinite system size using the corrections to the free energy expression of Polson *et al.* [84], was used to calculate the absolute value of f_c^* for each system independently. The solid structure considered in this work was fcc for all temperatures. This assumption is addressed in §3.9. The free energies of two states calculated in this manner are presented in Table 3.2. For comparison, the solid phase equation of state of van der Hoef for the $12 - 6$ LJ [119], with a recent adjustment of the reference parameter C by Mastny and de Pablo [120], yields a value of $f_c^* = -2.525$ at $\rho^* = 1.1$ and $T^* = 1.0$, which is similar to the result obtained in this work from the FL method, $f_c^* - 2.538(2)$.

The absolute free energy of a third, auxiliary, state, not explicitly represented, at $T^* = 3.0$

(and different densities for each n) was also calculated from the FL method. This state was used as the starting point of paths labeled (c) and (d) in table 3.2, which take different routes in (ρ^*, T^*) space to reach the final states, $(1.1, 1.0)$ and $(1.8, 5.0)$, respectively. This way, integration across systems at different volumes and temperatures is also checked for consistency against the Einstein crystal method. Once again, these values are consistent with each other and with those obtained relative to the $n = 12$ system from the multiple histogram method with Hamiltonian extrapolation used throughout this work.

3.7   Solid-fluid coexistence

3.7.1   Methodology

For the determination of phase coexistence properties between the fluid and crystalline solid, Helmholtz free energy curves, as a function of volume, were constructed for each phase independently. As discussed before, because the coexistence region cannot be crossed to yield their relative value, absolute free energy calculations must be carried out on reference points for the curves, on each side independently.

For the fluid phase of the $n = 12$ system, the reference state was determined by virial expansion up to the fifth order, using the coefficients from Barker [70], at $\rho^* = 0.1$ and $T^* = 2.0$. A series of 100 simulations at different densities was performed to connect that state to the one at $\rho^* = 1.0$, $T^* = 2.0$, resulting in the reduced absolute configurational free energy per particle, at that state, of $f_c^* = -0.1007(8)$. This estimate is consistent with that obtained from another path starting at $\rho^* = 0.1$ and $T^* = 4.0$. Furthermore, these calculations were repeated for system sizes of $N = 108$, 256 and 864. While the free energy obtained at that state using systems with 108 and 256 particles is considerably different from the estimate with $N = 500$, the result for $N = 864$ is within statistical error. It is therefore expected that this reference free energy on the fluid phase is not further affected by finite size effects.

For the solid phase, reference points for $n = 12$ were determined using the Einstein crystal method with a finite size study using up to $N = 864$ particles, as described in §3.2.2. This calculation was carried at the following thermodynamic points (ρ^*, T^*): (1.1, 1.0), (1.28, 2.0), (1.5, 3.0), (1.5, 4.0) and (1.5, 5.0). The corresponding reduced configurational free energies, f_c^*, were, respectively, -2.538(2), 5.185(1), 18.905(1), 24.1829(8) and 29.1232(7). Thermodynamic integration was performed across several paths in $(\rho^\star, T^\star)$ space connecting these states and the results confirmed the consistency of the calculated free energies.

For the other values of n, the reference free energies were calculated relative to the $n = 12$ system at the same density and temperature. Sometimes, due to the shifting of the freezing and melting lines to higher densities with decreasing n, it was necessary to extend simulations of the $n = 12$ system on the solid phase to higher densities so that the starting state of the
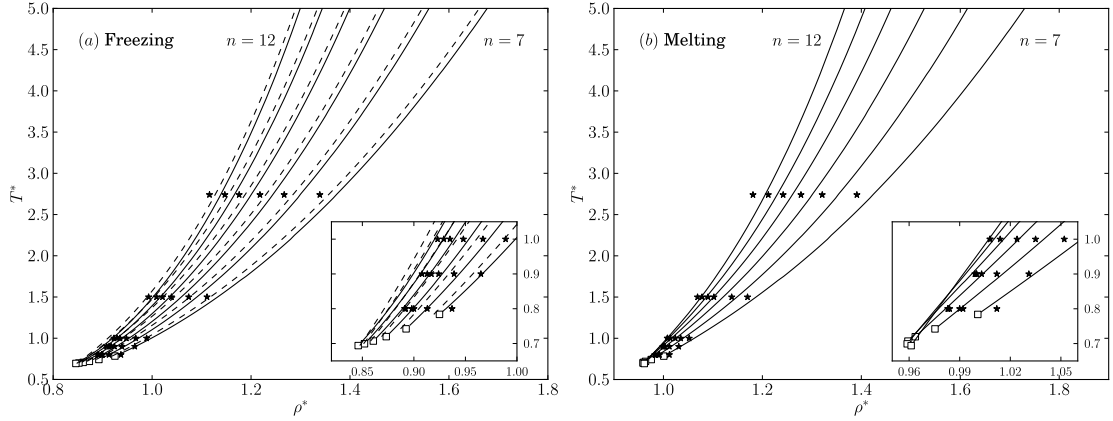
Figure 3.5: Solid-fluid transition densities for the $n-6$ Lennard-Jones. From left to right, the lines and symbols are those of the $n=12$ to $n=7$ systems, in sequence. Solid lines are the results from this work and the symbols ($*$) those of Ahmed and Sadus [114]. The open squares ($\square$) represent the triple points calculated here (Table 3.5). The dashed lines in (a) are the approximated freezing curves of Khrapak *et al.* [27], given by equation (3.58).

branch of the system with lower n did not fall inside the region of coexistence.

Once the absolute free energy was known for states close to coexistence on both phases, series of simulations were performed for all systems from $n=7$ to 12, at reduced temperatures $T^* = 0.75$, 1.0, 1.5, 2.0, 2.5, 3.0, 3.5, 4.0, 4.5 and 5.0. Each series consisted of simulations performed at different densities, with a step of $\Delta\rho^* = 0.01$, and for values near the freezing and melting lines. As explained before, they are further divided into independent fluid and solid branches. A simulation is defined as belonging to the liquid branch if it is initiated with a random configuration and solid if it is prepared with particles positioned at the fcc lattice positions. Due to the ergodic barrier it is unlikely that one phase will spontaneously transform into the other, but that can be controlled by keeping track of, for example, the pair distribution function. The generalized multiple histogram method was used to combine the simulations in each branch, and construct curves for the configurational free energy, $f_c^*(V^*)$, and pressure, $P^*(V^*)$, as functions of volume, at constant temperature, for each n. The reduced configurational chemical potential is given by

$$\mu^*(V^*) = f_c^*(V^*) + \frac{P^*(V^*)V^*}{N}, \tag{3.56}$$

and the coexistence properties are determined from the procedure described in §3.2. Additionally, to obtain results for an arbitrary T^* inside the range of temperatures considered, histogram reweighting of the data from the nearest series of simulations was used. The methodology used for the calculation of the errors in the coexistence properties is described in Appendix B.
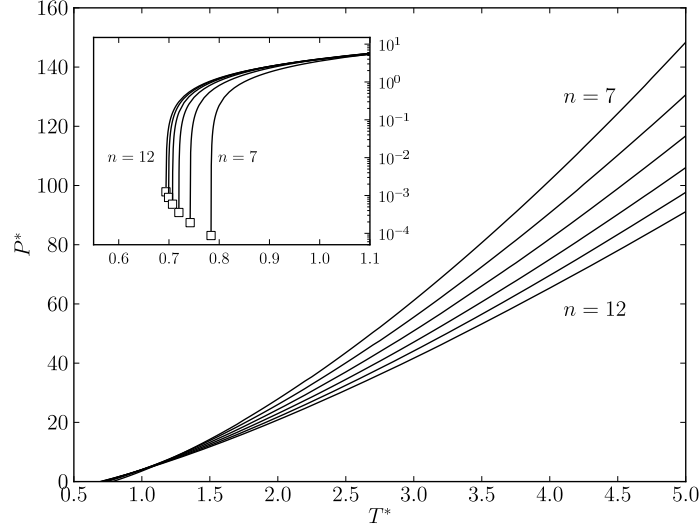
Figure 3.6: Solid-fluid coexistence pressures for the $n-6$ Lennard-Jones. For reduced temperatures $T^* \gtrsim 1.1$ the coexistence pressure increases monotonically with decreasing n. For lower temperatures (detail in inset on a log scale) the behavior is reversed. The open squares ($\square$) represent the triple points calculated here (Table 3.5).

3.7.2   Results

The solid-fluid coexistence properties obtained in this work are presented in Table 3.3 and figures 3.5 and 3.6. For a more complete view of the phase diagram of the $n-6$ LJ system, the vapor-liquid transition lines of Okumura and Yonezawa [109] are represented in Figure 3.7 alongside the melting and freezing curves calculated in this work.

In Figure 3.5 the coexistence densities obtained by Ahmed and Sadus [114], using an independent method [113], are also given. For medium to high temperatures ($T^* \gtrsim 1.0$) the densities obtained in this work, both on the solid and fluid side, are higher than those reported by these authors. For low temperatures, the behavior is reversed, with the coexisting densities dropping slightly faster with temperature. Despite these differences, the observed coexistence properties as a function of n follow the same pattern reported in [114]. The decrease in n, creating a softer atomic core, is accompanied by: (1) a shift of the melting and freezing lines to higher densities, a natural effect of a less repulsive potential; (2) a narrower coexistence region ($\rho_S^*(T^*) - \rho_F^*(T^*)$) and (3) an increase of the coexistence pressure for high temperatures ($T^* \gtrsim 1$) and the reverse for lower temperatures.

The type of potential truncation, cutoff distances and system size have been identified as sources of discrepancies between different estimates of solid-fluid coexistence properties of the $12-6$ LJ system [120, 26]. In this work, a variable cutoff distance is used that is equal to half the side of the simulation box. With $N = 500$ particles, this puts r_c at a minimum of about 3σ for the very highest densities, but, more frequently above 4σ, near triple point densities. This compares with $N = 2048$ and a fixed cutoff distance of 2.5σ in the work of Ahmed and

Table 3.3: Solid-fluid coexistence data for the $n-6$ Lennard-Jones systems: coexistence pressures (P^*), configurational chemical potentials (μ^*), densities (ρ^*), configurational free energies per particle (f_c^*) and potential energies per particle (u^*). For $T^* = 0.75$, the $n = 7$ system is already below the triple point temperature, so no real solid-fluid coexistence is observed.

				Fluid phase			Solid phase		
T^*	n	P^*	μ^*	ρ^*	f_c^*	u^*	ρ^*	f_c^*	u^*
0.75	12	0.66(2)	−3.49(2)	0.8626(9)	−4.252(2)	−6.162(5)	0.9694(6)	−4.167(2)	−7.232(3)
	11	0.61(2)	−3.83(2)	0.8676(9)	−4.538(2)	−6.453(5)	0.9674(6)	−4.465(2)	−7.482(3)
	10	0.54(2)	−4.29(2)	0.874(1)	−4.907(2)	−6.828(6)	0.9677(7)	−4.848(1)	−7.822(4)
	9	0.39(2)	−4.96(3)	0.883(1)	−5.404(2)	−7.331(6)	0.9704(8)	−5.364(1)	−8.297(4)
	8	0.11(2)	−6.00(3)	0.895(1)	−6.115(2)	−8.048(6)	0.9774(9)	−6.1046(9)	−9.001(4)
1.00	12	3.94(3)	0.84(3)	0.9201(7)	−3.439(4)	−6.137(3)	1.0073(6)	−3.069(4)	−7.091(2)
	11	4.00(3)	0.59(3)	0.9286(8)	−3.717(4)	−6.421(3)	1.0103(7)	−3.369(4)	−7.345(2)
	10	4.06(3)	0.24(3)	0.9392(8)	−4.080(4)	−6.784(3)	1.0161(7)	−3.753(4)	−7.689(2)
	9	4.06(3)	−0.31(4)	0.9534(9)	−4.572(5)	−7.285(3)	1.0251(8)	−4.274(5)	−8.166(2)
	8	3.97(4)	−1.20(4)	0.973(1)	−5.287(5)	−8.014(3)	1.0399(9)	−5.023(5)	−8.884(2)
	7	3.56(4)	−2.86(5)	0.999(1)	−6.424(5)	−9.172(4)	1.062(1)	−6.210(5)	−10.047(3)
1.50	12	11.75(3)	10.33(3)	1.0020(4)	−1.395(5)	−5.649(0)	1.0763(4)	−0.585(5)	−6.597(0)
	11	12.17(3)	10.36(3)	1.0168(5)	−1.615(5)	−5.881(0)	1.0867(4)	−0.846(6)	−6.810(0)
	10	12.69(3)	10.34(3)	1.0355(5)	−1.908(6)	−6.188(1)	1.1012(5)	−1.177(7)	−7.103(1)
	9	13.25(4)	10.18(4)	1.0591(6)	−2.326(7)	−6.622(1)	1.1207(5)	−1.638(8)	−7.526(1)
	8	13.86(5)	9.75(4)	1.0905(6)	−2.959(8)	−7.285(2)	1.1486(6)	−2.316(8)	−8.188(1)
	7	14.27(5)	8.57(5)	1.1325(8)	−4.033(9)	−8.410(2)	1.1872(7)	−3.452(9)	−9.318(2)
2.00	12	20.81(4)	20.53(3)	1.0646(4)	0.980(7)	−4.855(1)	1.1341(3)	2.179(7)	−5.866(1)
	11	21.79(4)	20.93(4)	1.0848(4)	0.850(8)	−4.995(2)	1.1508(4)	2.003(9)	−6.000(2)
	10	22.97(5)	21.36(4)	1.1105(5)	0.677(9)	−5.203(3)	1.1725(5)	1.77(1)	−6.197(2)
	9	24.36(6)	21.71(5)	1.1425(5)	0.40(1)	−5.518(4)	1.2012(5)	1.44(1)	−6.514(3)
	8	26.02(7)	21.89(6)	1.1847(6)	−0.07(1)	−6.049(5)	1.2397(6)	0.90(1)	−7.042(4)
	7	27.9(2)	21.50(16)	1.241(2)	−0.96(3)	−7.02(1)	1.293(2)	−0.06(3)	−8.03(1)
2.50	12	30.86(6)	31.21(5)	1.1165(4)	3.57(1)	−3.870(3)	1.1840(4)	5.15(1)	−4.965(3)
	11	32.50(7)	32.03(6)	1.1419(5)	3.57(1)	−3.905(5)	1.2059(5)	5.08(1)	−4.997(4)
	10	34.50(8)	32.94(7)	1.1732(6)	3.53(2)	−3.978(6)	1.2338(6)	4.98(2)	−5.072(5)
	9	37.02(9)	33.95(8)	1.2134(7)	3.44(2)	−4.134(7)	1.2706(7)	4.81(2)	−5.232(7)
	8	40.09(9)	34.88(7)	1.2651(6)	3.19(2)	−4.473(8)	1.3191(6)	4.48(2)	−5.580(7)
	7	43.5(1)	35.19(8)	1.3325(7)	2.52(2)	−5.256(9)	1.3837(7)	3.72(2)	−6.381(9)
3.00	12	41.67(6)	42.20(5)	1.1611(3)	6.31(1)	−2.753(4)	1.2277(3)	8.26(1)	−3.943(4)
	11	44.10(7)	43.48(6)	1.1911(4)	6.45(1)	−2.663(6)	1.2542(4)	8.31(2)	−3.853(5)
	10	47.12(9)	44.95(7)	1.2278(5)	6.58(2)	−2.579(7)	1.2879(5)	8.37(2)	−3.781(7)
	9	50.9(1)	46.63(9)	1.2749(6)	6.70(2)	−2.55(1)	1.3314(6)	8.34(2)	−3.759(9)
	8	55.5(1)	48.3(1)	1.3346(7)	6.69(2)	−2.67(1)	1.3884(7)	8.30(2)	−3.90(1)
	7	61.2(2)	49.6(1)	1.4135(9)	6.32(3)	−3.19(2)	1.4646(9)	7.83(3)	−4.44(2)
3.50	12	53.24(7)	53.51(6)	1.2009(3)	9.18(1)	−1.528(5)	1.2672(3)	11.50(1)	−2.818(5)
	11	56.51(9)	55.23(8)	1.2347(4)	9.46(2)	−1.301(8)	1.2979(4)	11.69(2)	−2.601(7)
	10	60.7(1)	57.33(9)	1.2767(5)	9.79(2)	−1.05(1)	1.3367(5)	11.92(2)	−2.358(9)
	9	66.0(1)	59.8(1)	1.3302(6)	10.15(2)	−0.80(1)	1.3870(6)	12.19(3)	−2.13(1)
	8	72.5(2)	62.3(1)	1.3983(7)	10.43(3)	−0.68(2)	1.4520(7)	12.35(3)	−2.02(2)
	7	80.7(2)	64.6(1)	1.4874(9)	10.40(3)	−0.90(2)	1.5387(9)	12.20(4)	−2.28(2)
4.00	12	65.37(8)	65.00(7)	1.2370(4)	12.15(1)	−0.232(7)	1.3029(4)	14.83(2)	−1.618(6)
	11	69.6(1)	67.24(9)	1.2744(5)	12.60(2)	0.15(1)	1.3373(5)	15.17(2)	−1.251(9)
	10	75.1(1)	69.9(1)	1.3210(6)	13.13(2)	0.59(1)	1.3810(6)	15.59(3)	−0.83(1)
	9	82.0(2)	73.1(1)	1.3801(7)	13.74(3)	1.06(2)	1.4371(7)	16.09(3)	−0.38(2)
	8	90.7(2)	76.7(1)	1.4560(8)	14.33(3)	1.47(2)	1.5100(8)	16.56(4)	0.00(2)
	7	101.7(3)	80.1(2)	1.555(1)	14.67(4)	1.57(3)	1.607(1)	16.78(5)	0.07(3)
4.50	12	78.0(1)	76.63(8)	1.2695(4)	15.19(2)	1.135(9)	1.3356(4)	18.23(2)	−0.356(8)
	11	83.4(1)	79.5(1)	1.3108(5)	15.82(2)	1.68(1)	1.3739(5)	18.75(3)	0.17(1)
	10	90.2(2)	82.8(1)	1.3619(6)	16.57(3)	2.32(2)	1.4221(6)	19.38(3)	0.79(1)
	9	99.0(2)	86.8(1)	1.4265(7)	17.46(3)	3.03(2)	1.4838(7)	20.13(4)	1.47(2)
	8	110.2(2)	91.4(2)	1.5099(8)	18.41(4)	3.76(3)	1.5644(8)	20.95(4)	2.16(2)
	7	124.3(3)	96.0(2)	1.618(1)	19.15(4)	4.21(3)	1.670(1)	21.54(5)	2.58(3)
5.00	12	91.2(1)	88.4(1)	1.2995(4)	18.29(2)	2.56(1)	1.3661(4)	21.71(2)	0.962(9)
	11	97.7(2)	91.8(1)	1.3441(5)	19.11(3)	3.27(1)	1.4076(5)	22.39(3)	1.65(1)
	10	106.1(2)	95.9(1)	1.3996(6)	20.10(3)	4.11(2)	1.4601(6)	23.24(4)	2.47(2)
	9	116.8(3)	100.7(2)	1.4696(8)	21.28(4)	5.09(2)	1.5273(8)	24.28(5)	3.41(2)
	8	130.6(3)	106.3(2)	1.5597(9)	22.59(5)	6.13(3)	1.6146(9)	25.44(5)	4.41(3)
	7	148.4(4)	112.3(2)	1.677(1)	23.79(5)	6.99(4)	1.730(1)	26.48(6)	5.22(3)
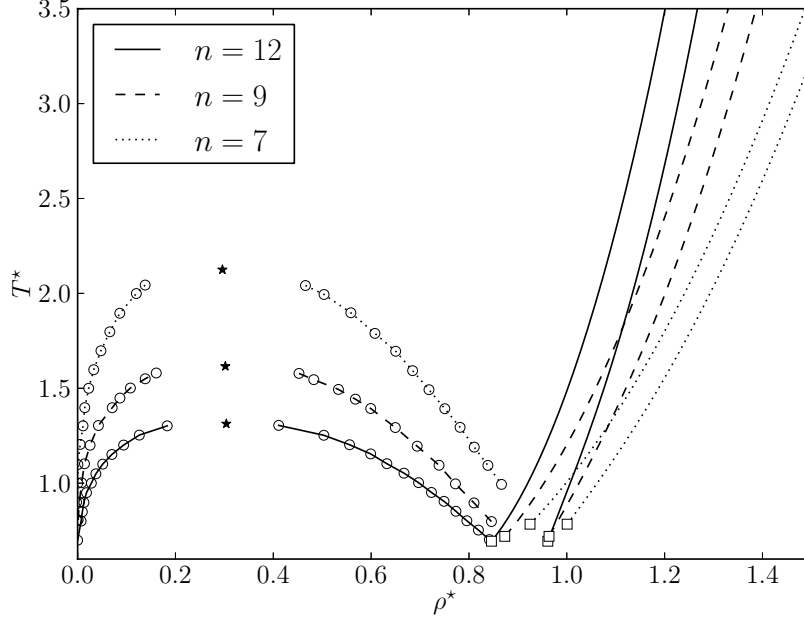
Figure 3.7: The vapor-liquid-solid phase diagram of the $n-6$ LJ system for three values of n, with solid-fluid lines given by the present results and vapor-liquid data from Okumura and Yonezawa [109] (open circles with guiding lines), including the critical points ($\star$).

Sadus [114]. 2.5σ is is a common choice for the cutoff radius, but may result in systematic errors on the estimated melting properties [120, 26]. For comparison, the present results for the $n = 12$ system are in good agreement with those obtained very recently by Pedersen with $r_c = 6\sigma$, using an independent method [112].

The effect of system size has been studied in this work, as mentioned before, in particular its effect on the absolute free energy of the reference states, which is the biggest source of error on the coexistence properties. For the solid phase, there is a strong dependence on system size (and also on the type of long-range corrections used) and this was addressed by extrapolating to the infinite system size. The reference free energy of the fluid phase is less sensitive and it was found that performing the calculation with more than 500 particles does not yield significantly different results.

An approximated method to locate the freezing line of the $n-6$ LJ system was recently proposed by Khrapak *et al.* [27] based on the observation that the normalized second derivative of the LJ interaction potential remains approximately constant along the freezing line, exhibiting little systematic dependence with temperature and density [121],

$$\mathcal{L} = u''\left(\Delta\right)\Delta^2/T = \text{const.}, \tag{3.57}$$

where $\Delta = \rho^{-1/3}$ is the mean interparticle distance. This leads to the following generic equation for the freezing curves of these systems,

Table 3.4: Solid-fluid coexistence densities obtained at moderate and high temperatures and comparison with results from the generic freezing equation (3.58), and the IPL system using data from [75]. Values in parentheses below the results are the percentual deviations of the estimates relative to the results of this work.

n	T^*	Fluid phase			Solid Phase	
		This work	Eq. (3.58)	IPL	This work	IPL
12	5.0	1.2995	1.2903 (0.7%)	1.2268 (5.9%)	1.3661	1.2725 (7.4%)
	100.0	2.6342	2.6369 (0.1%)	2.5943 (1.5%)	2.7387	2.6911 (1.8%)
9	5.0	1.4696	1.4579 (0.8%)	1.2715 (15.6%)	1.5273	1.3035 (17.2%)
	100.0	3.6360	3.6426 (0.2%)	3.4514 (5.3%)	3.7404	3.5381 (5.7%)

$$T^\star = \frac{1}{\mathcal{L}(n)} \left(\frac{n}{n-6}\right) \left(\frac{n}{6}\right)^{\frac{6}{n-6}} \left[n(n+1)\rho^{\star n/3} - 42\rho^{\star 2}\right]. \tag{3.58}$$

Furthermore, since the value of $\mathcal{L}$ is approximately constant along the freezing line it can conceivably be determined from the high temperature limit. In this region, the repulsive term is dominant, and the $n-6$ LJ potential may be approximated by an inverse power law (IPL), $u_n^{\mathrm{IPL}} = \epsilon(\sigma/r)^n$, after appropriate rescaling due to the absence of the multiplicative constant A_n. The freezing point of the IPL potential is then used to determine the constant $\mathcal{L}(n)$, which, given the assumptions in this discussion, should be transferable to the LJ form. By combining numerical data from different sources, the authors have arrived at the following values: $\mathcal{L}(12) = 290$, $\mathcal{L}(11) = 278$, $\mathcal{L}(10) = 267$, $\mathcal{L}(9) = 256$, $\mathcal{L}(8) = 246$ and $\mathcal{L}(7) = 237$. Substituting these values into equation (3.58) leads to the freezing curves which are plotted alongside the results of this work in Figure 3.5(a). They exhibit a very similar behavior even if skewed toward lower densities. Given the approximated nature of this method, the results are satisfactory.

It is expected that the agreement between equation (3.58) and the curves obtained from the methodology of the present study becomes better at higher temperatures [27, 121], as the system approaches the IPL limit. To show this, an independent series of simulations was performed at $T^* = 100$ and the solid-fluid coexistence properties was calculated as before. The results are presented in Table 3.4, for two values of n, along with a comparison with the freezing equation of Khrapak *et al.*, equation (3.58), and the coexistence densities of the purely repulsive IPL system with the same n, using data obtained recently [75]. At $T^* = 100$, equation (3.58) gives an accurate estimate of the freezing density, with a deviation of $\delta\rho^* = 0.003$ for $n = 12$ and 0.0066 for $n = 9$. Additionally, comparison with the corresponding IPL potential shows that the $n-6$ LJ system approaches a regime governed by purely repulsive interactions with increasing T. Furthermore, this approach is slower for less repulsive systems, with the $n = 9$ system exhibiting a larger relative difference to the IPL ($\sim 5\%$) compared with the $n = 12$ ($\sim 2\%$) at $T^* = 100$.

Table 3.5: Triple points properties of the $n-6$ Lennard-Jones system calculated in this work: temperatures (T_{tp}^*), pressures (P_{tp}^*), configurational chemical potential (μ_{tp}^*), and densities of the three coexisting phases (V - vapor, L - liquid and S - solid).

n	T_{tp}^*	$10^3 P_{\mathrm{tp}}^*$	μ_{tp}^*	$10^3 \rho_{\mathrm{V,tp}}^*$	$\rho_{\mathrm{L,tp}}^*$	$\rho_{\mathrm{S,tp}}^*$
12	0.694(1)	1.25(2)	$-4.398(4)$	1.83(3)	0.8460(5)	0.9612(3)
11	0.699(1)	0.89(2)	$-4.672(4)$	1.29(3)	0.8520(5)	0.9589(4)
10	0.707(1)	0.59(1)	$-5.020(4)$	0.84(2)	0.8606(5)	0.9593(4)
9	0.720(2)	0.355(9)	$-5.484(5)$	0.50(1)	0.8732(5)	0.9637(4)
8	0.742(2)	0.191(5)	$-6.139(5)$	0.259(7)	0.8924(5)	0.9753(4)
7	0.784(2)	0.087(3)	$-7.134(5)$	0.112(3)	0.9246(4)	1.0004(4)

3.8   Triple points

To determine the triple point parameters a numerical search was performed for the temperature $T_{\mathrm{tp}}^\star$ at which the vapor (subscript V), liquid (L) and solid (S) phases coexist simultaneously: $\mu_{\mathrm{V}}^*\left(T_{\mathrm{tp}}^*, V_{\mathrm{V}}^*\right) = \mu_{\mathrm{L}}^*\left(T_{\mathrm{tp}}^*, V_{\mathrm{L}}^*\right) = \mu_{\mathrm{S}}^*\left(T_{\mathrm{tp}}^*, V_{\mathrm{S}}^*\right)$ and $P_{\mathrm{V}}^*\left(T_{\mathrm{tp}}^*, V_{\mathrm{V}}^*\right) = P_{\mathrm{L}}^*\left(T_{\mathrm{tp}}^*, V_{\mathrm{L}}^*\right) = P_{\mathrm{S}}^*\left(T_{\mathrm{tp}}^*, V_{\mathrm{S}}^*\right)$. The free energy curves for the liquid and solid phases at a given T^* were calculated by histogram reweighting of the simulation series at the lowest temperature (but above T_{tp}^*). The vapor phase curve was obtained from virial expansion up to the third coefficient, which should be sufficiently accurate considering the small densities involved ($\rho_{\mathrm{V}}^* < 0.002$). The resulting triple point parameters are presented in Table 3.5. Details on the estimation of the error in these quantities are given in Appendix B.

Triple point temperature and densities have been obtained before for the $12-6$ Lennard-Jones. The results from the current work agree with those of references [116] ($T_{\mathrm{tp}}^* = 0.692$) and [120] ($T_{\mathrm{tp}}^* = 0.694$). Comparison with other earlier estimates can be found in [116].

Comparatively, much less data is available for the triple point properties of systems with other values of n. The results from this work are compared with those of Ahmed and Sadus [114], who extrapolated solid-liquid transition lines to low temperatures and collected vapor-liquid data from the literature. For this reason their results should only be taken as an approximation, as the authors themselves warn. In contrast, the present work uses a series of simulations at low T^* and histogram reweighting to determine the free energy curves at lower (but nearby) temperatures, coupled with a precise estimation of the vapor properties from virial expansion. This should result in a consistent and more accurate value of the triple point parameters.

Nevertheless, the agreement with the work of Ahmed and Sadus [114] regarding the triple point temperatures is quite good for systems with $n =$7, 8 and 9, for which they report, respectively, $T_{\mathrm{tp}}^* =$0.782, 0.748 and 0.718, mostly within statistical error of the current results. For $n =$10, 11 and 12 their estimates (respectively, $T_{\mathrm{tp}}^* =$0.689, 0.673 and 0.661) yield lower temperatures than the ones in Table 3.5. Additionally, these authors suggest that $T_{\mathrm{tp}}^\star$ increases linearly with $1/n$, while the present results show a clear non-linear behavior, as depicted in Figure 3.8. The triple point pressures determined in this work are much lower than those
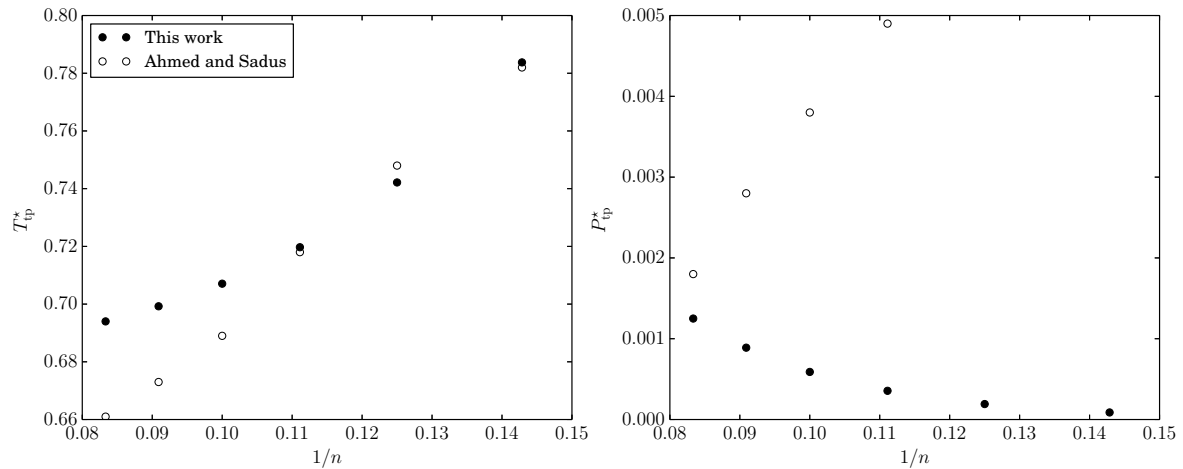
Figure 3.8: Triple point temperature (left) and pressure (right) of the $n - 6$ LJ system as a function of $1/n$, showing results for this work (filled circles) and by Ahmed and Sadus [114] (open circles).

reported in [114]. More significantly, the present results show that $P_{tp}^\star$ increases with n (it decreases non-linearly with $1/n$), not the other way around.

3.9   Solid-solid transition

The complete phase diagram of the purely repulsive inverse power law system has been determined with a high degree of precision [95, 122, 123]. It has been found that, for sufficiently soft potentials ($n \lesssim 7$), it freezes into a body centered cubic (bcc) phase, and transitions into the fcc phase by increasing the density or decreasing the temperature. Throughout this work it was assumed the stable structure of the $n - 6$ LJ solid is the fcc, but since this potential approaches an IPL with increasing temperatures, it is conceivable that there is a value of $T^\star$ above which some of the softer systems, in particular the $7 - 6$ LJ, exhibit a stable bcc phase.

To study this hypothesis, further free energy calculations were carried for the $n = 7$ LJ system, this time using the bcc lattice as the underlying structure of the solid phase and $N = 1024$ particles. The free energy curves for the bcc solid were constructed as before, using the Einstein method and a series of simulations in a density range near the melting line, for three different temperatures. These curves are plotted in Figure 3.9 alongside the fcc and fluid curves obtained before. The plots show that, at $T^* = 1.0$, the free energy of the bcc phase is always higher than the fcc. At $T^* = 5.0$, the free energies of both phases are already very close, but the fcc-fluid coexistence is still the most stable. At $T^* = 100$, the situation is reversed and the bcc phase has slightly a lower free energy. It seems likely, then, that the $7 - 6$ system freezes, for some $T^\star$ above 5.0, into a stable bcc phase. These results are preliminary and merely illustrative. Even at $T^\star = 100$, the relative difference in free energy between the fcc and bcc phases is very small, and sensitive to implementation details such as number of particles or type of long range corrections. No definitive conclusion could be drawn from the
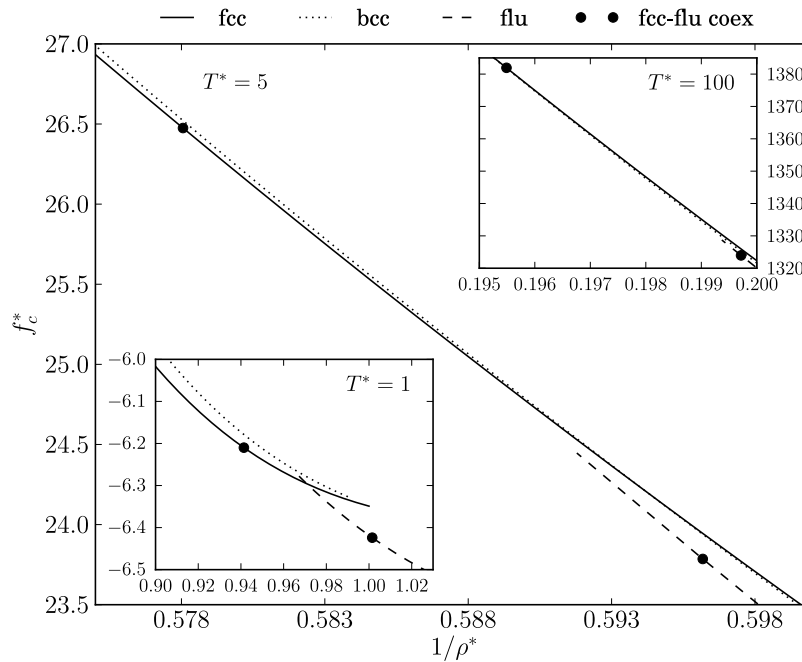
Figure 3.9: Comparison of the free energy curves of the fcc (solid), bcc (dotted) and fluid (dashed) phases for the $n = 7$ LJ system. The solid circles are the locations of the fcc-fluid coexistence points calculated in this work. For $T^* = 100$, the bcc free energy curve is slightly below that of the fcc phase.

data. Further work is required and alternative methods should be explored which do not rely on calculations relative to independent reference states.

Very recently, Khrapak and Morfill demonstrated that the fcc-bcc-fluid triple point of several model systems, when described in terms of two scaled coordinates related to the softness and strength of the interparticle potential, falls in a narrow region of the phase diagram [124]. Using this argument, the location of fcc-bcc-fluid triple point of the $7 - 6$ LJ system was approximately predicted at $\rho^\star \approx 3.4$ and $T^\star \approx 32.3$ [124].

3.10   Conclusions

In this chapter, the solid-fluid coexistence properties of a generalized form of the Lennard-Jones potential whose repulsive term is proportional to r^{-n} was studied by extensive free energy calculations. It was determined that the freezing and melting densities, for the same temperature, increase as the value of the exponent n is decreased. This result is in line with previous works by Ahmed and Sadus [114], using an independent technique based on NEMD, and Khrapak *et al.* [27, 121], who present approximated freezing curves for $n-6$ LJ potentials based on the observation of the constancy of the second derivative of this type of potentials at freezing. At the time of writing, to the best of this author's knowledge, no other sources were available for the solid-fluid coexistence properties of $n - 6$ LJ potentials.

In the current work, free energy curves were constructed independently for each phase and

connected to reference states of known free energy. Systems with $n < 12$ used the $n = 12$ LJ as reference. The free energy integration across several paths in (ρ^*, T^*, n) space was carried using a generalized form of the multiple histogram method of Ferrenberg and Swendsen, which combines the samples from multiple simulations, performed with different temperatures, volumes or potential functions, to give a self-consistent estimate for their relative free energies. Any integration method like this lends it self to two kinds of errors: (1) inaccuracies in the reference free energy; and (2) accumulated errors when traversing the path of simulations. These errors were estimated by the procedure given in Appendix B. Furthermore, as a control mechanism, new, redundant, paths in thermodynamic state were constructed starting on their own independently calculated reference states, and these were checked for consistency with the previous estimates. Although the bulk of simulations were performed with $N = 500$, attention was given to the system size effects on the free energy of the reference states, which were extrapolated to the thermodynamic limit.

The triple point parameters for the $n - 6$ LJ were also calculated with higher precision than previously available. The procedure relied on combining the free energy curves of the three phases and looking for the equilibrium conditions. The liquid and solid curves were constructed by extrapolation from the $T^* = 1.0$ series and the vapor's directly from virial expansion.

Chapter 4

Rotational Phase Transition of the Fullerene C$_{60}$ System

4.1 Introduction

The discovery of fullerenes is attributed to the research team of Kroto, Heath, O'Brien, Curl and Smalley, at Rice University, USA, who carried experiments to synthetize carbon clusters by laser vaporization of graphite targets and found a remarkably stable structure with 60 atoms [28]. They correctly predicted that the molecule had the structure of a truncated icosahedron, with 12 pentagonal and 20 hexagonal faces. In the original paper on Nature, they provided the famous visual analogy of the classic European football, which has the same geometric features. The C$_{60}$ molecule was baptized Buckminsterfullerene, in honor of Buckminster Fuller, for its resemblance with the geodesic domes designed and built by the renowned architect. For their discovery of fullerenes, Curl, Kroto and Smalley were jointly awarded the Nobel Prize in Chemistry in 1996.

The name "fullerene" refers to the larger class of cage-like all-carbon molecules, of which the C$_{60}$ is the most common. These molecules are frequently pictured as graphene sheets wrapped around in the shape of a hollow sphere or ellipsoid. Depending on the source, the term may sometimes refer to carbon nanotubes as well, similar molecules but with a cylindrical shape and open on both ends.

Each carbon atom in a fullerene molecule bonds trigonally with three others, forming two single bonds and one double bond, as in graphene. But, unlike graphene in its pure form, which consists only of 6-membered hexagonal carbon rings, some 5-membered pentagons must exist on these spherical molecules to allow for the curvature of the surface. Rings with less than 5 carbons are unlikely to occur [125]. There is a geometric imposition that all fullerene molecules with only pentagonal or hexagonal faces have exactly 12 pentagons and an arbitrary number of hexagons [125]. C$_{20}$ is the smallest possible construction, with 12 pentagons and no hexagonal face. To minimize local curvature, which in turn minimizes strain, no pentagonal
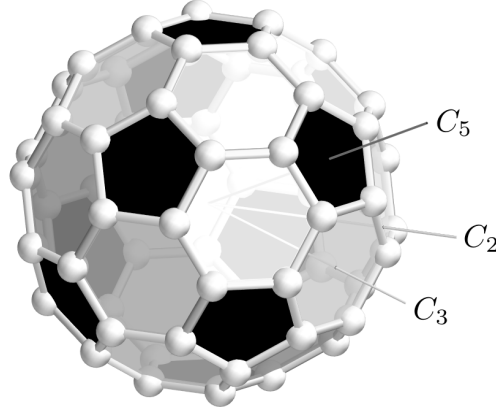
Figure 4.1: The fullerene C_{60} molecule with representative rotational symmetry axes.

face must be adjacent to another. The smallest fullerene to obey this rule is the C_{60} (12 pentagons and 20 hexagons), which explains why it is by far the most stable and common fullerene [126].

All the 60 carbon atoms in this molecule are equivalent, but there are two types of bonds: 60 single bonds (SB), that are shared between pentagonal and hexagonal faces, and 30 double bonds (DB), which are the edges common to two hexagons. The bonds are mostly sp^2-hybridized but, due to the curvature of the surface, acquire some sp^3 character [126]. The bond length is 1.4 Å for double bonds and 1.46 Å for single bonds, resulting in a diameter for the C_{60} molecule of 7.1 Å [127, 126].

The symmetry of C_{60}, the highest of fullerene molecules, is that of the icosahedral point group I_h, with 6 five-fold axes (C_5) that go through the center of the pentagons, 10 three-fold (C_3) axes normal to the hexagonal faces and 12 two-fold axes (C_2) that cross the double bond centers. The structure and symmetry of the C_{60} molecule is pictured in Figure 4.1.

4.2   Phase behavior

4.2.1   Orientational phase transition

At room temperature and pressures, the C_{60} molecules are in a face centered cubic (fcc) crystal phase (space group $Fm\bar{3}m$) in which each fullerene is rotating rapidly and almost freely about its center position in the lattice site [128, 126] . There is some local correlation between the orientations of neighboring molecules, which favors some pair configurations, but this phase remains mostly orientationally disordered [129]. The lattice parameter of the cubic cell at 300 K is 14.17 Å which gives a nearest-neighbor distance of 10.02 Å [126, 128].

It was first discovered by Heiney and coworkers [128] that, below a certain transition temperature ($T_0 = 260$ K at ambient pressures [130]), the C_{60} crystal solid undergoes a first order phase transition into an orientationally ordered phase with a simple cubic (sc) structure
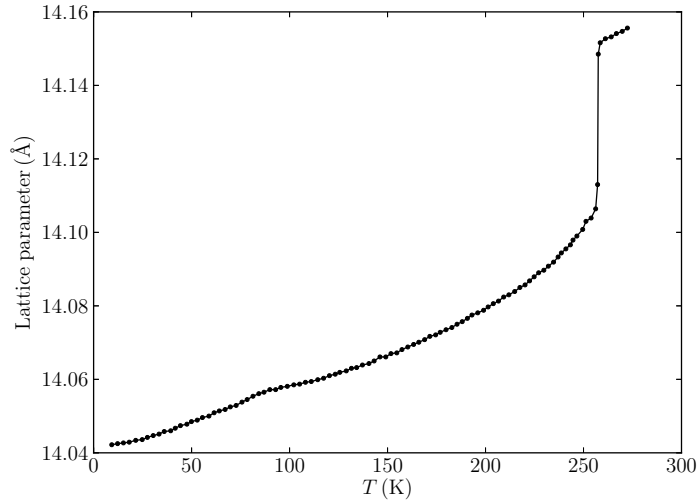
Figure 4.2: Experimental lattice parameter of the C_{60} fullerite cubic unit cell, as a function of temperature, with a sudden discontinuity at 260 K due to order-disorder transition and a small bump at 90 K due to the onset of the glassy phase. Data from David *et al.* [131].

(space group $Pa\bar{3}$). In this phase, rotation slows down abruptly and molecules are constrained to specific orientations with some small librational motion around the equilibrium. This transition is quite evident from the accompanying jump of 0.04 Å in the lattice parameter down to 14.10 Å (Figure 4.2). The lattice parameters then continues to decrease as the temperature drops, down to 14.04 Å around 10 K [130, 131, 128].

The driving mechanism for this transition is the orientational dependence of the intermolecular interactions between neighboring molecules that results from a non-uniform electron distribution in the molecular surface. In a C_{60} molecule the two types of bonds, single and double, have different lengths, as mentioned before. The double bonds, which are shorter, have a higher concentration of electrons than the single bonds, and will have a tendency to align with electron-poor regions of neighboring molecules, specifically, the pentagonal and hexagonal faces. These nearest neighbor configurations are commonly known as P (when a double bond of one molecule faces a pentagon on a neighbor) and H (double bond - hexagon) orientations.

In the freely rotating phase, some orientational correlation was already present, but the thermal energy was high enough that it remained local. Below the transition temperature, the intermolecular attraction outweighs the entropy gain by rotation and molecules begin to establish long range orientational order, as they align in one of the two preferred configurations mentioned above, minimizing the total energy of the crystal.

The following steps describe how to unambiguously achieve the orientation of the fullerene molecules in this ordered phase [126]:

- To begin, all molecules are positioned with its centers of mass at the sites of an fcc lattice.

- Secondly, each molecule is put at the same standard orientation, where its two-fold axes are aligned in all $\langle 100 \rangle$ directions. Two such orientations, obtained from each other by a 90° rotation, are possible. Throughout this work, standard orientation A, as defined in the book by Dresselhaus *et al.* [126] is used as the angle reference, although this choice is arbitrary.

- Then, each of the four molecules in the cubic unit cell, at positions $(0, 0, 0)$, $(\frac{1}{2}, \frac{1}{2}, 0)$, $(0, \frac{1}{2}, \frac{1}{2})$ and $(\frac{1}{2}, 0, \frac{1}{2})$ is assigned a *different* $\langle 111 \rangle$ local axis: $[111], [1\overline{1}\overline{1}], [\overline{1}1\overline{1}]$ and $[\overline{1}\overline{1}1]$, respectively [126]. These will be aligned with a molecular C_3 axis, which goes through the center of an hexagonal face.

- The four molecules of the unit cell are then rotated by a setting angle ϕ around their local assigned axis. A setting angle of $\phi_\mathrm{P} \approx 22°$ corresponds to the P configuration and $\phi_\mathrm{H} \approx 82°$ to the H configuration [130].[1]

The assignment of the local $\langle 111 \rangle$ axes causes the lowering of the symmetry, as the molecules are no longer equivalent by translation. The molecules are still positioned at the fcc lattice sites, but now form a simple cubic structure with four non-equivalent molecules per unit cell. The configuration with setting angles $\phi_\mathrm{P}(\phi_\mathrm{H})$ is such that six double bonds of a molecule are oriented towards six C$_{60}$ neighbors and six pentagons (hexagons) are facing the other six neighbors. The values of these angles were determined experimentally by analysing x-ray and/or neutron diffraction profiles [126, 131, 130, 132, 133].

The P and H orientations can be obtained from each other by a 60° rotation about the local $\langle 111 \rangle$ axis, or a 42° rotation about one of the C_2 axis normal to that direction. Molecules will rapidly alternate between both of these configurations while keeping a relative population of P/H configurations which is a function of temperature as well as pressure. Between 90 and about 200 K the ratio of molecules in the H and P configurations is well fitted by a Boltzmann distribution [131]. Let $f(T)$ be the fraction of molecules in the P configuration, then,

$$f(T) = \frac{1}{1 + \exp(-\Delta U / k_\mathrm{B} T)}, \tag{4.1}$$

where $\Delta U = U_\mathrm{H} - U_\mathrm{P}$ is the energy difference the two states. Fitting to experimental data at zero pressure gives an average value of $\Delta U = 11\,\mathrm{meV}$ [131, 134], with the P orientation being slightly less energetic and thus the majority orientation. Close to the fcc-sc transition temperature the fraction of P orientations is ~55% and, at 90 K, ~85%. The energy difference between orientations, ΔU in equation (4.1), is also a function of pressure and decreases with increasing P. For high enough pressures, the H orientation, which has slightly smaller molecular volume, is actually favored ($\Delta U < 0$), becoming the majority orientation [29].

---

[1]The actual values reported in [130] are $\phi_\mathrm{P} \approx 98°$ and $\phi_\mathrm{H} \approx 38°$, because standard orientation B was used as the reference. The resulting orientations are nevertheless equivalent.

Above a certain critical pressure, and for low enough temperatures, it is possible to obtain a phase with almost 100% population of H-oriented molecules [29, 135].

Below about 90 K, the system undergoes a continuous transition into a glassy state where the kinetic energy of the system is insufficient to overcome the relatively high rotational energy barrier between P and H configurations ($\sim 230 - 290$ meV [136, 137, 138, 139, 140]) and the hopping of the molecules between orientations is significantly reduced. Even as the temperature is decreased, the relative population of major and minor orientations remains frozen [130].

The fcc - sc transition temperature increases with increasing pressure, with the slope of the temperature-pressure curve being reported as around $\mathrm{d}T_0/\mathrm{d}P = 162$ K/GPa, a value arrived at by Sundqvist by combining various sources [29]. This observation has been historically difficult as it is highly dependent on experimental details. In particular, the use of different pressure transmitting gases is responsible for many inconsistent results, as lighter elements such as He are sometimes used and these are known to diffuse into the interstitial sites, reducing the compressibility of the fullerite [29].

4.2.2   Other features of the C$_{60}$ phase diagram

The C$_{60}$ fullerite sublimes at ~ 700 K, at normal pressures, without forming a liquid phase [29]. It is still an open question whether a stable liquid phase for this system is possible at all. Early theoretical investigations using an isotropic model for the C$_{60}$ molecule arrived at opposite conclusions regarding this problem [141, 142, 143]. Subsequent works proved that this result is sensitive to the characteristics of the potential model and other implementation details. Specifically, it was found that the appearance of a stable liquid phase depends on the range of the attractive tail of the C$_{60}$-C$_{60}$ interactions, which is very close to the limit where the triple point in the vapor-liquid-solid phase diagram crosses the critical point [144, 145]. Nevertheless, the various predictions point to a liquid phase that, if present, is only stable for a very narrow range of temperatures and pressures in the vicinity of 1900 K and 30 MPa [142, 146, 147, 117, 148, 68]. From an experimental point of view, it is difficult to provide a definitive answer on this question as well, since a very precise control of experimental conditions is required. At a nanoscale, MD studies have predicted that small clusters of seven fullerene molecules can achieve a liquid-like state [149, 150].

At high pressures, the C$_{60}$ fullerite exhibits a high variety of polymeric phases, ranging from small dimers or clusters to complex 3D structures. These polymeric phases have been extensively studied, both from an experimental and theoretical point of view. Detailed reviews on the subject are available in [151, 152].

Polymerization of the C$_{60}$ system can be achieved either through irradiation with intense UV or visible light (photopolymerization) or by submitting the sample to high pressures, which brings the molecules close together and promotes the creation of covalent bonds between

neighboring molecules. Photopolymerization was identified early in the study of fullerenes [153]. It allows for the formation of dimers or small clusters at low pressures and close to room temperatures. The process of formation of intermolecular bonds has been identified as 2+2 cycloaddition [152], wherein two double bonds, one from each molecule, open and form an intermolecular ring involving 4 carbons and 4 single bonds. One essential condition for this reaction is that the double bonds of adjacent molecules are brought together in parallel, which can only happen in the freely rotating phase ($T > 260$ K). Above 400 K, the thermal energy breaks the polymers and the C_{60} monomers are recuperated.

By comparison, with pressure induced polymerization one is able to obtain large, well ordered and stable 1D and 2D polymers [154, 155] and even complex 3D structures [156, 157, 158]. For pressures above 1 GPa and temperatures around $500 - 600$ K, dimers start to organize into large parallel chains along one of the $\langle 110 \rangle_c$ directions, where the c subscript refers to the parent cubic system. This causes a contraction of the cell in this direction, leading to an orthorhombic unit cell. For higher temperatures (T in $700 - 900$ K range) and pressures between 1.5 and $4 - 5$ GPa, parallel chains in a $\{100\}_c$ layer are brought together and cross-linked, forming a polymeric plane where where each molecule is connected to four others. This is the tetragonal polymeric 2D phase. For higher pressures, up to 9 GPa, the polymerization will happen on a $\{111\}_c$ plane of the parent lattice, resulting in a configuration where each molecule is connected to 6 neighbors. By submitting the pristine C_{60} sample or the 1D/2D polymerized fullerite to even higher pressures, $9 - 15$ GPa, and depending on the pressure-temperature treatment, it is possible to obtain a variety of different 3D polymers, some of which exhibit extreme elastic and hardness properties [157, 158].

4.3   Review of potential models

4.3.1   Atom-atom models

Each molecule in a fullerene solid is bound to others by weak van der Waals interactions. The intramolecular carbon-carbon covalent bonds are, comparatively, much stronger [126]. For this reason, the structural properties of the crystal are much more sensitive to changes in pressure and temperature than the shapes of the molecules themselves. This is no longer true for conditions of extreme pressure or temperature, when polymerized phases are formed, or the molecules are otherwise subjected to intense forces leading to their deformation or destruction. For normal conditions, up to a few GPa and less than 700 K, the rigid molecule approximation is usually used and internal forces are disregarded.

One of the first models used to describe interactions between C_{60} molecules was proposed by Cheng and Klein (CK) [159, 160]. It takes an atomistic approach, that is, it explicitly considers each of the 60 atoms in a molecule as an interaction center, and derives the total energy between two molecules as a sum over all pairs of carbon atoms in different molecules,

$$U^{\text{CK}} = \sum_{i=1}^{60} \sum_{j=i}^{60} u_{\text{C-C}}\left(r_{ij}\right), \tag{4.2}$$

where r_{ij} is the distance between the i-th atom on the first molecule and the j-th atom on the second molecule and $u_{\text{C-C}}$ is the atom-atom pair term. The 12-6 Lennard-Jones potential, equation (2.60), was chosen for this term, and its parameters were taken from the well known interactions between carbons in different layers of graphite.

4.3.2   Bond charge models

It was discovered early that the simple atomistic model of equation (4.2), where the interaction sites are located in the positions of the 60 carbon atoms, is not enough to actually stabilize the $Pa\bar{3}$ simple cubic phase at low temperatures, instead predicting an orthorhombic [161] or tetragonal [160] structure. Sprik, Cheng and Klein (SCK) [162] found that incorporating additional Lennard-Jones interaction sites at the center of the double bonds is enough to stabilize the cubic structure and thus reproduce the fcc-sc phase transition, albeit at much lower transition temperatures than expected. The effect of the additional site is subtle but essential. In the simple model with only atom-atom LJ interactions, the tetragonal phase was characterized by double bonds in neighboring molecules being brought together, in crossed configuration. The extra interaction site adds a short-range repulsion which penalizes this near-neighbor orientation. The LJ parameters must be adjusted to account for the extra sites.

In the same work [162], the authors enhanced their model further and found a better fit to the fcc-sc transition temperature when partial negative charges are added to the same double bond sites and neutralizing charges to all carbon sites. This is an attempt to model the anisotropy of the charge distribution on the molecular surface mentioned in §4.2.1, which causes the electron-rich double bonds to align with electron poor pentagonal and hexagonal faces. The authors found, from MD simulations, a transition temperature of $T_{\text{c}} \approx 215$ K, signaled by an abrupt change in the unit cell size and energy of the system. This value is still far from the experimentally observed $T_{\text{c}} = 260$ K. More recently, Chang and Sandler [163] carried out precise free energy calculations of the phase transition for the second SCK model and found a transition temperature of $T_{\text{c}} = 257$ K using slightly modified parameters.

Other simple models based on the same principles have been proposed. Lu, Li and Martin (LLM) [164] chose to keep the 60 LJ sites at the carbon atoms and move the partial charges to the centers of both the double and the single bonds. From mean field arguments the transition temperature was estimated as $T_{\text{c}} \approx 271$ K, but this was not confirmed by MC or MD simulations. Burgos, Halac and Bonadeo [165] changed the van der Waals carbon-carbon potential to the Buckingham form,

$$u_{\text{C-C}}\left(r\right) = Ae^{-Br} - Cr^{-6}, \tag{4.3}$$

and moved the positive partial charges to the centers of the pentagonal faces while keeping
the negative charges at the centers of the double bonds. Pintschovius and Chaplot [166] opted
for a charge distribution where positive charges are placed in the double bond centers but
split in two radial directions, a fraction going inside the molecule and the other outwards.
Lamoen and Michel [167] put interactions centers at the atomic positions, single bond centers
and in 3 locations along each double bond, in order to better account for the distribution of
$\pi-$electrons.

Kita *et al*, [168] took a more elaborate approach than the previous attempts by making the
van der Waals term explicitly anisotropic, i.e., the interaction between two atoms is a function
of both the distance between the atoms and the relative orientation of the two molecules.
Additionally, the electrostatic interactions are due to permanent dipoles positioned on the
atom sites and parallel to the double bonds. With proper parametrization this model is
able to reproduce an activation barrier between the P and H orientations of 260 meV and an
energy difference of 14 meV, in good agreement with experiments. On the other hand, the
orientational phase transition is accompanied by a smooth change in the lattice parameter
and the rotational order parameters in a range from 200 to 260 K. Experimentally, this change
is much more abrupt.

The models presented here, despite their various degrees of complexity and accuracy,
are still ad-hoc models, based on specific experimental phenomena that they try to repro-
duce, and are, thus, fundamentally limited. Savin *et al.* [169], argued that these so-called
bond charge models do not properly describe Coulomb interactions between fullerenes, and
proposed a semi-empirical potential where the Coulomb charges are treated microscopically
using a charge distribution estimated by density functional theory (DFT) with the local den-
sity approximation. Additionally, short range interactions were modeled with several LJ sites
distributed over the surface of the molecules. This model leads to a surprising conclusion
regarding the nature of the orientational correlation between molecules: the authors argue
against the commonly held view that Coulomb interactions are minimized when a double
bond of one molecule faces a pentagon or hexagon of another (DB-P/H alignment) and that
they are, in fact, maximized. This model actually favors a nearest neighbor configuration
with atom-pentagon alignment, but, in a crystal, it is impossible to optimize all interactions
in this way, and so long range ordering based on DB-P/H aligned nearest neighbors emerges,
as expected from experimental observations.

Full scale *ab initio* calculations of the C_{60} solid have been performed [170, 171, 172], but
these kinds of studies are also limited in scope of applicability, both due to the difficulty in
accounting for long range interactions using DFT and the computational effort required to
perform these calculations.

The simple phenomenological models that attempt to balance a basic empirical description
of the molecule and an accurate portrayal of the forces involved still have an important role
to play in the study of the properties of bulk fullerite. They are able to describe important

properties of the phase diagram of these systems while maintaining a complexity that is accessible to MC or MD simulations of relatively large systems, which is important when studying the phase behavior.

4.3.3 Central body

The atomistic/bond-charge models can be greatly simplified if one is only interested in the properties of the freely rotating solid or gas phases. In these conditions, a molecule can be treated as a spherical surface with a uniform density of carbon atoms. The well known potential model of Girifalco [173] is constructed in this manner. Equation (2.60) is uniformly integrated along a spherical shell with a diameter $d = 7.1\,\text{Å}$ and a functional form is derived for the interaction between two C_{60} molecules that only takes into account the distance r between their centers:

$$U^G(r) = -\alpha \left[\frac{1}{s(s-1)^3} + \frac{1}{s(s+1)^3} - \frac{2}{s^4} \right] + \beta \left[\frac{1}{s(s-1)^9} + \frac{1}{s(s+1)^9} - \frac{2}{s^{10}} \right], \quad (4.4)$$

where $s = r/d$, and α and β are constants related the density of atoms in the surface and the carbon-carbon Lennard-Jones parameters,

$$\alpha = \epsilon \frac{N^2}{3} \left(\frac{\sigma}{d} \right)^6, \quad (4.5)$$

$$\beta = \epsilon \frac{2N^2}{45} \left(\frac{\sigma}{d} \right)^{12}, \quad (4.6)$$

where $N = 60$ is the number of atoms in the molecule. $\sigma = 3.469\,\text{Å}$ and $\epsilon = 33.25\,\text{K}$ are the free LJ parameters that were adjusted to reproduce the lattice constant and heat of sublimation [173].

This model, despite its simplicity, is very useful to describe the high temperature behavior of the C_{60} system and has been used extensively to predict the phase diagram in this regime [141, 142, 147, 148]. Because it does not contain any orientational dependence it cannot reproduce the transition into the low temperature orientationally ordered phase.

Another central body potential was derived by Pachecho and Prates Ramalho [170] from *ab initio* calculations which is softer than the Girifalco potential at shorter distances and also includes a three body term. Ferreira *et al.* [117] and Barroso [68] studied the high temperature phase diagram of C_{60} using this potential and found that it predicts a liquid phase. Furthermore, it was found that the three body dispersive term has a stabilizing effect on the liquid phase, increasing the temperature range where it can be found [68].

Table 4.1: Parameters and interaction sites for the potential models used in this work. C corresponds to an atom site, SB and DB to the center of the single and double bonds, respectively. e is the charge of the electron.

Model	Site	Lennard-Jones		Coulomb	Refs
		$\epsilon\,(\mathrm{K})$	$\sigma\,\left(\mathrm{\AA}\right)$	$q\,(|\mathrm{e}|)$	
CK	C	28	3.4		[159, 160]
SCK	C	14.8	3.4	0.225	[162, 163]
	DB	14.8	3.6	-0.45	
LLM	C	34.4	3.4		[164]
	SB			0.27	
	DB			-0.54	

4.4   Simulations of the orientational phase transition of C_{60}

4.4.1   Potential details

For the purposes of investigating the orientational phase transition on the C_{60} fullerite, the models of Cheng and Klein (CK) [159, 160]; Sprik, Cheng and Klein (SCK) [162] with modifications to potential parameters by Chang and Sandler [163]; and Lu, Li and Martin (LLM) [164], described in §4.3, were used. A summary of the potential terms and parameters of each model is given in Table 4.1. The cross LJ parameters between interaction centers of type i and j, are given by the Lorentz-Berthelot mixing rules,

$$\epsilon_{ij} = \sqrt{\epsilon_i \epsilon_j} \quad \text{and} \quad \sigma_{ij} = \frac{\sigma_i + \sigma_j}{2}. \tag{4.7}$$

To reduce the computational effort required to evaluate the potential energy of a system of N molecules with 60, 90 or 150 distinct sites each, the atomistic and bond charge interactions between a pair of molecules were restricted to maximum center of mass distance of $r_{\mathrm{CM}}^c = 12\,\mathrm{\AA}$. In the pressure and temperature range investigated in this work, the centers of mass of the C_{60} are located around the sites of an fcc lattice of side $\sim 14\,\mathrm{\AA}$. This cutoff distance limits the full interaction to the first molecular neighbors only. For molecules that are separated by more than r_{CM}^c the central body approximation of Girifalco, equation (4.4), is used, which only takes into account the distances between molecular centers. This approximates the van der Waals interactions effectively at medium to long range distances, at which point the detailed atomistic model is unlikely to be necessary, and has the advantage of being orders of magnitude faster. Coulomb interactions are not considered for distances larger than r_{CM}^c. As discussed in §2.3.2, it is usually not safe to apply short-range truncation to electrostatic interactions, and special numerical techniques such as the Ewald summation are usually necessary. However, as is demonstrated in Figure 4.3(b), the magnitude of the total Coulomb energy between a pair of neutral C_{60} molecules drops approximately with r_{CM}^{-13}, where r_{CM} is the intermolecular distance, which is sufficiently fast to be handled by this truncation scheme, according to the
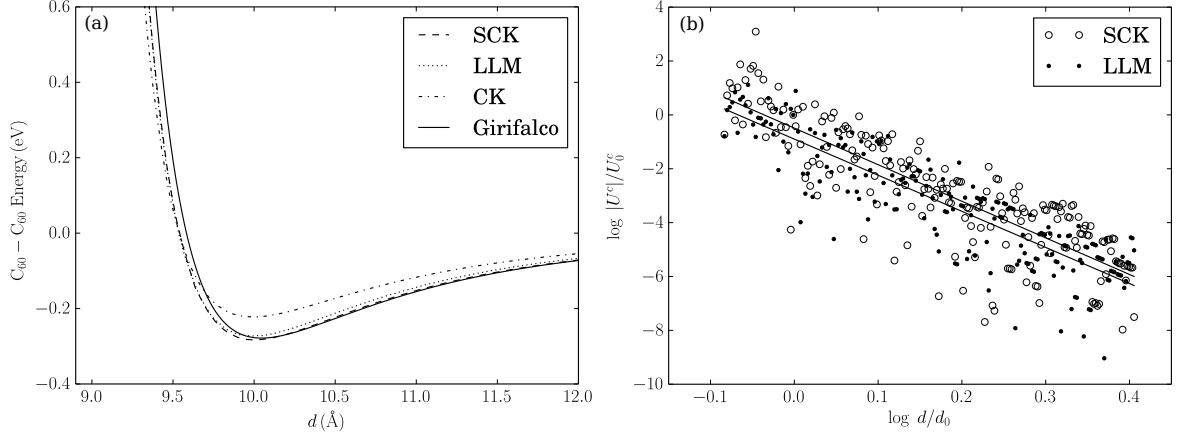
Figure 4.3: Energy of two C$_{60}$ molecules as a function of intermolecular distance d for the potential models used in this work, obtained by averaging over 10000 random orientations of the molecules: (a) total energy; (b) Coulomb term only, on a log scale. The solid lines in subfigure (b) are linear fits to the data whose slopes are -13.6 and -13.4, for the SCK and LLM models, respectively.

criteria defined in §2.3.2.

The dependence of the total potential energy, including van der Waals and Coulomb interactions, on the distance between a pair of C$_{60}$ molecules is given in Figure 4.3(a), averaged over all orientations, for the models considered in this work. Depending on the relative orientation of the molecules, the energy minimum may be shifted a few hundredths of an Angstrom. The CK model, due to a conservative choice of $\epsilon = 28\,\mathrm{K}$, has a noticeably shallow attractive well and a less repulsive core. The SCK and LLM potentials are very similar, and are well approximated by the Girifalco effective potential, except for a small difference on the location of the energy minimum that results from changes in the chosen parameters.

For the purposes of studying the properties of the ordered and disordered phases, these details are less important than the dependence of the total energy on the relative orientation of the fullerenes. In Figure 4.4, the energy of a molecule in a unit cell of fullerite is given as it is rotated by an angle ϕ around the local $\langle 111 \rangle$ rotation axis set by the symmetry. Three cases are explored: (i) coherent rotation of all molecules by the same angle around its own $\langle 111 \rangle$ axis, as described in §4.2.1; (ii) rotation of one molecule with its neighbors fixed at the P position ($\phi \approx 22°$); (iii) rotation of one molecule with its neighbors fixed at the H orientation (the exact angle varies). All curves were obtained using a lattice constant of $a = 14.04\,\text{Å}$, but the shape of these curves is relatively insensitive to this value. As can be seen by following the solid curves in Figure 4.4, all three models correctly exhibit an energy minimum when all molecules are at $\phi \approx 22°$, corresponding to a configuration where all molecules are in an P orientation (all-P), that is, DB-Pentagon alignment between near neighbors. For the CK model, however, this is a local minimum, instead of a global one. An all-H configuration, where every molecule is DB-Hexagon aligned with its neighbors, should happen when they
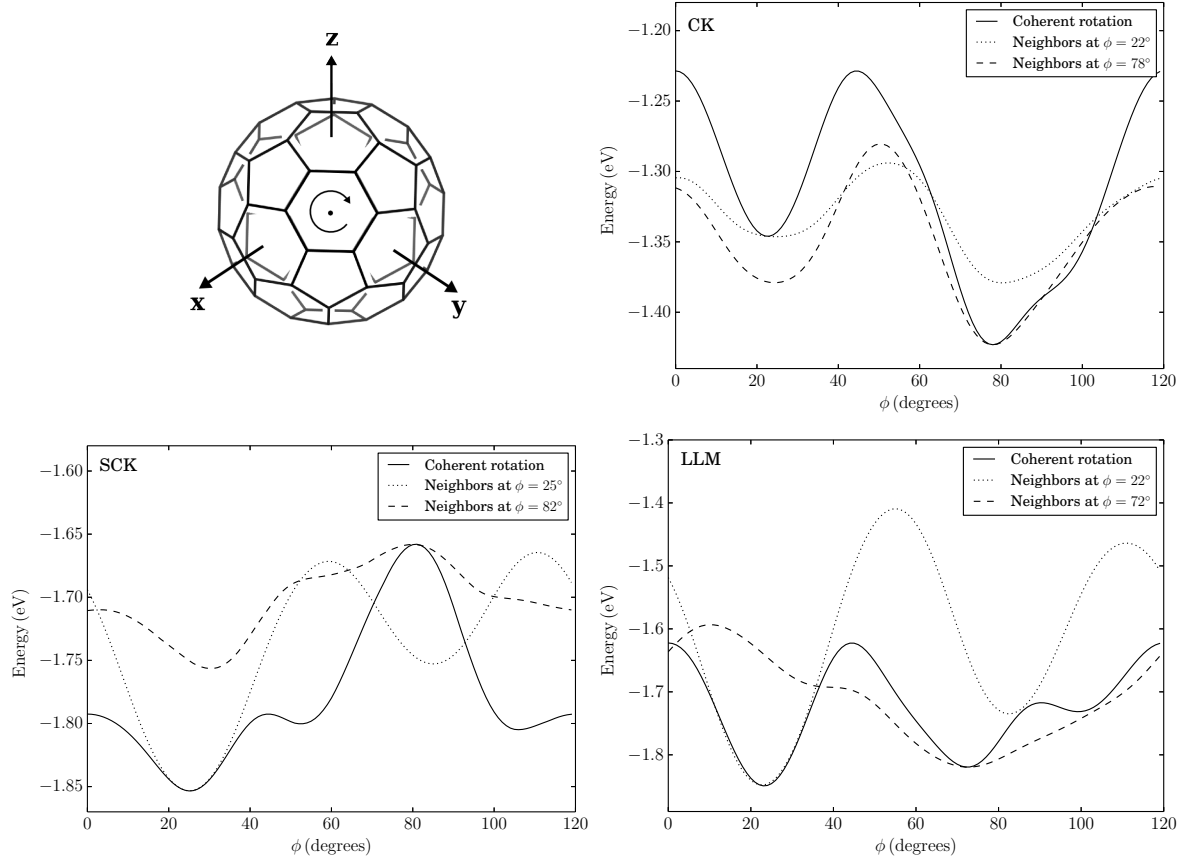
Figure 4.4: Dependence of the intermolecular potential on the orientation of one molecule with respect to its neighbors. The rotation by angle ϕ is measured around a local $\langle 111 \rangle$ axis which is different for each molecule of the unit cell, as described in §4.2.1. For the molecule at position $(0, 0, 0)$, the axis of rotation is [111]. The diagram on the top left shows the P orientation of this molecule ($\phi = 22°$) and the rotation axis. When the rotation is coherent, all molecules rotate by the same angle ϕ. Otherwise, the molecule at $(0, 0, 0)$ will rotate while its neighbors are fixed at some other setting angle.

all have a setting angle close to $82°$. For the LLM model, this minimum happens at $\phi = 72°$. Surprisingly, such a configuration is energetically unfavorable on the SCK model, as can be seen by the maximum of the solid curve at this angle.

The dotted lines show the effect of the orientation of one molecule when the remainder of the system is in a P orientation. In this situation, for the SCK and LLM models, the energy will be minimized when the molecule is also at a P configuration, but there is another minimum for an H orientation, at $\phi = 82°$, which the molecule can reach after crossing a significant energy barrier. Quantitatively, at $a = 14.04\,\text{Å}$, the height of this energy barrier is $180\,\text{meV}$ and $380\,\text{meV}$, for the SCK and LLM models, respectively. This compares with the experimental value of $\sim 230 - 290\,\text{meV}$ [136, 137, 138, 139, 140]. The energy difference between the two states, at the bottom of the wells, is $100\,\text{meV}$ and $110\,\text{meV}$, respectively, which is much larger than the experimental value of $11\,\text{meV}$ [131, 134].

The dashed lines in Figure 4.4 show the favorable states for a molecule immersed in all-H

orientation	$m = 0$	$m = 1$	$m = 2$	$m = 3$	$m = 4$	$m = 5$	$m = 6$
P ($\phi = 22°$)	-0.3659 $0i$	± 0.5958 $\pm 0.5897i$	0.0221 $\pm 0.5927i$	± 0.7027 $\pm 0.7124i$	0.6846 $\pm 0.0071i$	± 0.3926 $\pm 0.3843i$	-0.0149 $\pm 0.8072i$
H ($\phi = 82°$)	0.4385 $0i$	± 0.7035 $\pm 0.7177i$	-0.006 $\pm 0.7105i$	0.0879 $\pm 0.1104i$	-0.8203 $\pm 0.0164i$	± 0.6502 $\pm 0.6309i$	0.040 $\pm 0.6483i$
H ($\phi = 72°$)	0.2494 $0i$	± 0.4191 $\pm 0.9421i$	-0.2898 $\pm 0.5080i$	0.4335 $\pm 0.3934i$	-0.4666 $\pm 0.6039i$	± 0.8333 $\pm 0.1252i$	0.1954 $\pm 0.6597i$

Table 4.2: Reference values for the Q_{6m} parameters of a C_{60} molecule in the P and H orientations. Values with the $\pm$ symbol may be positive or negative, depending on which of the four $\langle 111 \rangle$ rotation axes is set.

configuration. For the SCK model, such a state is highly unstable. For the LLM model, the tendency of the free molecule will be to align with its neighbors orientation. This shows that this model should be able to predict an all-H configuration.

4.4.2 Simulation details and order parameters

Monte Carlo simulations were carried in the NPT ensemble using the anisotropic volume update, described in §2.2.5. 108 C_{60} molecules were initially positioned at the face centered cubic lattice sites. When anisotropic volume updates are used, the lengths and angles of the unit cell, initially cubic, may change during the course of a simulation. The standard molecular displacement, molecular rotation and volume update moves were used, as described in §2.4. Since the molecules were considered rigid, no moves were implemented to sample the internal degrees of freedom.

Simulations were performed for pressures of 0, 300, 500, 700, 1000 and 1300 MPa, and a variable temperature range. Simulations were initiated in an all-P configuration with $\phi = 22°$, unless otherwise stated. For each Monte Carlo step, on average, N molecular displacements, N molecular rotations and 1-5 volume update moves were performed. Each simulation was carried out for 5×10^4 MCS, with a sample being recorded every 20 steps. About 30% of the initial samples were required for the equilibration stage, and were discarded from the analysis.

To describe the orientational ordering of the molecules in the solid phase, the order parameter of reference [160] was used, $Q_{6m} = \sum Y_{6m}$, where Y_{6m} is the spherical harmonic function of sixth order, with $m = 0, 1, ..., 6$, and the sum is over all the 60 carbon atoms of the molecule. Since Q_{6m} is a complex number for $m > 0$, there are 13 parameters which can be used to identify the absolute orientation of a molecule, but they are not all independent. The values of Q_{6m} for the P and H orientations are given in Table 4.2. The $\pm$ symbol means that a particular component of Q_{6m} takes alternating positive and negative signs for each of the four non-equivalent molecules in the unit cell (two times each). Thus, the average of Q_{6m} over all the molecules in a perfectly P or H aligned unit cell (or a sample with multiple cells) is zero except for the real component of Q_{60}, Q_{62}, Q_{64} and Q_{66}. If the molecules are rapidly
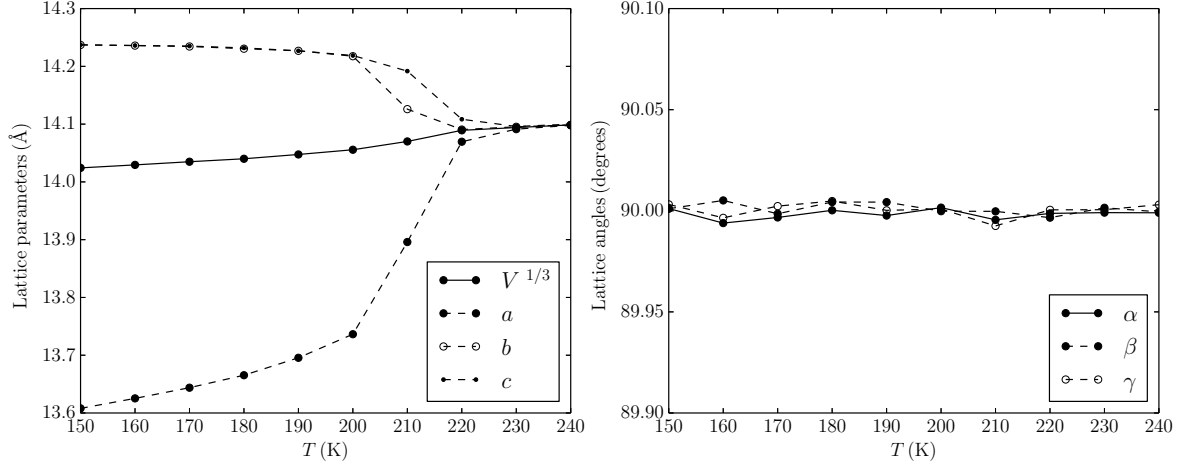
Figure 4.5: Change in volume V and shape of the simulation cell for the CK model at $P = 0$. a, b and c are the lengths of the lattice vectors and α, β and γ the angles between them. At low temperatures, the cubic lattice is stretched in two directions and shortened on the other.

rotating, with little restriction on the orientation they may take, all components of Q_{6m} will be spread in between approximately -1.5 and 1.5 with a bias towards the origin. Thus, in the high temperature phase, the ensemble and sample average of Q_{6m} drops to values close to zero.

The distribution of angles ϕ is also measured. Examples are shown on the diagrams of Figure 4.7(b,d,f). For each molecule, ϕ is defined as the angle of rotation around the $\langle 111 \rangle$ axis that passes through the molecular center of mass which is most aligned with a C_3 molecular axis. If no C_3 axis can be found at less than an $8°$ angle with one of the four $\langle 111 \rangle$ axes, then this molecule is considered misaligned, and does not contribute to the ϕ histograms. The distribution $p(\phi)$ represents the probability of finding a molecule which is aligned with a $\langle 111 \rangle$ axis and has angle of rotation ϕ. Thus, the integral $\int p(\phi) \, d\phi$ gives the fraction of molecules which are aligned, according to this criterion. This is why the area under the high temperature curves of Figure 4.7(b,d,f) is smaller, since in these disordered states, fewer molecules will have the proper alignment.

The gray shaded area in those figures represents the curve obtained by this procedure considering a uniform distributions of orientations.

4.4.3   Results

Low pressures

In Figure 4.5, results for the average unit cell dimensions and shape are presented for the CK model at $P = 0$ as a function of temperature. Below $220\,\mathrm{K}$, the lattice undergoes a transformation and the cubic symmetry is lost, with one side of the unit cell decreasing by about 2% while the other two dimensions increase by 1%. The angles of the cell remain
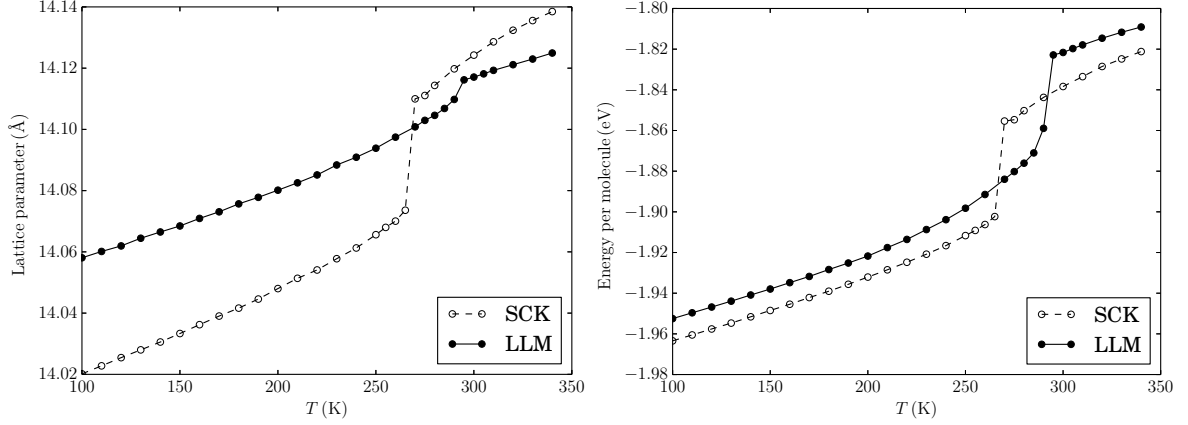
Figure 4.6: Variation of the cubic lattice parameter and energy with temperature at $P = 0$, for the bond charge models. There is a sudden drop in both quantities due to the transition to the orientationally ordered phase at 270 K and 295 K.

at $90°$. As expected, the CK model with only LJ interaction sites at the 60 carbon atoms predicts a tetragonal phase at low T. This confirms the results obtained by the early MD simulations of Cheng and Klein with 32 molecules [159, 160], and serves as a test case for the anisotropic NPT MC algorithm used in the work of this chapter. While the Q_{6m} order parameters exhibits a change at $T = 220$ K, indicating the onset of some orientational order, an analysis of the orientational profile of the samples indicates that the molecules have no tendency to align any of its C_3 axes with a local $\langle 111 \rangle$ axis, and thus no P or H configurations can be identified. This model does not reproduce the real sc-fcc transition of the C_{60} fullerite.

In Figure 4.6, NPT simulation results are presented for the SCK and LLM models at zero pressure. During the course of these, and subsequent, simulations no significant deviations from a cubic unit cell were observed, and, as such, only one lattice parameter is reported. It is clear from the plots of Figure 4.6 that the system undergoes a first order phase transition, in both models, as evidenced by the abrupt change in the lattice parameter and the potential energy of the system. The transition temperatures at $P = 0$ are estimated as $T_0 = 270$ K and 295 K, for the SCK and LLM models, respectively. When compared with the experimental result of $T_0 = 260$ K, and the plot of Figure 4.2, the SCK model predicts a better estimate of both the transition temperature and the accompanying change in the lattice parameter. Both models underestimate the lattice parameter, which is 14.17 Å at room temperatures.

In Figure 4.7, the orientational profile of this transition is given in terms of the Q_{6m} parameters and the distribution of the angles ϕ around the principal rotation axis of a molecule. From those images, the order-disorder transition is evident due to the abrupt change in Q_{6m} at T_0 and the difference in the distribution of ϕ above and below this temperature. The following discussion will focus on the first two rows of Figure 4.7, leaving the last one to be analyzed in the next section.
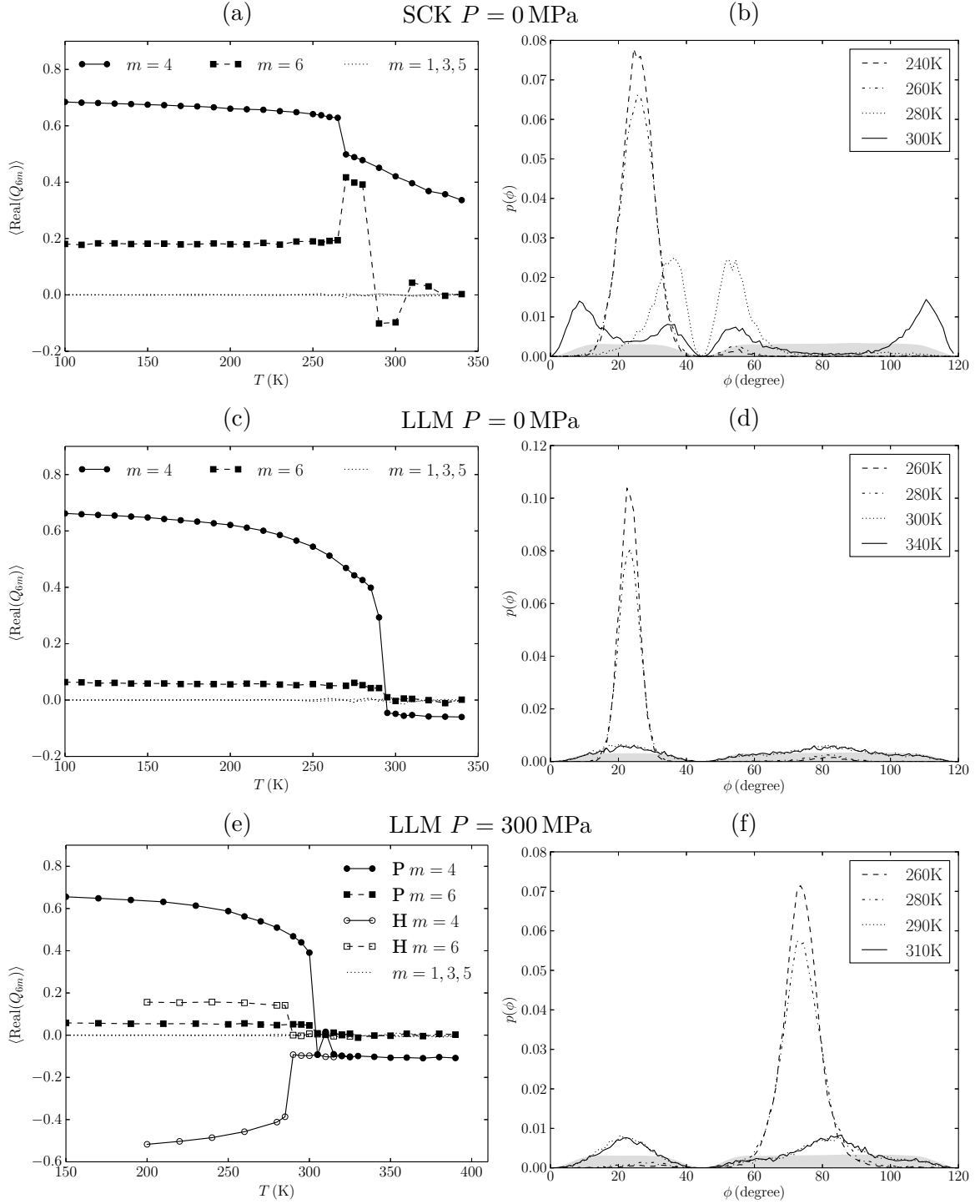
Figure 4.7: Orientational order parameters Q_{6m}, averaged over all molecules and samples, as a function of temperature (a,c,e) and distribution of the angle of rotation ϕ around a local $\langle 111 \rangle$ crystal axis observed in some simulations (b,c,f). The shaded gray areas on the right all represent the curve ϕ which would be obtained if all orientations were truly uniformly distributed. Subfigure (e) shows the transition to both the majority P and majority H states, and the distributions represented in subfigure (f) are for the majority H and random states.

For the SCK model, the average of the real component of Q_{64} approaches 0.6846, the value expected of an all-P configuration (cf. Table 4.2), as the temperature is decreased below T_0. For $m = 6$, the value is close to zero, but not negative, indicating that this low temperature phase does not strictly equate with $\phi = 22°$. Indeed, it is visible from Figure 4.4 that the global P minimum is closer to $\phi = 25°$ for this model, and the theoretical value of Q_{66} at this angle is $0.17 \pm 0.79i$, which is much closer to the observed. This is further established by the distribution of angles observed at $T = 240\,\text{K}$ and $260\,\text{K}$, which have a very large peak with mean values $25.6\,(1)°$ and $25.7(1)°$, respectively. At these temperatures, a vanishingly small number of molecules are found at angles close to $82°$, in the H minority configuration. Instead a secondary peak appears near $55°$. Since the majority configuration is P, this rotation angle should be energetically unfavorable (cf. Figure 4.4). The reasons for this peak are unclear, but it suggests a more complicated orientational dependence than is captured by the discussion so far, which focuses on a one-dimensional analysis of the rotation angle around a $\langle 111 \rangle$ axis.

When $T > T_0$, the SCK model predicts a phase whose orientations are not completely random. First, the parameters Q_{6m} should drop very fast to values near zero in these conditions, which does not happen for $m = 4$ and, for $m = 6$, only after passing two stages. This is further confirmed from the angle distribution at these temperatures, which also suggests two high temperature regimes, as the curves for $280\,\text{K}$ and $300\,\text{K}$, both above T_0, are markedly different. This two-stage behavior is recurrent for higher pressure simulations of the SCK model.

In contrast to the above discussion, the LLM model shows the expected behavior for both the Q_{6m} parameters and the ϕ distribution. Q_{64} is close the theoretical value for an all-P configuration at the lowest temperatures. As it approaches T_0 it gradually decreases due to the mixing of molecules with different orientations and, at the transition temperature, it drops abruptly to values near zero. The angle distribution shows a pronounced peak with mean value $23.2\,(1)°$ for both $T = 260\,\text{K}$ and $T = 280\,\text{K}$, corresponding to the P configuration of the majority of the molecules, and a smaller one at $82°$, which signifies the presence of a limited number of molecules with H orientation. This very small minority H population is in contrast with the experimental evidence, which points to about 15% of H-oriented molecules, even at $90\,\text{K}$, and close to 50% at the transition temperature [131, 134]. That such is not observed with this, and the SCK, model is a consequence of the high energy gap between the P and H orientations, mentioned in §4.3, which is $110\,\text{meV}$, 10 times larger than the experimental value. Substituting in equation (4.1), the estimated fraction of H oriented molecules close to T_0 for this potential is about 1%. The observed amount in the simulations is about 5%, but it is not clear what part of this figure results from rapid reorientation between P and H orientations, or is simply due to the onset of the disordered phase.

For $T > T_0$, the distribution of the ϕ angles is suddenly flattened, as can be seen in Figure 4.7(d), and are very close to the uniform distribution curves represented by the shaded area. The valleys at angles $0°$ and $43°$ are a consequence of the procedure used to determine
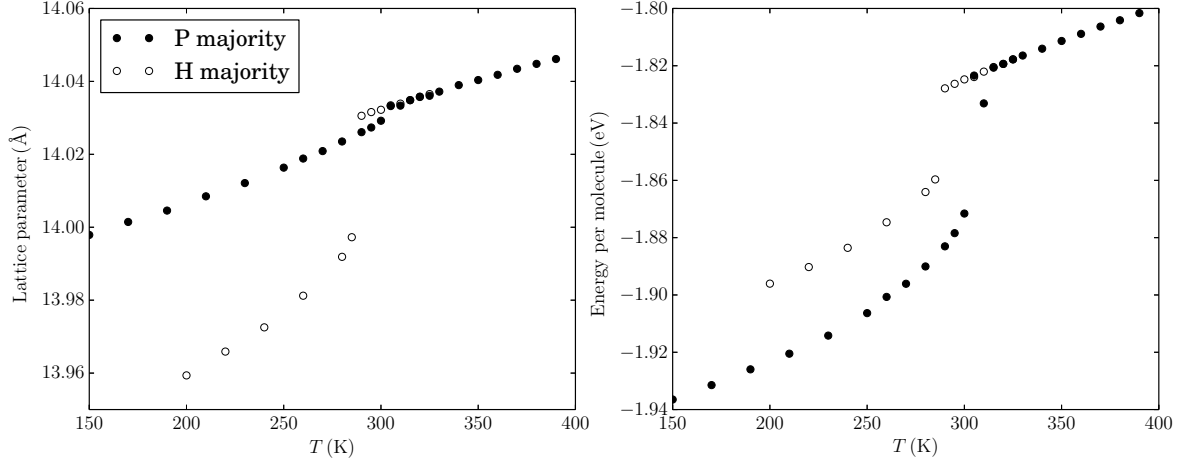
Figure 4.8: Orientational transition for the LLM model at 300 MPa for two low temperature phases, where the populations are either mostly P or mostly H oriented.

ϕ, as discussed in §4.4.2. The Q_{6m} parameters also take values compatible with a highly disordered phase.

High pressures

The properties of the sc-fcc transition for the SCK model remain fundamentally unchanged with increasing pressure. A linear increase in the transition temperature can be observed (Figure 4.9), as well as the natural reduction in lattice parameters and increase in energy, as the molecules are brought closer together. The calculated value of $\mathrm{d}T_0/\mathrm{d}P$ is $0.137 \pm 0.010\,\mathrm{K/MPa}$, which compares with the experimental value of $0.162\,\mathrm{K/MPa}$, mentioned in §4.2.1.

Experimentally, it is observed that, for sufficiently high pressures, the H orientation becomes more stable and the majority of the molecules would be found with setting angles near 82° [29]. For the SCK model, however, such a phase does not seem possible since an all-H unit cell corresponds to an energy maximum (cf. the line corresponding to a coherent rotation for the SCK model in Figure 4.4). This was confirmed by initiating several simulations below T_0 with an all-H configuration, for all pressures, and observing that they quickly relax into all-P states.

For the LLM model, the H majority state is at an energy minimum, and may occur if the pressure is high enough. To investigate this possibility, simulations were initiated in all-H configurations. At zero pressure, it was found that this state is thermodynamically unstable, as simulations converge to all-P configurations below T_0, reproducing the results shown in figures 4.6 and 4.7(c,d). At 300 MPa, the results show that both the P and H majority states are locally stable below T_0, with high transition times between them, since a simulation initiated in one does not evolve into the other during the length of the run. In both cases,
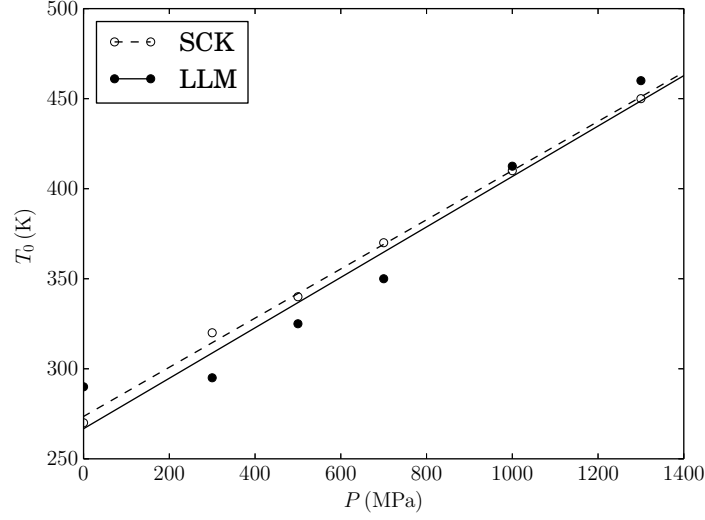
Figure 4.9: Variation of the transition temperature with pressure. For the highest pressures, the uncertainty in the visual identification of T_0 may be as high as $30\,\mathrm{K}$. The equations for the linear fits to the data are $T_0 = (0.137 \pm 0.010)\,P + 273 \pm 7$ and $T_0 = (0.14 \pm 0.05)\,P + 267 \pm 30$, for SCK and LLM, respectively.

the transition into a disordered fcc phase with increasing temperature is reproduced, but at slightly different values of T_0, $305\,\mathrm{K}$ (P) and $290\,\mathrm{K}$ (H). The corresponding lattice parameter and energy variation with temperature is given in Figure 4.8. It is clear from this figure, that the energy of the H majority phase is higher and its lattice constant much smaller. This reflects the fact that, for the LLM interaction model, the potential energy minimum between two H oriented molecules is higher and happens for a smaller C_{60}-C_{60} distances, than if they were P aligned. The values of the orientational order parameters, given in Figure 4.7(e), for the H majority phase are compatible with a setting angle of $\phi = 72°$, and the distribution of sampled angles represented in Figure 4.7(f) supports this observation. The move from a P to an H majority population changes the relaxation angle of the H orientation from $82°$ to $72°$ degrees.

At $P = 500\,\mathrm{MPa}$, simulation results show that the P majority phase is less stable, as some spontaneous transformation from P to H majority near T_0 is observed, but not the reverse. For $P \geq 700\,\mathrm{MPa}$, most simulations in the sc phase reach a final H majority configuration, but this often requires long equilibration times, and the sampling statistics are poor.

The estimated $\mathrm{d}T_0/\mathrm{d}P$ for the LLM model obtained in this work is $0.14 \pm 0.05\,\mathrm{K/MPa}$, in line with the result for the SCK case.

4.5 Conclusions

In this chapter, the rotational phase transition of the fullerene C_{60} was studied by means of NPT MC simulations using models of the molecule which treat each atom and bond

as a possible interaction point. The transition is easily identified by the sudden drop in the lattice parameter, energy and the rotational order parameters, which happens when the temperature drops below a critical value. Some hysteresis is present, however, which makes the visual criteria used here somewhat imprecise.

The CK model, which treats the molecule as rigid assembly of 60 Lennard-Jones sites at the atomic positions, predicts a low temperature tetragonal phase that, while indicating some orientational order, is against experimental evidence.

In the SCK model, which includes electrostatic interactions due to partial charges in the atom sites and the centers of the double bonds, a stable low temperature simple cubic phase is correctly found, with a transition temperature of $270\,\mathrm{K}$ at zero pressure, close to the experimental value of $260\,\mathrm{K}$. Furthermore, this phase is characterized by a nearly 100% occupation of P oriented molecules, with setting angles $\phi = 25°$ around the local $\langle 111 \rangle$ axes. This compares with the approximated experimental value of $22°$. No H minority population can be found with statistical certainty. For this model, the H majority state is energetically prohibited. For temperatures above T_0, a non-uniform distribution of molecular orientations and a larger than expected Q_{64} parameter is found, indicating that the high temperature phase is not truly rotationally free.

The LLM model, which considers partial charges in both the single and double bond centers, also predicts the fully P aligned phase at low temperatures, but for temperatures close to T_0, there is a gradual mixing of other orientations, including a small population of H oriented molecules. If the pressure is high enough, the H majority orientation becomes more stable. Spontaneous transformation to an H majority orientation is observed for pressures $P \gtrsim 500\,\mathrm{MPa}$. Due to the hysteresis and long ergodic times associated with this transformation, only a careful treatment based on free energy calculations can help determine the exact conditions for the stability of the H and P majority phases. The observed P (H) majority $\langle 111 \rangle$ rotation angle is $22°$ $(72°)$. The LLM model also correctly predicts a freely rotating high temperature phase, with little orientational bias, even for temperatures immediately above T_0.

The LLM model is the best performer of the set in terms of describing the orientational properties below and above T_0. Its major downfall is the fact that it does not allow for the coexistence of P and H populations in the proper ratio, due to a very large difference between the energy levels of the two states, an order of magnitude higher than expected.

Chapter 5

Hydrogen Adsorption in Zeolites

5.1 Introduction

Hydrogen is expected to play an important role in a future energy economy based on environmentally clean sources and carriers. As a fuel, it has tremendous potential. It is the most abundant element in the universe, lightweight, has the highest energy density by weight of any common fuel (although less so by volume), and it can be used to generate energy with no harmful by-product and high efficiency [33]. However, its adoption as the primary energy carrier faces substantial challenges [174]. Probably the most significant, where it concerns mobile applications, is the lack of a storage solution which is safe, cheap and high-capacity. The most common methods of hydrogen storage are compression of the gas phase at high pressures, liquefaction at cryogenic temperatures and storage in solid state materials [175].

An interesting alternative which has attracted significant attention in the last decades is storage by adsorption in microporous materials [31, 32, 33]. These materials have a well defined open-pore structure, with often tunable shape and pore size, and have important applications in catalysis, gas adsorption, purification and separation. Among the various classes of microporous materials, zeolites [34, 35] present a few advantages: structural stability, large internal surface area, adjustable pore volume by cation exchange, and the fact that their adsorption isotherms exhibit no hysteresis [176], so that the process is completely reversible. Additionally, they are easy to synthesize in large quantities and at low cost. Extensive experimental surveys [177, 178, 179, 176, 180, 181, 182] have found the hydrogen storage capacity of zeolites to be < 2 wt% (weight-percent) at cryogenic temperatures and < 0.3 wt% at room temperatures and above, at low pressures.

The structure of zeolites is based on a framework of alternating AlO_4 and SiO_4 tetrahedra, the primary building units, which are arranged in space to form an intricate 3D network of cavities, channels and openings of various dimensions. Additionally, charge balancing cations are also present in the structure and because they are loosely bound to the framework, they may easily be exchanged for others. If a cation species is replaced with another of different

size, this will have an impact on the available internal surface and pore size, providing the means with which a zeolite's structure can be tuned to different guest species and applications [180, 179].

Even though zeolites have been used on an industrial scale for many years, there are still challenges in understanding, at an atomic level, the mechanisms for adsorption, diffusion and selectivity inside the material. In this respect, molecular simulation is an important complement to experimental studies. Monte Carlo and Molecular Dynamics have been used extensively for this purpose, due to their relative simplicity and efficiency when compared to full quantum chemistry calculations. Important reviews on the wide range of techniques and studies dealing with simulation of adsorption in zeolite systems were carried by Fuchs *et al.* [48] and, more recently, Smit and Maesen [183]. Several simulation studies have targeted the specific case of hydrogen adsorption in zeolites [184, 185, 186, 187, 188, 189, 190].

In the current work, the adsorption of molecular hydrogen in the zeolite NaA is studied by the grand-canonical Monte Carlo (GCMC) method, described in §2.2.6. In this scheme, a gas of guest molecules, hydrogen in this case, is in thermodynamic equilibrium inside and outside the host system, the zeolite. This equilibrium is achieved by allowing the number of guest molecules inside the zeolite, with which they interact, to fluctuate at a fixed chemical potential, which is related to the pressure of the reservoir gas.

The main ingredient in any simulation study of adsorption is the model of interactions between guest molecules and the host system. It is crucial that this interaction potential is designed and parametrized to be 1) simple enough that it can be used with relatively large systems and long simulation times and 2) capable of reproducing experimental quantities. Ideally, the model would be derived from theoretical considerations and whatever free parameters remained would be fit to reproduce experimental results. Outside of *ab initio* methods, there is still, however, considerable freedom in this choice, and results are highly sensitive to such details. In this work, a simple semi-empirical potential, proposed by Darkrim *et al.* [186], is used which combines van der Waals interactions modeled by a Lennard-Jones potential, Coulombic forces between partial charges and an extra term due to the induced polarization of the hydrogen molecule.

Adsorption isotherms are determined for a wide range of temperatures and pressures and compared with experimental data. The low pressure behavior is studied by analyzing the behavior of the isotherms as $P \to 0$ and comparing it with the result obtained by a direct method of computing the Henry's law coefficient. The next section introduces the principal concepts of adsorption as they pertain to the objectives of this work. In §5.3 the structure of the zeolite NaA is explained in detail, followed by a description of the potential model in §5.4. Implementation details are given in §5.5 and results in §5.6. The chapter finishes with the main conclusions. Part of the results presented this chapter were previously published in reference [191].

5.2   Principles of adsorption

Adsorption is the process by which a molecule in a gas phase interacts with a surface and becomes temporarily attached to it, departing from the gas phase, and increasing the local density near that surface. This phenomenon is a consequence of the rough potential energy landscape typical of an adsorbent surface, characterized by many local energy wells which trap the free roaming adsorbate particles. These wells may be shallow, corresponding to the effect of weak interactions like van der Waals forces, in which case the process is known as physisorption, or much deeper, as it happens when the formation of chemical bonds is involved (chemisorption). The present works attempts to model physisorption processes only, which require much lower activation energies. Furthermore, the discussion in this chapter will be limited to single component adsorbate systems.

A good measure of the capacity for a material to serve as a storage medium lies in its adsorption isotherms, essentially, the amount of gas molecules that are adsorbed into the material at a constant temperature, as a function of applied pressure. These can be obtained experimentally or by simulation, and compared with theoretical predictions based on some adsorption model. The most common experimental techniques are the volumetric and gravimetric methods, where the amount of adsorbed material is measured by expanding the gas into a known volume or a microbalance, respectively. From a simulation point of view, a straightforward way to obtain an isotherm is by performing GCMC simulations at several input pressures. This method yields directly the total number of molecules adsorbed into the structure, but also provides important microscopic-level information, such as the spatial distribution of the adsorbates inside the 3D framework, and the location of preferred adsorption sites.

5.2.1   Henry's law

The simplest possible isotherm treats the adsorbed phase as an ideal gas, where the guest molecules do not interact with each other, and is limited to a two dimensional monolayer immediately above the adsorbing surface. In these conditions, the ideal gas relation can be used:

$$P_a = \rho_a k_B T, \tag{5.1}$$

where ρ_a and P_a are, respectively, the density and pressure of the adsorbed phase. In the limit of low occupancy, one can further impose that the pressure of the adsorbed phase is directly proportional to the external pressure of the gas phase, P,

$$\lim_{\rho_a \to 0} P_a = cP, \tag{5.2}$$

where c is some unknown constant. Replacing into equation (5.1), one obtains

$$\rho_a = \frac{cP}{k_B T} = K_H P, \tag{5.3}$$

Equation (5.3) is known as Henry's law, and it is an accurate description of the real behavior of adsorbed phases at relatively low loadings. The proportionality constant, K_H, is known as Henry coefficient and is an important intrinsic characteristic of an adsorption material. If an experimental or theoretical adsorption isotherm is available, then K_H may be determined by observing the slope of the curve at the lowest pressures. In a computer simulation, it is possible to compute the Henry coefficient in a much more direct way. The method makes use of the fact that K_H is directly related to the excess chemical potential of the adsorbed molecules [183],

$$K_H = \beta \exp\left(-\beta \mu^{\mathrm{exc}}\right), \tag{5.4}$$

which can be solved by what is essentially the Widom test particle method (§3.2.2). Specifically, the following quantity is computed:

$$K_H = \beta \frac{1}{V} \int\limits_V \mathrm{d}\mathbf{r} \exp\left(-\beta \Delta U\left(\mathbf{r}\right)\right). \tag{5.5}$$

This integration is solved by an unbiased Monte Carlo scheme, by generating a large number of random positions $\mathbf{r}$ in the cell with uniform distribution, placing a single test adsorbate molecule at that position and calculating ΔU, its energy of interaction with an otherwise empty host. Equation (5.5) is valid for spherical particles with no internal degrees of freedom. For molecules with rotational degrees of freedom, the integration should include additional angular variables. In this work, this is handled by assigning a random orientation to the (linear) hydrogen molecules, uniformly chosen, every time a test insertion is performed.

This is a powerful method that outputs, with little effort, an unambiguous single value result that can be quickly compared against experimental data. This means it can be used to validate and calibrate zeolite-guest potential models and its parameters (see, for example, the work of Watanabe *et al.* [192] and Talu and Myers [193]) or to consistently compare the adsorbing performance of a wide range of materials, known or hypothetical (the work of Lin *et al.* [194], where thousands of zeolite and related structures were screened for their capacity to capture carbon dioxide, provides an excellent example of a large scale application of this idea).

Another important quantity, which is also experimentally available, is the isosteric heat of adsorption, q_{st}. It can be derived from the Clausius-Claperyon relation, equation (3.45), which relates two phases in thermodynamic equilibrium,

$$\frac{\mathrm{d}P}{\mathrm{d}T} = \frac{s_g - s_a}{v_g - v_a}, \tag{5.6}$$

where g labels the gas phase and a the adsorbed phase. The entropy s and volume v are differential functions,

$$s_i = \left(\frac{\partial S}{\partial n_i}\right)_{T,P} \text{ and } v_i = \left(\frac{\partial V}{\partial n_i}\right)_{T,P}. \tag{5.7}$$

In most conditions, the specific volume of the free gas phase is much greater than that of the adsorbed phase, leading to the approximation $v_g - v_a \approx v_g$ and

$$\frac{dP}{dT} = (s_g - s_a)\,\rho_g. \tag{5.8}$$

Let $\Delta s_{\text{ads}} = s_a - s_g$ be the change in differential entropies on adsorption and $\Delta h_{\text{ads}} = T\Delta s_{\text{ads}}$ the change in differential enthalpies. Usually, the positive value is reported instead, $q_{\text{st}} = -\Delta h_s$, and is known as the isosteric heat of adsorption. Equation (5.8) then becomes

$$q_{\text{st}} = T\left(\frac{dP}{dT}\right)_{n_a} \rho_g^{-1}, \tag{5.9}$$

where the partial differentiation is performed at constant coverage $n_a = \rho_a v_a$.

Equation (5.9) is general, but can be further simplified if it is assumed that the gas phase behaves as an ideal gas (the same approximation used to derive Henry's law of adsorption). In this case, the ideal gas law is applied to ρ_g, resulting in

$$q_{\text{st}} = \frac{k_B T^2}{P}\left(\frac{dP}{dT}\right)_{n_a} = -\left(\frac{d\ln P}{d\beta}\right)_{n_a}. \tag{5.10}$$

Thus, the isosteric heat of adsorption may be determined by differentiating a series of isotherms at constant loading (n_a). Additionally, applying equation (5.3) yields a similar relation with the Henry coefficient,

$$q_{\text{st}} = \left(\frac{d\ln K_H}{d\beta}\right)_{n_a}. \tag{5.11}$$

5.2.2 Langmuir and virial isotherm

A very common model for describing monolayer adsorption at higher loadings is the well known Langmuir isotherm,

$$\rho_a = \frac{K_H P}{1 + (K_H/\rho_{sat})\,P}, \tag{5.12}$$

where K_H is the Henry coefficient, and ρ_{sat} the saturation density, the maximum amount of adsorbed material the system may take. This model treats the adsorption phenomenon as a dynamic equilibrium between free particles in the gas phase and discrete adsorption sites, which may be vacant or occupied. It assumes that all adsorption sites are equivalent and independent from each other and restricts adsorption to a single layer [195]. For low pressures, the Langmuir isotherm reduces to the Henry's version, equation (5.3). A variation

of the Langmuir model exists which considers two distinct types of adsorption sites. The aptly named dual-site Langmuir isotherm is sometimes required to explain the shape of more complex experimental isotherms [183].

A virial form of the adsorption isotherm is also sometimes used [195],

$$\frac{P}{\rho_a} = \exp\left[A + B\rho_a + C\rho_a^2 + ...\right], \tag{5.13}$$

where the first virial coefficient is related to the Henry coefficient, $K_H = \exp(-A)$. An advantage of equation (5.13) is that it provides the means with which the Henry constant can be determined from experimental data when not enough data points are available at low loading regimes. In principle, a plot of $\ln(P/\rho_a)$ with ρ_a remains linear at much higher concentrations. The virial isotherm is useful to fit adsorption data, but it is essentially empirical, providing very little insight into the adsorption process [195].

Other adsorption models are available which attempt to explain multilayer adsorption or the adsorption of mixtures [195].

5.2.3   Absolute vs. excess adsorption

It is important to note that, while molecular simulation yields the total amount of molecules inside the cell volume (the absolute value N_{abs}), experiments are usually concerned only with that portion of the gas that is adsorbed into a thin layer adjacent to the surface of the solid. This quantity, N_{ex}, the excess amount, is calculated as the total amount minus the number of molecules that would otherwise be present in the same volume [196], i.e.,

$$N_{\text{ex}} = N_{\text{abs}} - \rho_b V_b, \tag{5.14}$$

where ρ_b is the density of the bulk phase of the hydrogen gas and V_b is the void volume, a measure of the total volume accessible to the guest molecules, which includes the empty space inside the porous material and the experimental apparatus. There is, unfortunately, some ambiguity on the definition of the void volume. Usually, adsorption experiments of helium gas at a specific reference state are performed to determine V_b, because helium has weak interaction with the atoms of the solid and, therefore, it is assumed that it has no excess adsorption, so that $V_b = N_{\text{abs}}^{\text{He}}/\rho_b^{\text{He}}$ [197]. This assumption is debatable even at room temperatures, and the choice of reference state used to carry the helium density experiment, which is often omitted from the source, may have an impact on the reported isotherms, especially at high pressures [198]. This makes independent comparison of simulated and experimental results difficult. For this reason, the results of the present work are shown as unambiguous absolute, rather than excess, quantities.
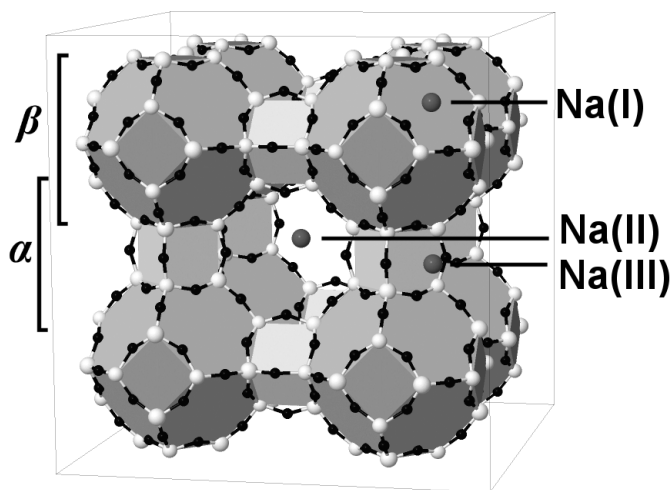
Figure 5.1: Unit cell of the zeolite NaA with oxygen atoms in black, T-atoms (Al/Si) in white and representative positions of the three types of Na$^+$ in dark gray. Eight β cages are represented in the corners of the framework surrounding a central α cage.

5.3 Structure of the NaA zeolite

The dehydrated NaA zeolite crystal (also known as 4A) is a cubic arrangement of unit cells with composition $\{Na_{12}[(AlO_2)_{12}(SiO_2)_{12}]\}_8$. The building blocks are alternating AlO_4 and SiO_4 species, corner-sharing tetrahedra with one aluminum or silicon (known as a T atom) in the center bonded to four oxygens on the corners, which are shared between blocks. Due to Lowenstein's rule that states that Al-O-Al linkages are energetically unfavorable [183], when the Al/Si ratio is one, each oxygen will connect two different T atoms (Al-O-Si). These tetrahedral entities are arranged in space to form a porous network of small and large cavities, which are known, respectively, as β and α cages, as shown in Figure 5.1. The β cages (also called sodalites) are shaped roughly like a truncated octahedron, with an approximated internal radius of 5 Å. They are connected by their square faces in a cubic arrangement. At the center of the cube formed by 8 sodalites in the vertices, there is a large opening, the α cage, which has an internal radius a little above 7 Å. The windows of the α cage are formed by 8-oxygen rings with a diameter of approximately 6.8 Å. It is through these open windows that the guest molecules enter the hollow space inside the α cage, where most adsorption is expected to occur. However, the presence of the large Na cations almost at the center of these windows (as discussed below) will have a detrimental effect. The unit cell is cubic with length $a = 24.56$ Å and belongs to the space group Fm$\bar{3}$c [199]. The coordinate positions of the atoms were taken from x-ray diffraction studies of this zeolite [199].

The aluminosilicate framework, Al-O-Si, has a net negative charge due to the mixed content of Al^{3+} and Si^{4+} ions. This is compensated by the introduction of positively charged ions in extra positions of the framework. For the particular case of the NaA zeolite, the counter-ions are Na$^+$, but due to the high ion-exchange property of zeolites, they can be easily

Table 5.1: Description of the three types of Na atoms in the zeolite NaA.

type	number per unit cell	occupancy	position
I	64	1	At the center of each 6-oxygen ring that make up the windows of the sodalite (β) cages.
II	24	1/4	One for each window of the α cage (8-oxygen ring), with roughly equal probability in one of four possible locations slightly off-center on the plane of the ring.
III	12	1/12	Off-plane at the center of the 4-oxygen rings that link the sodalites.

replaced. Experimental results on the influence of cation exchange on zeolites [180, 179] show that replacing sodium with a larger cation has a significant impact on the hydrogen uptake, and higher still on the zeolite A species, due to the already relatively small pore size.

On the zeolite NaA, there are three different types of sodium cations, classified according to the three main extra-framework sites they can occupy [34]. Details are given in Table 5.1 and representative sites are sketched in Figure 5.1. As described in the table, there is some disorder associated with the occupancy of those positions.

Molecular dynamics studies of the dehydrated NaA zeolite at room temperature by Faux *et al.* [200] have shown that the Na(I) atoms remain relatively fixed, while the Na(II) atoms display significant mobility, migrating between the four degenerate positions in the 8-oxygen ring as well as moving in and out of the ring plane. The Na(III) atoms also display out of plane mobility at room temperature. Significant migration of the sodium cations between the type II and III sites has been shown to occur in the presence of water [201].

Due to their large size and position in the windows of the α cages, the Na cations have an important effect on hydrogen uptake by (1) blocking the entrance of the molecules into the space inside and (2) limiting the total void volume available [180].

5.4   Potential model

The total potential energy U of the system which contains the host zeolite and guest hydrogen molecules is a sum of the zeolite-adsorbate (ZA), adsorbate-adsorbate (AA) and zeolite-zeolite (ZZ), or internal, interactions,

$$U = U^{ZA} + U^{AA} + U^{ZZ}. \tag{5.15}$$

For the purposes of studying adsorption at normal pressures and temperatures, it is usual practice to impose the rigid framework approximation. This avoids the calculation of the internal energy between zeolite atoms, U^{ZZ}, which usually requires complex force fields designed for bonded interactions. This approximation allows for longer simulation times and the study of larger and more complex systems. While useful, it is a necessarily less accurate

Table 5.2: Lennard-Jones parameters and partial charges used in this work, using best fit from [186]. Na atoms have different charges depending on their type. For the hydrogen molecule, two charges are located at the positions of the protons (H) and one at center of mass (CM).

	Al	Si	Na	O	H_2
$\sigma\,(\text{Å})$	1.016	0.677	3.5	2.45	2.958
$\epsilon\,(\text{K})$	19.1	18.6	8.0	42.0	36.7
$q\,(|e|)$	1.48	0.8	(I) 0.864 (II) 0.606 (III) 0.196	-0.75	(H) 0.4829 (CM) -0.9658

description of reality. This has naturally raised some concern on how reliable some of the measured properties are, in particular, dynamic quantities such as the rate of diffusion of the guest molecules inside the structure (typically determined by MD simulations). Demontis and Suffritti, in an extensive review [202], argue that if the molecules are small enough and in high dilution, the effects of lattice vibrations in the diffusion properties are minimal. Some workers have incorporated a fully flexible zeolite structure in their studies of the NaA zeolite [200]. Others have kept the Al-O-Si framework rigid while still allowing the much more mobile Na atoms to move about their positions [186, 187]. In this work, all zeolite atoms will be fixed in their experimentally determined positions.

If the creation and destruction of chemical bonds between atoms is disregarded (which would enter the realm of chemisorption and outside the scope of this work), then, the host-guest and guest-guest interaction is limited to van der Waals and, if the molecule is multipolar, Coulombic contributions.

The van der Waals term can be modeled by the 12-6 Lennard-Jones (LJ) potential [203], equation (2.60), where the value of the parameters ϵ and σ depend on the atoms being considered. Potentials which include higher order dispersion terms or an exponential Born-Mayer form for the short-range repulsion have also been used [48].

In this work, a LJ interaction site is placed at the position of each atom in the zeolite and at the center of mass of each hydrogen molecule. The choice for the values of the LJ parameters is not straightforward, and they are usually adjusted to every situation, in order to fit the purpose and data available to the researcher, which justifies the fact that no consistently adequate set of parameters can be found in the literature. The best fit parameters obtained by Darkrim *et al.* [186] are used in this work and are reproduced in Table 5.2, a pair of ϵ and σ values for every atom species in the system. The cross interaction parameters between atoms of species i and j, are given by the Lorentz-Berthelot mixing rules, equation (4.7), with the single component parameters given in Table 5.2.

A Coulombic term describes the interaction between the partial charges in the zeolite structure and the (permanent) hydrogen multipole. The electrostatic energy between two point charges q_i and q_j is given by equation (2.62).

The partial charges in the zeolite may be determined experimentally or theoretically, using some quantum chemistry calculation, the most common of which is the electronegativity equalization method [204].

Following the approach of Darkrim *et al.* [186], the hydrogen quadrupole is modeled by a distribution of 3 point charges: two with value $q_H = 0.4829 \, |e|$ located at the position of the hydrogen atoms, separated by $0.741 \, \text{Å}$, and another with value $-2q_H$ positioned at the center of the molecule. Intermolecular interactions are calculated by summing over the three charges. The molecule is also assumed rigid, so no intramolecular interactions need to be considered.

Additionally, some authors also consider an interaction between charges in the zeolite and the dipole induced in the hydrogen molecule by the electric field present in the structure. This polarization energy is calculated by the first term of the multipole expansion [48, 184, 186]. For a molecule at position $\mathbf{r}$, it is given by

$$u^{\text{pol}} = -\frac{1}{2} \alpha_{H_2} \mathbf{E}^2 (\mathbf{r}), \tag{5.16}$$

where $\alpha_{H_2} = 0.806 \, \text{Å}^3$ is the mean polarizability of the molecule [186] and $\mathbf{E}(\mathbf{r})$ the electric field at that position. In this work, the electric field is calculated from the partial charges in the zeolite only, thus ignoring guest-guest polarization effects. Furthermore, it is assumed that the polarization of a molecule is independent of its orientation (only a single, mean, polarizability is used). It is a fair assumption at room temperature but disputable at lower temperatures. In contrast, Anderson *et al.* [184] used the molecular polarizability tensor and explicitly accounted for the anisotropy of the polarization energy.

In summary, in this work, the total energy of the system (ignoring the internal energy of the zeolite structure) is calculated as

$$U^{H_2} = \sum_{\substack{i \in \{Z,A\} \\ j \in \{A\}}} 4\epsilon_{ij} \left[\left(\frac{\sigma_{ij}}{r_{ij}} \right)^{12} - \left(\frac{\sigma_{ij}}{r_{ij}} \right)^{6} \right] + \frac{1}{4\pi\varepsilon_0} \sum_{\substack{i \in \{Z,A\} \\ j \in \{A\}}} \frac{q_i q_j}{r_{ij}} - \frac{1}{2} \sum_{i \in \{A\}} \alpha_{H_2} \mathbf{E}^2 (\mathbf{r}_i), \tag{5.17}$$

where r_{ij} is the distance between atoms i and j, and the notation $\{Z, A\}$ and $\{A\}$ are meant to indicate that the summations are carried over all zeolite (Z) interaction sites and/or all sites on the adsorbate (A) molecules, depending on the type of interaction being evaluated, as explained in the text.

5.4.1   Feynman-Hibbs effective potential

A correct treatment of an hydrogen fluid at very low temperatures cannot safely ignore quantum contributions, which are significant due to the low mass of this molecule. A com-

parison of classical and quantum simulations of hydrogen adsorption in carbon nanotubes at 77 K, for example, has shown that the first can overestimate the adsorption by as much as 20% [205].

One way to deal with quantum contributions in an MC simulation is to use the path-integral formalism of Feynman [206]. In this framework, each quantum particle is replaced by a necklace of harmonically coupled beads, and necklaces interact with each other by a bead-bead pairwise potential [207]. The number of beads per necklace, B, is increased until the equilibrium properties of the system no longer change with this number. The treatment becomes exact for $B \to \infty$ and reverts to the classical approximation for $B = 1$. Even considering an optimal value of B, path-integral MC (PIMC) simulations are still costly, which led to the development of effective potentials that approximate the path-integral necklace-necklace interactions by a simple pair term. One such approach is based on the Feynman-Hibbs (FH) [206] variational estimate of the quantum partition function, described next.

The FH variational approach describes the spread in the position of a quantum particle due to the uncertainty principle by a Gaussian packet of width $\hbar/\sqrt{12mk_BT}$, centered at its center of mass. If exchange interactions are neglected (they are only meaningful for extremely low temperatures and high densities [208]) the partition function can be cast as

$$Z^{\text{GFH}} = \frac{1}{\Lambda^3 N!} \int_V \mathrm{d}\mathbf{r}^N \exp\left[-\beta \sum_{i<j} u^{\text{GFH}}(r_{ij})\right], \tag{5.18}$$

where

$$u^{\text{GFH}} = \left(\frac{6m_{\text{red}}}{\pi\beta\hbar^2}\right)^{3/2} \int u(|r+R|) \exp\left(-\frac{6m_{\text{red}}}{\beta\hbar^2}R^2\right) \mathrm{d}R \tag{5.19}$$

is the Gaussian Feynman-Hibbs (GFH) effective potential between two particles with reduced mass m_{red}, obtained after applying the Gaussian smearing to the classical, spherically symmetric, potential u. In order to have a usable form of this effective potential, a Taylor expansion is carried around r to the second order of R, leading to the quadratic form of the FH potential (QFH),

$$\begin{aligned} u^{\text{QFH}}(r) &= u(r) + \frac{\beta\hbar^2}{24m_{\text{red}}}\nabla^2 u(r) \\ &= u(r) + \frac{\beta\hbar^2}{24m_{\text{red}}}\left[u''(r) + 2\frac{u'(r)}{r}\right], \end{aligned} \tag{5.20}$$

where the derivatives are taken with respect to the distance between particles. The quadratic Feynman-Hibbs potential is an effective way to incorporate quantum corrections in a classical simulation, with good approximation at moderately low temperatures and densities. Equation (5.20) captures two essential quantum effects. When the energy is near a minimum, the curvature of $u(r)$ is positive and the corrections raise the energy level, modeling the zero-

point effect. When the energy is near a maximum, $\nabla^2 u$ is negative, decreasing the energy barrier, which models the tunneling effect [209]. This potential has been used extensively in simulations of atomic and molecular fluids [207, 210, 211] and adsorption phenomena [205, 212, 213] at low temperatures.

In this work, for simplicity, the FH correction is applied only to the Lennard-Jones term of the potential (the quadratic correction for the Coulomb potential is zero, and the contribution due to the polarization energy is ignored). Thus, the total potential energy of the zeolite-hydrogen system with quantum corrections is now given by

$$U^{\mathrm{QFH}} = U^{H_2} + \sum_{\substack{i \in \{Z,A\} \\ j \in \{A\}}} \frac{\beta \hbar^2}{m_{\mathrm{red},ij} \sigma_{ij}^2} \epsilon_{ij} \left[22 \left(\frac{\sigma_{ij}}{r_{ij}} \right)^{14} - 5 \left(\frac{\sigma_{ij}}{r_{ij}} \right)^8 \right], \tag{5.21}$$

where U^{H_2} is defined in 5.17. For the interaction between two hydrogen molecules, the reduced mass is $m_{\mathrm{red}} = m/2$, where m is the mass of an H_2. Since the zeolite atoms are assumed fixed, their mass is infinite in this context and $m_{\mathrm{red}} = m$ for an hydrogen-zeolite atom pair.

This expansion of the GFH potential is valid under normal densities and for $\Lambda \leq 0.5\sigma$, where Λ is the thermal de Broglie wavelength, equation (2.8) [207]. For the current system of hydrogen molecules with $\sigma = 2.958\,\text{Å}$ at $T = 77\,\text{K}$, $\Lambda = 0.47\sigma$, which falls within that limit. Additionally, the inclusion of the next order term $(\hbar^4)$ has been shown to provide little benefit when simulating bulk fluids [207].

5.5   Simulation details

GCMC simulations of the adsorption of molecular hydrogen into the zeolite NaA were performed at different temperatures and gas pressures. At a given Monte Carlo step in this algorithm, one trial move is attempted that consists of an insertion of an H_2 molecule, with random orientation, at a random position in the zeolite, or a removal of an H_2 from the configuration, and is accepted or rejected according to the rules defined in §2.2.6. The two operations are attempted with a 50% chance each. For moderate to high temperatures only those two operations were performed, but it was determined that, for the lowest temperatures, specifically $T = 77\,\text{K}$, the convergence of the chain is much improved by the inclusion of the displacement and rotational moves alongside the insertion and removal operations. When all 4 operations are included, each is attempted with a 25% chance.

The GCMC simulation takes as an input the chemical potential μ of the hydrogen gas reservoir rather than the experimentally accessible external pressure, P. The equation of state of the Lennard-Jones fluid of Johnson *et al.* [214], with the parameters for the $H_2 - H_2$ LJ interaction as given in Table 5.2, was used to convert the imposed pressure P to μ. This conversion ignores the contribution of the comparatively much weaker electrostatic interac-

tions to the properties of the gas reservoir. By using the Widom test particle method with the full $H_2 - H_2$ potential (LJ and electrostatic terms), the real chemical potential of the model was computed, at some states, and compared with the result of the equation of state. The approximation was deemed adequate for the range of temperatures and pressure considered.

In this work, a single unit cell of NaA was considered, the structure of which is detailed in §5.3. T-sites were filled with alternating Al and Si atoms. For each Na(II) atom, one of the four possible positions on the plane of the 8-oxygen ring was randomly chosen with uniform probability at the beginning of the simulation. Likewise, the Na(III) sites were filled with 1/12 occupancy, randomly selected. In general, it was found that the specific configuration of sodium sites had no influence on the final observed adsorption capacity, within statistical accuracy. Following the most common approach, this work used a fixed zeolite structure throughout. The final result was a host configuration with 672 atoms. Standard periodic boundary conditions were applied.

The LJ potential was truncated to half the box length and long range corrections were added as described in previous chapters. To handle the long-ranged coulombic interactions between the hydrogen quadrupoles and the host charges, simple truncation is not adequate, and the Ewald summation method, described §2.3.2, was used instead. For the interaction between two H_2 molecules, however, the energy drops rapidly with distance and it can be calculated directly as a sum of $q_i q_j / r_{ij}$ terms over all 3 charges in each molecule, with the usual truncation to the minimum image. The internal interactions in the zeolites and H_2 molecules are not calculated since both are assumed rigid.

The electric field at a point $\mathbf{r}$, required for evaluation the polarization energy U_p, was calculated by extending the Ewald method to the first derivative of the electrostatic potential, as described in §2.3.3. This way, the electric field may be calculated, with precision, at any position during the course of the simulation. This is in contrast with methods which precompute the electric field at discrete positions in the cell, by solving the gradient explicitly or through other techniques, and use interpolation when necessary. As an alternative, Anderson *et al.* [184] chose to approximate $\mathbf{E}$ by a sum, over all charges in the system, of q/r^2 terms with an exponential drop-off switch. The approach taken here should provide more precise results at relatively low extra cost.

A typical GCMC simulation run consisted of 3×10^6 MCS, each involving one insertion or removal attempt. The first third of the length of the run was reserved for the equilibration stage, and thus discarded. The number of observed H_2 molecules per unit cell was registered every 10 MC steps, and ensemble averages calculated. A wide range of temperatures, from $T = 77$ to $300\,\mathrm{K}$, and pressures, from $P = 1$ to $180\,\mathrm{MPa}$ was investigated.

The Henry coefficient was calculated by the particle insertion method for about 40 temperatures between 200 and 600 K. For each temperature, 3×10^6 different random positions and orientations for the test molecule were generated, and equation (5.5) was solved.
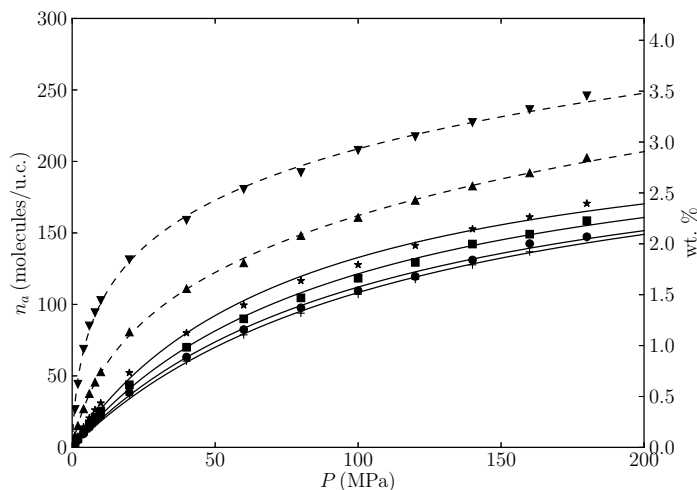
Figure 5.2: Simulated hydrogen adsorption isotherms in the zeolite NaA at various temperatures, in molecules per unit cell (u.c.) or weight percentage (wt%). From top to bottom $T =$150 K, 200 K, 250 K, 273 K, 293 K and 303 K. The solid lines are Langmuir isotherm fits to the data, and the dashed lines are second order virial fits.

5.6 Results

The adsorption isotherms obtained in this work using the classical potential model described in §5.4, are represented in Figure 5.2 for several moderate to high temperatures. These are measured in terms of the total number of adsorbed H_2 molecules per unit cell (u.c.) of the NaA zeolite, as well as in gravimetric density (expressed as wt%), which is the percentual mass of adsorbed hydrogen per unit mass of the system (adsorbed gas + adsorbent material). These isotherms are of type "I", according to the definition of reference [195]. As expected, adsorption increases with both pressure and temperature, reaching values of 2 wt%, corresponding to about 140 molecules per unit cell of the zeolite, at room temperature and very high pressures, and 3.5 wt% at 150 K. The very low temperature case is discussed further ahead. For temperatures starting at $T = 250$ K, the results were fitted to a simple Langmuir isotherm, equation (5.12). For the lower temperatures, however, the fitting was not satisfactory and a functional virial isotherm, equation (5.13), was used instead.

At room temperature and moderate to high pressures ($P \geq 10$ MPa) the results closely match those obtained by Darkrim *et al.* [186]. At $P =$10, 40 and 70 MPa, these authors report an experimental (absolute) adsorption of 0.35, 1.0 and 1.4 wt %, respectively.

In the low pressure regime ($P < 10$ MPa), at room temperatures, there is significantly more experimental data available in the literature for comparison. However, differences in experimental apparatus, sample preparation, void volume determination or measuring procedures also mean that it is difficult to find consistent results between these works. This is evident in Figure 5.3, where experimental results from different sources are plotted against the simulated isotherms obtained in this work. The present results from GCMC simulations
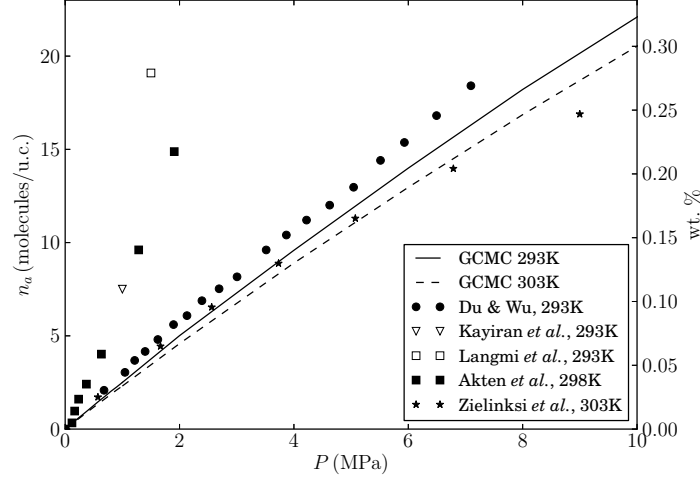
Figure 5.3: Low pressure, room temperature adsorption isotherms. Comparison between simulations (GCMC) and experimental results by Du & Wu [181], Langmi *et al.* [176], Kayiran *et al.* [179], Akten *et al.* [187] and Zielinski *et al.* [215].

with a classical potential model are in good agreement with the measures by Du and Wu [181], and Zielinsky *et al.* [215] at, respectively, 293 K and 303 K. The hydrogen adsorption at these temperatures reaches almost 0.3 wt% at pressures just below 10 MPa. In contrast, Langmi and coworkers [176] claim that this amount of adsorption happens at much lower pressures (1.5 MPa), while Akten *et al.* [187] report a value closer to 0.2 wt% at $P = 2$ MPa, which is still about three times higher than what was obtained in this work. It is worth noting that Akten *et al.* also performed GCMC simulations using a potential similar to the one used here, with the difference that they chose not to include LJ interaction centers in the Si and Al atoms, and no polarization term was considered. Their potential parameters were optimized to reproduce experimental results [187]. The consequence is that ϵ is increased for the oxygen atoms, to compensate the absence of the Si/Al LJ and polarization interactions, but the Na atoms are notably smaller, $\sigma = 2.805$ Å, which might help explain the higher rate of adsorption observed in their simulations, since the blocking effect of the extra framework sodium atoms is substantially reduced.

In the low temperature regime, at $T = 77$ K, Langmi and coworkers [176, 180] report an hydrogen uptake for the this zeolite of 1.54 wt% at 1.5 MPa, with similar results obtained by Du and Wu [181]. The simulations in this work using the purely classical potential, equation (5.17), predict an hydrogen uptake that is almost twice that figure (2.7 wt%) at the same pressure. The full isotherms are plotted in Figure 5.4. The inclusion of the quadratic Feynman-Hibbs corrections to the Lennard-Jones H_2-H_2 and H_2- zeolite interactions, results in a decrease of the adsorption capacity to about 2.2 wt%. This result can be attributed to the increase in the effective diameter of the hydrogen molecules due to quantum spreading. While the value of 2.2 wt % is still far from the experimental results from those authors, this
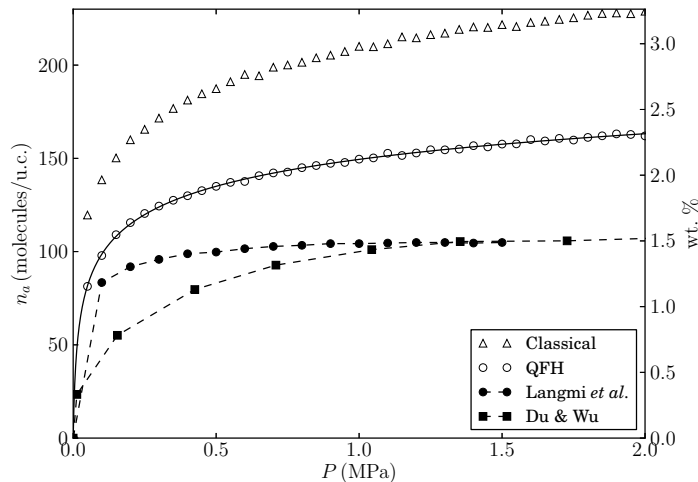
Figure 5.4: Hydrogen adsorption at 77 K. Comparison between simulations using the classical potential, equation (5.17), QFH effective potential, equation (5.21), and experiments by Langmi *et al.* [176, 180] and Du and Wu [181]. The dashed lines are visual guides and the solid line is a fitted virial isotherm.

shows that the inclusion of quantum corrections is important to correctly model hydrogen adsorption in this regime. This result merits a more detailed analysis of the role of quantum effects in the low temperature adsorption, a study which would be more adequately handled by PIMC simulations.

Even with the inclusion of QFH corrections, the low temperature/pressure estimate from this work seems overly optimistic and in contrast with established results which put the adsorption capacity of this, or any other type of common zeolite, at a maximum of about 2.0% in the low temperature regime [182]. Clearly the parameters of the model, which were fit to moderate temperature and higher pressure data, are not transferable to low temperatures without further adjustments.

Using the particle insertion method, the Henry coefficient was determined as a function of temperature, and results are plotted in Figure 5.5. To check for the consistency of these results, low pressure isotherms were constructed, for some temperatures, by performing additional GCMC simulations between 0.1 and 1 MPa. The slope of these curves was extracted to give an estimate for the Henry coefficient, which is plotted in Figure 5.5 (a) as well, showing perfect agreement between the two methods. The isosteric heat of adsorption at low loading was determined using equation (5.11), from the slope of the $\ln K_H$ vs β curve, plotted in Figure 5.5 (b). For the highest temperatures, the curve departs slightly from the linear behavior and these points were not considered in the fit. The result was $q_{st} = 743 \pm 1$ K or 6.18 kJ/mol.

In order to provide a better understanding of the adsorption affinity of the zeolite NaA structure, the full guest-host potential energy, equation (5.17), of a single H_2 molecule is represented as 2D density maps along two planes that cross a unit cell of the material, in Figure 5.6. The grand-canonical distribution function, equation (2.18), states that the
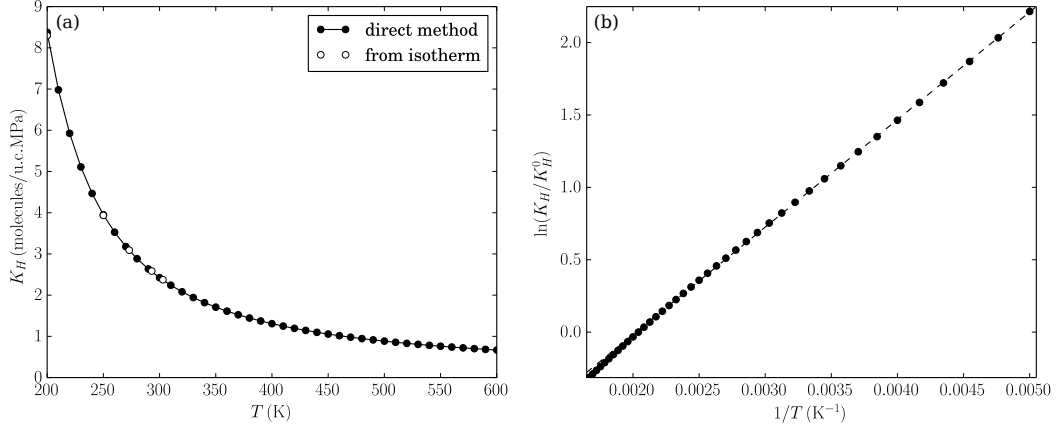
Figure 5.5: The Henry coefficient of hydrogen adsorbed into the NaA zeolite determined from the test particle method: (a) as a function of temperature; and (b) logarithm vs inverse temperature linear relationship.
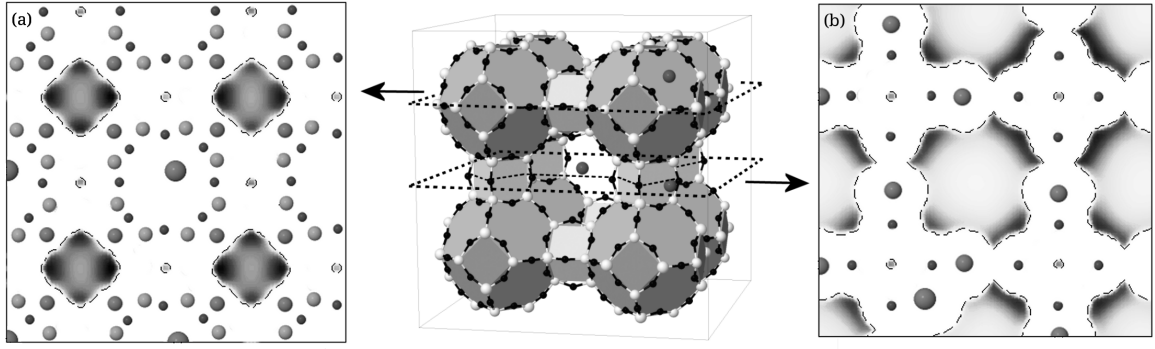
Figure 5.6: Density plots of the potential energy, βU^{ZA}, of an H_2 molecule in an empty zeolite, averaged over all orientations, along two (001) planes of the unit cell: (a) goes through the center of the sodalites and contains α cage windows (8-oxygen rings); and (b) goes through the center of the α cage. Only areas with negative energy are shaded, and the darker the tone the more negative and, thus, more energetically favorable. The spheres represent framework atoms in the vicinity of the plane.

probability of finding a particle at position $\mathbf{r}_i$ grows with $\exp\left(-\beta U\right)$, so that adsorption is expected to occur for the lowest values of U. The shaded areas in the plots are regions where the total potential energy is negative, which means that the framework atoms will exert an attractive interaction on the guest particle. The non-shaded regions on the figures are areas that lay in the repulsive part of this potential, which increases very rapidly (as r^{-12}) as the atoms begin to overlap. The frontier between these two regions may be used as a measure of the available volume for adsorption. The location of this separating surface is not just a function of the static energy of the zeolite structure, but also depends on imposed pressure on the system (related to the chemical potential) and the density of molecules already present in the cell.

Figure 5.6(b) clearly shows a large volume for retaining guest molecules in the center of

the α cages, with a strong energy minimum in a thin layer adjacent to the internal surface of the cage, interrupted only by the repulsive effect of the large sodium atoms positioned in the windows of the cage. These Na(II) atoms, which have the largest atomic radius (as measured by the Lennard-Jones parameter σ), have the most influence on the available area for adsorption inside the zeolite. At the very center of the α cage, the interaction felt by the adsorbed particles is only slightly attractive and the hydrogen molecules present there would be mostly unconstrained by the zeolite. Figure 5.6(a) shows that there is another energetically favorable region, in a small volume inside the sodalite (β) cages. In simulations, which in this setting are only concerned with equilibrium properties, some molecules were found in these small, confined areas. In a real material, it is questionable that the adsorbate molecules would have enough energy to overcome the high energy barrier imposed by the 8 Na(I) atoms blocking the entrance to the sodalites. Another possible, albeit unlikely, adsorption site is a very small region in the center of the quasi-cubic cages that connect the sodalites. Simulation shows that H_2 molecules are found there only for the largest values of pressure or lowest temperatures.

5.7   Conclusions

In this chapter, the adsorption of molecular hydrogen in the zeolite NaA was studied by grand-canonical Monte Carlo simulations, for a wide range of temperatures and pressures. The potential model and parameters used show good agreement with experimental results at room temperatures, although, at low pressures, the observed storage capacity reported in different sources is very sensitive to experimental details and varies widely, making quantitative comparison difficult.

For a low temperature, low pressure regime, the situation is more clear, with the current classical potential model clearly overestimating the adsorption capacity of these materials. It was found that, in this regime, the inclusion of quantum corrections given by the quadratic Feynman-Hibbs effective potential lowers this estimate by as much as 30%. As such, this effects cannot be ignored at low temperatures.

An analysis of the potential energy field inside the zeolite shows that the volume available for adsorption is, for the most part, constrained by the extra-framework Na atoms. This is justified by their large LJ parameter σ and small ϵ, which results in a wide repulsive core with a negligible attractive energy well. Adjustment of these parameters will have a very direct effect on the total amount of adsorbed gas.

The linear relation between the hydrogen uptake and input pressure in the limit of zero loading is verified, and the corresponding proportionality constant, the Henry coefficient, is calculated as a function of temperature. Systematic validation of any model at low pressures can be done by comparing such a curve with experimental observations of $K_H(T)$.

The present results demonstrate the difficulty in defining an all-encompassing potential

model that works for a broad range of temperatures and pressures. More so if one wishes to transfer the model to other guest molecules and host systems. Local adjustments of the parameters of the model from experimental data, when available, are always necessary. Nevertheless, important data can be extracted from a microscopic description with an approximate potential model of interactions, such as the location of optimal adsorption sites or the main potential barriers that block the adsorption of the guest molecules, which can help to guide the modeling of new, optimized, hydrogen storage materials.

Chapter 6

Conclusions and Future Research

The flexibility and power of the Monte Carlo method, supported by a variety of different techniques, was explored in the work presented in this thesis, which focused on three distinct applications.

First, the solid-fluid transition of the $n-6$ Lennard-Jones system was investigated. This is a superset of the classic Lennard-Jones pair potential where the repulsive term is proportional to the n-th power of the distance between particles. It is an important class of potentials with applications in several force-fields, but whose properties have not yet been so thoroughly investigated as those of the more common $12-6$ Lennard-Jones. In particular, the solid-fluid phase diagram of this system was reported for the first time only recently. The current work presents alternative results, which show slightly higher freezing and melting densities. Precise measurements of the solid-liquid-vapor triple points are also presented, which improve on previous approximated estimates.

The methodology used in this work was based on free energy calculations, carried independently for each phase, which is known to provide coexistence results with excellent precision. The task of computing the free energy of a system at conditions near coexistence is significant, requiring knowledge of reference states and many simulations in between. Here, a method was devised, based on the multiple histograms technique, which combines standard simulations performed with different Hamiltonians and extracts their free energy differences. This allows for the computation of the free energy of a generic $n-6$ system using the $12-6$ as a reference, which can greatly simplify the process. In the future, this method, supported by the data points provided in this work, can be used to compute free energies for other interaction models without resorting to the usual references at distant thermodynamic states, aiding the process of determining the phase diagrams of generic systems.

A question which surfaced recently and was left unanswered was that of the existence of a stable bcc phase, based on the observation that, at high temperatures, the $7-6$ LJ approximates the inverse power law potential with the same exponent, which does exhibit such a phase. Evidence points to a stable bcc structure for reduced temperatures approximately

below 100, but free energy calculations in this region of the phase diagram were inconclusive. An alternative technique such as the lattice switch method of Bruce *et al.*, especially designed to identify the relative stability of two solid phases, should be considered to answer this question in the future.

The phase diagram of the fullerene C_{60} was also studied, in particular, the transition from the orientationally disordered fcc phase at room temperatures to the highly ordered sc low temperature phase. Three atomistic models, some of which considered partial charges at different locations, were compared and it was concluded that the model due to Lu, Li and Martin is the one that can better reproduce the orientational properties of both phases, predicting the proper rotation angles for molecules in both the majority and minority populations in the sc phase and a highly disordered fcc phase. It also correctly predicts an all-H phase for sufficiently high pressures. This model fails, however, to replicate the experimental observation that a high fraction of both H and P oriented molecules can be found close to the transition temperature, and instead predicts a near 100% occupation by the majority population. This is a direct consequence of the high energy gap between both states, which overestimates the experimentally predicted value. Future models should attempt to correct this discrepancy.

For this part of the work, the anisotropic NPT MC algorithm was implemented. This technique allows for variations in the lengths of the simulation cell in all three directions and its internal angles, expanding the sampling to variable cell sizes and shapes. This is essential when dealing with solid phases that may undergo structural phase transitions which would otherwise be forbidden in the isotropic NPT scheme. This work helped overrule this possibility for the two bond charge models considered by demonstrating that the unit cell remained cubic for the range of pressures and temperatures investigated. For very high pressures, C_{60} polymeric phases emerge which cause a distortion of the lattice, and this is an interesting area of research which is fit for investigation with this technique. The study of these phases would also require more complex models which account for intramolecular interactions, so that the creation and formation of covalent bonds between C_{60} monomers can happen dynamically.

Finally, the adsorption of molecular hydrogen in the microporous zeolite NaA was investigated by GCMC simulations. A model of interactions was used which considers van der Waals, electrostatic and induced polarization terms. Expressions were derived for the electric field in the Ewald summation method, which allowed for the precise computation of this quantity, at any point in the simulation, with little overhead.

The results show good agreement with experimental data at room temperatures but less so in the low temperature regime. It was demonstrated that, at 77 K, the amount of adsorbed hydrogen using the classical potential is grossly overestimated. The inclusion of quantum effects, in an approximated way, through the use of the quadratic Feynman-Hibbs effective potential, led to a decrease of the hydrogen adsorbed by as much as 30%, showing that these

effects cannot be ignored at these temperatures.

In the future, this work may be extended to study adsorption in other zeolite species. The procedure of recalibrating the potential model would entail recalculation of the partial charges in the host system, through the electronegativity equalization method or similar techniques, and adjustment of the Lennard-Jones parameters by replicating the experimental Henry coefficient and isosteric heat of adsorption. Other structures, such as metal organic frameworks and carbon porous materials, which, in the last years, have reveled high hydrogen uptake capacities, are also worth investigating.

Bibliography

[1] N. Metropolis, A. W. Rosenbluth, M. N. Rosenbluth, A. H. Teller, and E. Teller. Equation of State Calculations by Fast Computing Machines. *The Journal of Chemical Physics*, 21:1087, 1953.

[2] W. W. Wood. Monte Carlo Calculations for Hard Disks in the Isothermal-Isobaric Ensemble. *The Journal of Chemical Physics*, 48:415, 1968.

[3] G. E. Norman and V. S. Filinov. Investigations of phase transitions by a Monte Carlo method. *High Temp. (USSR)*, 7:216, 1969.

[4] M. Mezei. Virial-bias Monte Carlo methods. *Molecular Physics*, 48:1075, 1983.

[5] P. Jedlovszky and M. Mezei. The anisotropic virial-biased sampling for Monte Carlo simulations in the isothermal-isobaric ensemble. *Molecular Physics*, 96:293, 1999.

[6] S. Duane, A. Kennedy, B. J. Pendleton, and D. Roweth. Hybrid Monte Carlo. *Physics Letters B*, 195:216, 1987.

[7] B. Mehlig, D. W. Heermann, and B. M. Forrest. Hybrid Monte Carlo method for condensed-matter systems. *Physical Review B*, 45:679, 1992.

[8] G. M. Torrie and J. P. Valleau. Monte Carlo study of a phase-separating liquid mixture by umbrella sampling. *The Journal of Chemical Physics*, 66:1402, 1977.

[9] G. M. Torrie and J. P. Valleau. Nonphysical sampling distributions in Monte Carlo free-energy estimation: Umbrella sampling. *Journal of Computational Physics*, 23:187, 1977.

[10] A. P. Lyubartsev, A. A. Martsinovski, S. V. Shevkunov, and P. N. Vorontsov-Velyaminov. New approach to Monte Carlo calculation of the free energy: Method of expanded ensembles. *The Journal of Chemical Physics*, 96:1776, 1992.

[11] C. J. Geyer and E. A. Thompson. Annealing Markov chain Monte Carlo with applications to ancestral inference. page 909, 1995.

[12] K. Hukushima, H. Takayama, and K. Nemoto. Application of an extended ensemble method to spin glasses. *International Journal of Modern Physics C*, 07:337, 1996.

[13] B. A. Berg and T. Neuhaus. Multicanonical ensemble: A new approach to simulate first-order phase transitions. *Physical Review Letters*, 68:9, 1992.

[14] B. A. Berg. Multicanonical Monte Carlo simulations. *International Journal of Modern Physics C*, 4:249, 1993.

[15] J.-S. Wang, T. K. Tay, and R. H. Swendsen. Transition Matrix Monte Carlo Reweighting and Dynamics. *Physical Review Letters*, 82:476, 1999.

[16] J.-S. Wang and R. H. Swendsen. Transition Matrix Monte Carlo Method. *Journal of Statistical Physics*, 106:245, 2002.

[17] A. Z. Panagiotopoulos. Direct determination of phase coexistence properties of fluids by Monte Carlo simulation in a new ensemble. *Molecular Physics*, 61:813, 1987.

[18] A. Panagiotopoulos, N. Quirke, M. Stapleton, and D. Tildesley. Phase equilibria by simulation in the Gibbs ensemble. *Molecular Physics*, 63:527, 1988.

[19] N. B. Wilding and A. D. Bruce. Freezing by Monte Carlo Phase Switch. *Physical Review Letters*, 85:5138, 2000.

[20] J. E. Lennard-Jones. On the Determination of Molecular Fields. II. From the Equation of State of a Gas. *Proceedings of the Royal Society of London. Series A*, 106:463, 1924.

[21] D. N. J. White. A computationally efficient alternative to the Buckingham potential for molecular mechanics calculations. *Journal of Computer-Aided Molecular Design*, 11:517, 1997.

[22] A. Warshel and S. Lifson. Consistent Force Field Calculations. II. Crystal Structures, Sublimation Energies, Molecular and Lattice Vibrations, Molecular Conformations, and Enthalpies of Alkanes. *Journal of Chemical Physics*, 53:582, 1970.

[23] J. J. Potoff and D. A. Bernard-Brunel. Mie Potentials for Phase Equilibria Calculations: Application to Alkanes and Perfluoroalkanes. *The Journal of Physical Chemistry B*, 113:14725, 2009.

[24] H. Meyer, O. Biermann, R. Faller, D. Reith, and F. Muller-Plathe. Coarse graining of nonbonded inter-particle potentials using automatic simplex optimization to fit structural properties. *The Journal of Chemical Physics*, 113:6264, 2000.

[25] K. A. Maerzke and J. I. Siepmann. Transferable Potentials for Phase Equilibria-Coarse-Grain Description for Linear Alkanes. *The Journal of Physical Chemistry B*, 115:3452, 2011.

[26] A. Ahmed and R. J. Sadus. Effect of potential truncations and shifts on the solid-liquid phase coexistence of Lennard-Jones fluids. *The Journal of Chemical Physics*, 133:124515, 2010.

[27] S. A. Khrapak, M. Chaudhuri, and G. E. Morfill. Freezing of Lennard-Jones-type fluids. *The Journal of Chemical Physics*, 134:054120, 2011.

[28] H. W. Kroto, J. R. Heath, S. C. O'Brien, R. F. Curl, and R. E. Smalley. C_{60}: Buckminsterfullerene. *Nature*, 318:162, 1985.

[29] B. Sundqvist. Fullerenes under high pressures. *Advances in Physics*, 48:1, 1999.

[30] T. Lee. *Monte Carlo Simulations of Structural Phase Transitions in Metals and Alloys*. PhD thesis, Brown University, 2010.

[31] K. M. Thomas. Hydrogen adsorption and storage on porous materials. *Catalysis Today*, 120:389, 2007.

[32] K. M. Thomas. Adsorption and desorption of hydrogen on metal–organic framework materials for storage applications: comparison with other nanoporous materials. *Dalton Transactions*, page 1487, 2009.

[33] J. Yang, A. Sudik, C. Wolverton, and D. J. Siegel. High capacity hydrogen storage materials: attributes for automotive applications and techniques for materials discovery. *Chemical Society Reviews*, 39:656, 2010.

[34] D. W. Breck. *Zeolite molecular sieves: structure, chemistry, and use*. Wiley, New York, 1973.

[35] E. Flanigen, J. Jansen, and H. v. Bekkum. *Introduction to Zeolite Science and Practice*. Elsevier Science, 1991.

[36] J. W. Gibbs. *Elementary principles in statistical mechanics developed with especial reference to the rational foundation of thermodynamics*. C. Scribner,, New York :, 1902.

[37] J.-P. Hansen and I. R. McDonald. *Theory of simple liquids*. Academic Press, 2006.

[38] D. Frenkel and B. Smit. *Understanding molecular simulation: from algorithms to applications*. Academic Press, 2002.

[39] M. E. J. Newman and G. T. Barkema. *Monte Carlo methods in statistical physics*. Clarendon Press, Oxford, 1999.

[40] V. I. Manousiouthakis and M. W. Deem. Strict detailed balance is unnecessary in Monte Carlo simulation. *The Journal of Chemical Physics*, 110:2753, 1999.

[41] M. P. Allen and D. J. Tildesley. *Computer simulation of liquids.* Oxford science publications. Clarendon Press, Oxford, 1989.

[42] I. McDonald. *NpT*-ensemble Monte Carlo calculations for binary liquid mixtures. *Molecular Physics*, 23:41, 1972.

[43] A. L. Ferreira and M. A. Barroso. Temperature and density extrapolations in canonical ensemble Monte Carlo simulations. *Physical Review E*, 61:1195, 2000.

[44] M. Parrinello and A. Rahman. Crystal Structure and Pair Potentials: A Molecular-Dynamics Study. *Physical Review Letters*, 45:14, 1980.

[45] M. Parrinello and A. Rahman. Polymorphic transitions in single crystals: A new molecular dynamics method. *Journal of Applied Physics*, 52:7182, 1981.

[46] H. C. Andersen. Molecular dynamics simulations at constant pressure and/or temperature. *The Journal of Chemical Physics*, 72:2384, 1980.

[47] I. Souza and J. L. Martins. Metric tensor as the dynamical variable for variable-cell-shape molecular dynamics. *Physical Review B*, 55:8733, 1997.

[48] A. H. Fuchs and A. K. Cheetham. Adsorption of Guest Molecules in Zeolitic Materials: Computational Aspects. *The Journal of Physical Chemistry B*, 105:7375, 2001.

[49] D. P. Landau and K. Binder. *A guide to Monte Carlo simulations in statistical physics.* Cambridge University Press, 2005.

[50] P. P. Ewald. Die Berechnung optischer und elektrostatischer Gitterpotentiale. *Annalen der Physik*, 369:253, 1921.

[51] S. W. de Leeuw, J. W. Perram, and E. R. Smith. Simulation of Electrostatic Systems in Periodic Boundary Conditions. I. Lattice Sums and Dielectric Constants. *Proceedings of the Royal Society of London. Series A*, 373:27, 1980.

[52] S. W. de Leeuw, J. W. Perram, and E. R. Smith. Simulation of Electrostatic Systems in Periodic Boundary Conditions. II. Equivalence of Boundary Conditions. *Proceedings of the Royal Society of London. Series A*, 373:57, 1980.

[53] S. W. de Leeuw, J. W. Perram, and E. R. Smith. Simulation of Electrostatic Systems in Periodic Boundary Conditions. III. Further Theory and Applications. *Proceedings of the Royal Society of London. Series A*, 388:177, 1983.

[54] T. M. Nymand and P. Linse. Ewald summation and reaction field methods for potentials with atomic charges, dipoles, and polarizabilities. *The Journal of Chemical Physics*, 112:6152, 2000.

[55] A. W. Appel. An Efficient Program for Many-Body Simulation. *SIAM Journal on Scientific and Statistical Computing*, 6:85, 1985.

[56] L. Greengard and V. Rokhlin. A fast algorithm for particle simulations. *Journal of Computational Physics*, 73:325, 1987.

[57] R. Hockney and J. Eastwood. *Computer Simulation Using Particles.* Taylor & Francis, 1989.

[58] T. Möller, E. Haines, and N. Hoffmann. *Real-time rendering.* A.K. Peters, Wellesley, Mass., 2008.

[59] D. C. Rapaport. *The Art of Molecular Dynamics Simulation.* Cambridge University Press, 2004.

[60] V. Franz J. Angular Monte Carlo integration using quaternion parameters: a spherical reference potential for CCl4. *Journal of Computational Physics*, 47:291, 1982.

[61] K. Binder, B. Block, S. K. Das, P. Virnau, and D. Winter. Monte Carlo Methods for Estimating Interfacial Free Energies and Line Tensions. *Journal of Statistical Physics*, 144:690, 2011.

[62] M. Schrader, P. Virnau, and K. Binder. Simulation of vapor-liquid coexistence in finite volumes: A method to compute the surface free energy of droplets. *Physical Review E*, 79, 2009.

[63] A. Z. Panagiotopoulos. Monte Carlo methods for phase equilibria of fluids. *Journal of Physics: Condensed Matter*, 12:R25, 2000.

[64] C. Vega, E. Sanz, J. L. F. Abascal, and E. G. Noya. Determination of phase diagrams via computer simulation: methodology and applications to water, electrolytes and proteins. *Journal of Physics: Condensed Matter*, 20:153101, 2008.

[65] J. M. G. Sousa, A. L. Ferreira, and M. A. Barroso. Determination of the solid-fluid coexistence of the n - 6 Lennard-Jones system from free energy calculations. *The Journal of Chemical Physics*, 136:174502, 2012.

[66] A. M. Ferrenberg and R. H. Swendsen. New Monte Carlo technique for studying phase transitions. *Physical Review Letters*, 61:2635, 1988.

[67] A. M. Ferrenberg and R. H. Swendsen. Optimized Monte Carlo data analysis. *Physical Review Letters*, 63:1195, 1989.

[68] M. Barroso. *Estudos de Monte Carlo de diagramas de fase: aplicação ao C_{60} e ao modelo de Lennard-Jones.* PhD thesis, Universidade de Aveiro, 2007.

[69] T. Kihara. Virial Coefficients and Models of Molecules in Gases. *Reviews of Modern Physics*, 25:831, 1953.

[70] J. A. Barker. Fifth Virial Coefficients. *The Journal of Chemical Physics*, 44:4206, 1966.

[71] J. A. Barker and J. J. Monaghan. Fourth Virial Coefficients for the 12–6 Potential. *The Journal of Chemical Physics*, 36:2564, 1962.

[72] T. Sun and A. S. Teja. An Equation of State for Real Fluids Based on the Lennard-Jones Potential. *The Journal of Physical Chemistry*, 100:17365, 1996.

[73] N. Clisby and B. M. McCoy. Ninth and Tenth Order Virial Coefficients for Hard Spheres in D Dimensions. *Journal of Statistical Physics*, 122:15, 2006.

[74] A. Y. Vlasov, X.-M. You, and A. J. Masters. Monte-Carlo integration for virial coefficients re-visited: hard convex bodies, spheres with a square-well potential and mixtures of hard spheres. *Molecular Physics*, 100:3313, 2002.

[75] T. B. Tan, A. J. Schultz, and D. A. Kofke. Virial coefficients, equation of state, and solid–fluid coexistence for the soft sphere model. *Molecular Physics*, 109:123, 2010.

[76] R. J. Wheatley. Calculation of High-Order Virial Coefficients with Applications to Hard and Soft Spheres. *Physical Review Letters*, 110:200601, 2013.

[77] J. K. Singh and D. A. Kofke. Mayer Sampling: Calculation of Cluster Integrals using Free-Energy Perturbation Methods. *Physical Review Letters*, 92:220601, 2004.

[78] J. K. Singh and D. A. Kofke. Erratum: Mayer Sampling: Calculation of Cluster Integrals Using Free-Energy Perturbation Methods [Phys. Rev. Lett. 92, 220601 (2004)]. *Physical Review Letters*, 95:249903, 2005.

[79] A. J. Schultz and D. A. Kofke. Sixth, seventh and eighth virial coefficients of the Lennard-Jones model. *Molecular Physics*, 107:2309, 2009.

[80] B. Widom. Some Topics in the Theory of Fluids. *The Journal of Chemical Physics*, 39:2808, 1963.

[81] W. G. Hoover and F. H. Ree. Melting Transition and Communal Entropy for Hard Spheres. *The Journal of Chemical Physics*, 49:3609, 1968.

[82] D. Frenkel and A. J. C. Ladd. New Monte Carlo method to compute the free energy of arbitrary solids. Application to the fcc and hcp phases of hard spheres. *The Journal of Chemical Physics*, 81:3188, 1984.

[83] J. Chang and S. I. Sandler. Determination of liquid–solid transition using histogram reweighting method and expanded ensemble simulations. *The Journal of Chemical Physics*, 118:8390, 2003.

[84] J. M. Polson, E. Trizac, S. Pronk, and D. Frenkel. Finite-size corrections to the free energies of crystalline solids. *The Journal of Chemical Physics*, 112:5339, 2000.

[85] W. G. Hoover. Entropy for Small Classical Crystals. *The Journal of Chemical Physics*, 49:1981, 1968.

[86] A. Z. Panagiotopoulos. Direct Determination of Fluid Phase Equilibria by Simulation in the Gibbs Ensemble: A Review. *Molecular Simulation*, 9:1, 1992.

[87] A. D. Bruce, N. B. Wilding, and G. J. Ackland. Free Energy of Crystalline Solids: A Lattice-Switch Monte Carlo Method. *Physical Review Letters*, 79:3002, 1997.

[88] A. D. Bruce, A. N. Jackson, G. J. Ackland, and N. B. Wilding. Lattice-switch Monte Carlo method. *Physical Review E*, 61:906, 2000.

[89] A. N. Jackson, A. D. Bruce, and G. J. Ackland. Lattice-switch Monte Carlo method: Application to soft potentials. *Physical Review E*, 65:036710, 2002.

[90] J. R. Errington. Solid–liquid phase coexistence of the Lennard-Jones system through phase-switch Monte Carlo simulation. *The Journal of Chemical Physics*, 120:3130, 2004.

[91] G. Grochola. Constrained fluid λ-integration: Constructing a reversible thermodynamic path between the solid and liquid state. *The Journal of Chemical Physics*, 120:2122, 2004.

[92] G. Grochola, I. K. Snook, and S. P. Russo. Application of the constrained fluid λ-integration path to the calculation of high temperature Au(110) surface free energies. *The Journal of Chemical Physics*, 122:064711, 2005.

[93] D. A. Kofke. Gibbs-Duhem integration: a new method for direct evaluation of phase coexistence by molecular simulation. *Molecular Physics*, 78:1331, 1993.

[94] D. A. Kofke. Direct evaluation of phase coexistence by molecular simulation via integration along the saturation line. *The Journal of Chemical Physics*, 98:4149, 1993.

[95] R. Agrawal and D. A. Kofke. Solid-Fluid Coexistence for Inverse-Power Potentials. *Physical Review Letters*, 74:122, 1995.

[96] R. Agrawal and D. Kofke. Thermodynamic and structural properties of model systems at solid-fluid coexistence. *Molecular Physics*, 85:43, 1995.

[97] D. Möller and J. Fischer. Vapour liquid equilibrium of a pure fluid from test particle method in combination with NpT molecular dynamics simulations. *Molecular Physics*, 69:463, 1990.

[98] D. Möller and J. Fischer. Erratum: Vapour liquid equilibrium of a pure fluid from test particle method in combination with NpT molecular dynamics simulations [Mol. Phys. 69, 463 (1990)]. *Molecular Physics*, 75:1461, 1992.

[99] N. B. Wilding. Critical-point and coexistence-curve properties of the Lennard-Jones fluid: A finite-size scaling study. *Physical Review E*, 52:602, 1995.

[100] F. Wang and D. P. Landau. Efficient, Multiple-Range Random Walk Algorithm to Calculate the Density of States. *Physical Review Letters*, 86:2050, 2001.

[101] E. A. Mastny and J. J. de Pablo. Direct calculation of solid-liquid equilibria from density-of-states Monte Carlo simulations. *The Journal of Chemical Physics*, 122:124109, 2005.

[102] J. R. Errington. Direct calculation of liquid–vapor phase equilibria from transition matrix Monte Carlo simulation. *The Journal of Chemical Physics*, 118:9915, 2003.

[103] A. J. C. Ladd and L. V. Woodcock. Triple-point coexistence properties of the lennard-jones system. *Chemical Physics Letters*, 51:155, 1977.

[104] J. R. Morris and X. Song. The melting lines of model systems calculated from coexistence simulations. *The Journal of Chemical Physics*, 116:9352, 2002.

[105] U. R. Pedersen, F. Hummel, G. Kresse, G. Kahl, and C. Dellago. Computing Gibbs free energy differences by interface pinning. *Physical Review B*, 88:094101, 2013.

[106] A. Lotfi, J. Vrabec, and J. Fischer. Vapour liquid equilibria of the Lennard-Jones fluid from the NpT plus test particle method. *Molecular Physics*, 76:1319, 1992.

[107] K. Kiyohara. Thermodynamic scaling Gibbs ensemble Monte Carlo: a new method for determination of phase coexistence properties of fluids. *Molecular Physics*, 89:965, 1996.

[108] A. Z. Panagiotopoulos. On the equivalence of continuum and lattice models for fluids. *The Journal of Chemical Physics*, 112:7132, 2000.

[109] H. Okumura and F. Yonezawa. Liquid–vapor coexistence curves of several interatomic model potentials. *The Journal of Chemical Physics*, 113:9162, 2000.

[110] I. Charpentier and N. Jakse. Phase diagram of complex fluids using an efficient integral equation method. *The Journal of Chemical Physics*, 123:204910, 2005.

[111] G. C. McNeil-Watson and N. B. Wilding. Freezing line of the Lennard-Jones fluid: A phase switch Monte Carlo study. *The Journal of Chemical Physics*, 124:064504, 2006.

[112] U. R. Pedersen. Direct calculation of the solid-liquid Gibbs free energy difference in a single equilibrium simulation. *The Journal of Chemical Physics*, 139:104102, 2013.

[113] J. Ge, G.-W. Wu, B. D. Todd, and R. J. Sadus. Equilibrium and nonequilibrium molecular dynamics methods for determining solid–liquid phase coexistence at equilibrium. *The Journal of Chemical Physics*, 119:11017, 2003.

[114] A. Ahmed and R. J. Sadus. Solid-liquid equilibria and triple points of n-6 Lennard-Jones fluids. *The Journal of Chemical Physics*, 131:174504, 2009.

[115] A. Ahmed and R. J. Sadus. Erratum: Solid–liquid equilibria and triple points of n-6 Lennard-Jones fluids [J. Chem. Phys. 131, 174504 (2009)]. *The Journal of Chemical Physics*, 133:229902, 2010.

[116] M. A. Barroso and A. L. Ferreira. Solid–fluid coexistence of the Lennard-Jones system from absolute free energy calculations. *The Journal of Chemical Physics*, 116:7145, 2002.

[117] A. L. C. Ferreira, J. M. Pacheco, and J. P. Prates-Ramalho. Phase diagram of C_{60} from ab initio intermolecular potential. *The Journal of Chemical Physics*, 113:738, 2000.

[118] F. H. Stillinger. Lattice sums and their phase diagram implications for the classical Lennard-Jones model. *The Journal of Chemical Physics*, 115:5208, 2001.

[119] M. A. van der Hoef. Free energy of the Lennard-Jones solid. *The Journal of Chemical Physics*, 113:8142, 2000.

[120] E. A. Mastny and J. J. de Pablo. Melting line of the Lennard-Jones system, infinite size, and full potential. *The Journal of Chemical Physics*, 127:104504, 2007.

[121] S. A. Khrapak, M. Chaudhuri, and G. E. Morfill. Liquid-solid phase transition in the Lennard-Jones system. *Physical Review B*, 82:052101, 2010.

[122] S. Prestipino, F. Saija, and P. V. Giaquinta. Phase diagram of softly repulsive systems: The Gaussian and inverse-power-law potentials. *The Journal of Chemical Physics*, 123:144110, 2005.

[123] T. B. Tan, A. J. Schultz, and D. A. Kofke. Efficient calculation of temperature dependence of solid-phase free energies by overlap sampling coupled with harmonically targeted perturbation. *The Journal of Chemical Physics*, 133:134104, 2010.

[124] S. A. Khrapak and G. E. Morfill. fcc-bcc-fluid triple point for model pair interactions with variable softness. *EPL (Europhysics Letters)*, 100:66004, 2012.

[125] H. W. Kroto. The stability of the fullerenes C_n, with $n = 24, 28, 32, 36, 50, 60$ and 70. *Nature*, 329:529, 1987.

[126] M. S. Dresselhaus, G. Dresselhaus, and P. C. Eklund. *Science of Fullerenes and Carbon Nanotubes: Their Properties and Applications*. Academic Press, 1996.

[127] K. Hedberg, L. Hedberg, D. S. Bethune, C. A. Brown, H. C. Dorn, R. D. Johnson, and M. D. Vries. Bond Lengths in Free Molecules of Buckminsterfullerene, C_{60}, from Gas-Phase Electron Diffraction. *Science*, 254:410, 1991.

[128] P. A. Heiney, J. E. Fischer, A. R. McGhie, W. J. Romanow, A. M. Denenstein, J. P. McCauley Jr., A. B. Smith, and D. E. Cox. Orientational ordering transition in solid C_{60}. *Physical Review Letters*, 66:2911, 1991.

[129] R. Moret, S. Ravy, and J.-M. Godard. X-ray diffuse scattering study of the orientational ordering in single crystal C_{60}. *Journal de Physique I*, 2:1699, 1992.

[130] W. I. F. David, R. M. Ibberson, T. J. S. Dennis, J. P. Hare, and K. Prassides. Structural Phase Transitions in the Fullerene C_{60}. *Europhysics Letters (EPL)*, 18:219, 1992.

[131] W. I. F. David, R. M. Ibberson, and T. Matsuo. High Resolution Neutron Powder Diffraction: A Case Study of the Structure of C_{60}. *Proceedings of the Royal Society of London. Series A*, 442:129, 1993.

[132] W. I. F. David, R. M. Ibberson, J. C. Matthewman, K. Prassides, T. J. S. Dennis, J. P. Hare, H. W. Kroto, R. Taylor, and D. R. M. Walton. Crystal structure and bonding of ordered C_{60}. *Nature*, 353:147, 1991.

[133] P. C. Chow, X. Jiang, G. Reiter, P. Wochner, S. C. Moss, J. D. Axe, J. C. Hanson, R. K. McMullan, R. L. Meng, and C. W. Chu. Synchrotron x-ray study of orientational order in single crystal C_{60} at room temperature. *Physical Review Letters*, 69:2943, 1992.

[134] K. Prassides, H. Kroto, R. Taylor, D. Walton, W. David, J. Tomkinson, R. Haddon, M. Rosseinsky, and D. Murphy. Fullerenes and fullerides in the solid state: Neutron scattering studies. *Carbon*, 30:1277, 1992.

[135] W. I. F. David and R. M. Ibberson. High-pressure, low-temperature structural studies of orientationally ordered C_{60}. *Journal of Physics: Condensed Matter*, 5:7923, 1993.

[136] R. D. Johnson, C. S. Yannoni, H. C. Dorn, J. R. Salem, and D. S. Bethune. C_{60} Rotation in the Solid State: Dynamics of a Faceted Spherical Top. *Science*, 255:1235, 1992.

[137] T. Matsuo, H. Suga, W. David, R. Ibberson, P. Bernier, A. Zahab, C. Fabre, A. Rassat, and A. Dworkin. The heat capacity of solid C_{60}. *Solid State Communications*, 83:711, 1992.

[138] F. Gugenberger, R. Heid, C. Meingast, P. Adelmann, M. Braun, H. Wühl, M. Haluska, and H. Kuzmany. Glass transition in single-crystal C_{60} studied by high-resolution dilatometry. *Physical Review Letters*, 69:3774, 1992.

[139] R. C. Yu, N. Tea, M. B. Salamon, D. Lorents, and R. Malhotra. Thermal conductivity of single crystal C_{60}. *Physical Review Letters*, 68:2050, 1992.

[140] R. Tycko, G. Dabbagh, R. M. Fleming, R. C. Haddon, A. V. Makhija, and S. M. Zahurak. Molecular dynamics and the phase transition in solid C_{60}. *Physical Review Letters*, 67:1886, 1991.

[141] M. H. J. Hagen, E. J. Meijer, G. C. a. M. Mooij, D. Frenkel, and H. N. W. Lekkerkerker. Does C_{60} have a liquid phase? *Nature*, 365:425, 1993.

[142] A. Cheng, M. L. Klein, and C. Caccamo. Prediction of the phase diagram of rigid C_{60} molecules. *Physical Review Letters*, 71:1200, 1993.

[143] N. W. Ashcroft. Elusive diffusive liquids. *Nature*, 365:387, 1993.

[144] C. Rascón, G. Navascués, and L. Mederos. Phase transitions in systems with extremely short-ranged attractions: A density-functional theory. *Physical Review B*, 51:14899, 1995.

[145] G. A. Vliegenthart and H. N. W. Lekkerkerker. Predicting the gas–liquid critical point from the second virial coefficient. *The Journal of Chemical Physics*, 112:5364, 2000.

[146] C. Caccamo. Modified-hypernetted-chain determination of the phase diagram of rigid C_{60} molecules. *Physical Review B*, 51:3387, 1995.

[147] M. Hasegawa and K. Ohno. Monte Carlo simulation study of the high-temperature phase diagram of model C_{60} molecules. *The Journal of Chemical Physics*, 111:5955, 1999.

[148] D. Costa, G. Pellicane, M. C. Abramo, and C. Caccamo. Free energy determination of phase coexistence in model C_{60}: A comprehensive Monte Carlo study. *The Journal of Chemical Physics*, 118:304, 2003.

[149] L. J. Gallego, J. García-Rodeja, M. M. G. Alemany, and C. Rey. Solidlike-to-Liquidlike Transition in Small Clusters of C_{60} Molecules or Transition-Metal Atoms. *Physical Review Letters*, 83:5258, 1999.

[150] A. Piatek, A. Dawid, and Z. Gburski. The existence of a plastic phase and a solid–liquid dynamical bistability region in small fullerene cluster $(C_{60})_7$: molecular dynamics simulation. *Journal of Physics: Condensed Matter*, 18:8471, 2006.

[151] B. Sundqvist. Polymeric Fullerene Phases Formed Under Pressure. In K. Prassides, editor, *Fullerene-Based Materials*, volume 109 of *Structure & Bonding*, page 85. Springer Berlin / Heidelberg, 2004.

[152] R. Moret. Structures, phase transitions and orientational properties of the C_{60} monomer and polymers. *Acta Crystallographica Section A*, 61:62–76, 2005.

[153] A. M. Rao, P. Zhou, K.-A. Wang, G. T. Hager, J. M. Holden, Y. Wang, W.-T. Lee, X.-X. Bi, P. C. Eklund, D. S. Cornett, M. A. Duncan, and I. J. Amster. Photoinduced Polymerization of Solid C_{60} Films. *Science*, 259:955, 1993.

[154] M. Núñez-Regueiro, L. Marques, J. L. Hodeau, O. Béthoux, and M. Perroux. Polymerized Fullerite Structures. *Physical Review Letters*, 74:278, 1995.

[155] L. Marques, J. L. Hodeau, M. Núñez-Regueiro, and M. Perroux. Pressure and temperature diagram of polymerized fullerite. *Physical Review B*, 54:R12633, 1996.

[156] L. Marques, M. Mezouar, J.-L. Hodeau, M. Núñez-Regueiro, N. R. Serebryanaya, V. A. Ivdenko, V. D. Blank, and G. A. Dubitsky. "Debye-Scherrer Ellipses" from 3D Fullerene Polymers: An Anisotropic Pressure Memory Signature. *Science*, 283:1720, 1999.

[157] Burgos, Halac, Weht, Bonadeo, Artacho, and Ordejon. New superhard phases for three-dimensional C_{60}-based fullerites. *Physical review letters*, 85:2328, 2000.

[158] V. Blank, S. Buga, G. Dubitsky, N. Serebryanaya, M. Popov, and V. Prokhorov. Properties and Applications of Superhard and Ultrahard Fullerites. In E. Ōsawa, editor, *Perspectives of Fullerene Nanotechnology*, page 223. Springer Netherlands, 2002.

[159] A. Cheng and M. L. Klein. Molecular dynamics simulations of solid buckminsterfullerenes. *The Journal of Physical Chemistry*, 95:6750, 1991.

[160] A. Cheng and M. L. Klein. Molecular-dynamics investigation of orientational freezing in solid C_{60}. *Physical Review B*, 45:1889, 1992.

[161] Y. Quo, N. Karasawa, and W. A. Goddard. Prediction of fullerene packing in C_{60} and C_{70} crystals. *Nature*, 351:464, 1991.

[162] M. Sprik, A. Cheng, and M. L. Klein. Modeling the orientational ordering transition in solid fullerene (C_{60}). *The Journal of Physical Chemistry*, 96:2027, 1992.

[163] J. Chang and S. I. Sandler. Free energy of the solid C_{60} fullerene orientational order-disorder transition. *The Journal of Chemical Physics*, 125:054705, 2006.

[164] J. P. Lu, X.-P. Li, and R. M. Martin. Ground state and phase transitions in solid C_{60}. *Physical Review Letters*, 68:1551, 1992.

[165] E. Burgos, E. Halac, and H. Bonadeo. Intermolecular forces and phase transitions in solid C_{60}. *Physical Review B*, 49:15544, 1994.

[166] L. Pintschovius and S. L. Chaplot. Neutron scattering study of the intermolecular vibrations in solid C_{60}. *Zeitschrift für Physik B Condensed Matter*, 98:527, 1995.

[167] D. Lamoen and K. H. Michel. Crystal field, orientational order, and lattice contraction in solid C_{60}. *The Journal of Chemical Physics*, 101:1435, 1994.

[168] Y. Kita and I. Okada. Molecular dynamics calculations of solid C_{60} under high pressure. *Molecular Simulation*, 33:165, 2007.

[169] S. Savin, A. B. Harris, and T. Yildirim. Towards a microscopic approach to the intermolecular interaction in solid C_{60}. *Physical Review B*, 55:14182, 1997.

[170] J. M. Pacheco and J. P. Prates Ramalho. First-Principles Determination of the Dispersion Interaction between Fullerenes and Their Intermolecular Potential. *Physical Review Letters*, 79:3873, 1997.

[171] K.-P. Bohnen and R. Heid. Ab Initio Intermolecular Potential of Solid C_{60} in the Low-Temperature Phase. *Physical Review Letters*, 83:1167, 1999.

[172] M. Hasegawa, K. Nishidate, M. Katayama, and T. Inaoka. Intermolecular potential and the equation of state of solid C_{60}. *The Journal of Chemical Physics*, 119:1386, 2003.

[173] L. A. Girifalco. Molecular properties of fullerene in the gas and solid phases. *The Journal of Physical Chemistry*, 96:858, 1992.

[174] P. Hoffmann. *Tomorrow's Energy: Hydrogen, Fuel Cells, and the Prospects for a Cleaner Planet.* MIT Press, Cambridge, Mass., 2002.

[175] M. Felderhoff, C. Weidenthaler, R. v. Helmolt, and U. Eberle. Hydrogen storage: the remaining scientific and technological challenges. *Physical Chemistry Chemical Physics*, 9:2643, 2007.

[176] H. W. Langmi, A. Walton, M. M. Al-Mamouri, S. R. Johnson, D. Book, J. D. Speight, P. P. Edwards, I. Gameson, P. A. Anderson, and I. R. Harris. Hydrogen adsorption in zeolites A, X, Y and RHO. *Journal of Alloys and Compounds*, 356-357:710, 2003.

[177] J. G. Vitillo, G. Ricchiardi, G. Spoto, and A. Zecchina. Theoretical maximal storage of hydrogen in zeolitic frameworks. *Physical Chemistry Chemical Physics*, 7:3948, 2005.

[178] M. Nijkamp, J. Raaymakers, A. van Dillen, and K. de Jong. Hydrogen storage using physisorption – materials demands. *Applied Physics A Materials Science & Processing*, 72:619, 2001.

[179] S. B. Kayiran and F. L. Darkrim. Synthesis and ionic exchanges of zeolites for gas adsorption. *Surface and Interface Analysis*, 34:100, 2002.

[180] H. Langmi, D. Book, A. Walton, S. Johnson, M. Al-Mamouri, J. Speight, P. Edwards, I. Harris, and P. Anderson. Hydrogen storage in ion-exchanged zeolites. *Journal of Alloys and Compounds*, 404-406:637, 2005.

[181] X.-m. Du and E.-d. Wu. Physisorption of Hydrogen in A, X and ZSM-5 Types of Zeolites at Moderately High Pressures. *Chinese Journal of Chemical Physics*, 19:457, 2006.

[182] J. Dong, X. Wang, H. Xu, Q. Zhao, and J. Li. Hydrogen storage in several microporous zeolites. *International Journal of Hydrogen Energy*, 32:4998, 2007.

[183] B. Smit and T. L. M. Maesen. Molecular Simulations of Zeolites: Adsorption, Diffusion, and Shape Selectivity. *Chemical Reviews*, 108:4125, 2008.

[184] C.-R. Anderson, D. F. Coker, J. Eckert, and A. L. R. Bug. Computational study of molecular hydrogen in zeolite Na-A. I. Potential energy surfaces and thermodynamic separation factors for ortho and para hydrogen. *The Journal of Chemical Physics*, 111:7599, 1999.

[185] J. A. MacKinnon, J. Eckert, D. F. Coker, and A. L. R. Bug. Computational study of molecular hydrogen in zeolite Na–A. II. Density of rotational states and inelastic neutron scattering spectra. *The Journal of Chemical Physics*, 114:10137, 2001.

[186] F. Darkrim, A. Aoufi, P. Malbrunot, and D. Levesque. Hydrogen adsorption in the NaA zeolite: A comparison between numerical simulations and experiments. *The Journal of Chemical Physics*, 112:5991, 2000.

[187] E. D. Akten, R. Siriwardane, and D. S. Sholl. Monte Carlo Simulation of Single- and Binary-Component Adsorption of CO_2, N_2, and H_2 in Zeolite Na-4A. *Energy & Fuels*, 17:977, 2003.

[188] M. K. Song and K. T. No. Molecular simulation of hydrogen adsorption in organic zeolite. *Catalysis Today*, 120:374, 2007.

[189] M. K. Song and K. T. No. Grand Canonical Monte Carlo simulations of hydrogen adsorption on aluminophosphate molecular sieves. *International Journal of Hydrogen Energy*, 34:2325, 2009.

[190] M. Rahmati and H. Modarress. Grand canonical Monte Carlo simulation of isotherm for hydrogen adsorption on nanoporous siliceous zeolites at room temperature. *Applied Surface Science*, 255:4773, 2009.

[191] J. M. Sousa, A. L. Ferreira, D. P. Fagg, E. Titus, R. Krishna, and J. Gracio. Temperature Dependence of the Henry's Law Constant for Hydrogen Storage in NaA Zeolites: A Monte Carlo Simulation Study. *Journal of Nanoscience and Nanotechnology*, 12:6785, 2012.

[192] K. Watanabe, N. Austin, and M. R. Stapleton. Investigation of the Air Separation Properties of Zeolites Types A, X and Y by Monte Carlo Simulations. *Molecular Simulation*, 15:197, 1995.

[193] O. Talu and A. L. Myers. Reference potentials for adsorption of helium, argon, methane, and krypton in high-silica zeolites. *Colloids and Surfaces A: Physicochemical and Engineering Aspects*, 187-188:83, 2001.

[194] L.-C. Lin, A. H. Berger, R. L. Martin, J. Kim, J. A. Swisher, K. Jariwala, C. H. Rycroft, A. S. Bhown, M. W. Deem, M. Haranczyk, and B. Smit. In silico screening of carbon-capture materials. *Nature Materials*, 11:633, 2012.

[195] D. M. Ruthven. *Principles of adsorption and adsorption processes*. Wiley, New York, 1984.

[196] A. L. Myers and P. A. Monson. Adsorption in Porous Materials at High Pressure: Theory and Experiment. *Langmuir*, 18:10261, 2002.

[197] O. Talu and A. L. Myers. Molecular simulation of adsorption: Gibbs dividing surface and comparison with experiment. *AIChE Journal*, 47:1160, 2001.

[198] P. Malbrunot, D. Vidal, J. Vermesse, R. Chahine, and T. K. Bose. Adsorbent Helium Density Measurement and Its Effect on Adsorption Isotherms at High Pressure. *Langmuir*, 13:539, 1997.

[199] J. J. Pluth and J. V. Smith. Accurate redetermination of crystal structure of dehydrated zeolite A. Absence of near zero coordination of sodium. Refinement of silicon,aluminum-ordered superstructure. *Journal of the American Chemical Society*, 102:4704, 1980.

[200] D. A. Faux, W. Smith, and T. R. Forester. Molecular Dynamics Studies of Hydrated and Dehydrated Na+-Zeolite-4A. *The Journal of Physical Chemistry B*, 101:1762, 1997.

[201] D. A. Faux. Molecular Dynamics Studies of Sodium Diffusion in Hydrated Na+-Zeolite-4A. *The Journal of Physical Chemistry B*, 102:10658, 1998.

[202] P. Demontis and G. B. Suffritti. Structure and Dynamics of Zeolites Investigated by Molecular Dynamics. *Chemical Reviews*, 97:2845, 1997.

[203] A. V. Kiselev, A. A. Lopatkin, and A. A. Shulga. Molecular statistical calculation of gas adsorption by silicalite. *Zeolites*, 5:261, 1985.

[204] W. J. Mortier, S. K. Ghosh, and S. Shankar. Electronegativity-equalization method for the calculation of atomic charges in molecules. *Journal of the American Chemical Society*, 108:4315, 1986.

[205] F. Darkrim and D. Levesque. High Adsorptive Property of Opened Carbon Nanotubes at 77 K. *The Journal of Physical Chemistry B*, 104:6773, 2000.

[206] R. P. Feynman and A. R. Hibbs. *Quantum mechanics and path integrals*. McGraw-Hill, New York, 1965.

[207] L. M. Sesé. Feynman-Hibbs potentials and path integrals for quantum Lennard-Jones systems: Theory and Monte Carlo simulations. *Molecular Physics*, 85:931, 1995.

[208] Q. Wang and J. Karl Johnson. Phase equilibrium of quantum fluids from simulation: Hydrogen and neon. *Fluid Phase Equilibria*, 132:93, 1997.

[209] C. Chipot and A. Pohorille. *Free Energy Calculations: Theory and Applications in Chemistry and Biology*. Springer, 2007.

[210] N. Tchouar, F. Ould-Kaddour, and D. Levesque. Computation of the properties of liquid neon, methane, and gas helium at low temperature by the Feynman-Hibbs approach. *The Journal of Chemical Physics*, 121:7326, 2004.

[211] N. Tchouar, M. Benyettou, and F. Ould Kadour. Quantum computation of the thermodynamics, structural and transport properties of Lennard-Jones liquid systems: The Feynman-Hibbs approach. *Journal of Molecular Liquids*, 122:69, 2005.

[212] H. Tanaka, H. Kanoh, M. Yudasaka, S. Iijima, and K. Kaneko. Quantum Effects on Hydrogen Isotope Adsorption on Single-Wall Carbon Nanohorns. *Journal of the American Chemical Society*, 127:7511, 2005.

[213] A. V. A. Kumar, H. Jobic, and S. K. Bhatia. Quantum Effects on Adsorption and Diffusion of Hydrogen and Deuterium in Microporous Materials. *The Journal of Physical Chemistry B*, 110:16666, 2006.

[214] J. K. Johnson, J. A. Zollweg, and K. E. Gubbins. The Lennard-Jones equation of state revisited. *Molecular Physics*, 78:591, 1993.

[215] J. M. Zielinski, C. G. Coe, R. J. Nickel, A. M. Romeo, A. C. Cooper, and G. P. Pez. High pressure sorption isotherms via differential pressure measurements. *Adsorption*, 13:1, 2007.

[216] G. Marsaglia. Choosing a Point from the Surface of a Sphere. *The Annals of Mathematical Statistics*, 43:645, 1972.

Appendix A

Random Vector on the Surface of a Sphere

Marsaglia [216] presents several algorithms for generating a random point in the surface of a sphere, which may also be generalized to higher dimensions. These techniques are based on trial and rejection schemes and usually require generating more random numbers, uniform or normally distributed depending on the algorithm, than strictly necessary. In this work, another approach was used which works only for three dimensions.

First, the relationship between Cartesian (x, y, z) coordinates and spherical coordinates (r, θ, ϕ) is realized,

$$
\begin{aligned}
x &= \sin\theta\cos\psi, \\
y &= \sin\theta\sin\psi, \\
z &= \cos\theta,
\end{aligned}
\tag{A.1}
$$

where the constraint $r = 1$ was used. x, y and z are restricted to the surface of a unit sphere centered on the origin. Then the z-component is selected with uniform probability in the interval $[-1, 1]$

$$
z = 2\mathcal{R} - 1,
\tag{A.2}
$$

where $\mathcal{R}$ is a random uniform number in $[0, 1]$. This constrains the point to the intersection of the sphere with the plane at z, parallel to the $x - y$ plane, a circumference with radius s,

$$
s = \sqrt{1 - z^2}.
\tag{A.3}
$$

Now, the point is chosen with equal probability in the circumference by generating a

random angle t in the interval $[0, 2\pi]$,

$$t = (2\mathcal{R} - 1)\, 2\pi, \tag{A.4}$$

and the remaining vector components follow,

$$
\begin{aligned}
x &= s \cos t, \tag{A.5} \\
y &= s \sin t. \tag{A.6}
\end{aligned}
$$

This technique requires generating only two uniform random numbers but has the disadvantage of using the relatively expensive trigonometric functions.

Appendix B

Error Analysis for Phase Coexistence Properties

For the free energy calculations presented in Chapter 3 involving an integration along a path in (ρ, T, n) space, the statistical error on the final state was estimated by dividing the data obtained from each simulation on the path into 10 blocks of equal length, and obtaining a different estimate of f_c.

For the reference states of the fluid phase, the biggest contribution to the error of $f_{\text{ref,F}}$ is due to the integration along the series of 100 simulations in an isotherm that connect the state at $\rho^* = 0.1$ to $\rho^* = 1.0$. Further free energy calculations in (ρ, T, n) space will still contribute, but to a lesser degree.

For the reference states on the solid side, the biggest contribution to the error of $f_{\text{ref,S}}$ results from the application of the Frenkel-Ladd Einstein crystal method to a finite system. When extrapolating to infinite size, different values of free energy are obtained depending on the type of long-range corrections used: uniform, lattice or average. These differences are larger than the statistical uncertainties of each individual estimate. For the solid phase calculations, the average corrections are always used, and the associated error with the Einstein crystal method is estimated by $\delta f_c = \left| f_c^{\text{uni}} - f_c^{\text{fcc}} \right| / 2$, where f_c^{uni} and f_c^{fcc} are the extrapolations using, respectively, uniform and fcc lattice corrections.

In §3.7, the solid-fluid coexistence properties were obtained by determining, for each temperature and system, the intersection point of the two $\mu(P)$ curves, one for each phase. The first order expansion of $\mu_{\{S,F\}}$ around the intersection point is

$$\mu_{\{S,F\}} = \mu_{\text{coex}} + \left(\frac{\partial \mu_{\{S,F\}}}{\partial P} \right)_{\text{coex}} \times (P - P_{\text{coex}}), \tag{B.1}$$

where $\left(\partial \mu_{\{S,F\}} / \partial P \right)_{\text{coex}}$ is the slope of the $\mu_{\{S,F\}}(P)$ curves at $P = P_{\text{coex}}$. It is assumed that the greatest source of error in the location of this intersection point is the reference value of the free energies of each branch, i.e., that $P(V)$ is known accurately and that $f_c(V)$ is

affected only by a constant error, $\delta f_{\text{ref},\{S,F\}}$. Considering these assumptions and equation (3.56), a new estimate of the intersection point is obtained by shifting the $\mu(P)$ curves by these constants $\delta f_{\text{ref},\{S,F\}}$,

$$
\begin{aligned}
\mu'_{\{S,F\}}(P) &= \mu_{\{S,F\}}(P) \pm \delta f_{\text{ref},\{S,F\}} \\
&= \mu_{\text{coex}} + \left(\frac{\partial \mu_{\{S,F\}}}{\partial P}\right)_{\text{coex}} \times (P - P_{\text{coex}}) \pm \delta f_{\text{ref},\{S,F\}},
\end{aligned}
\tag{B.2}
$$

where the prime superscript is used to identify the new quantities after applying the error delta in the reference free energy.

The intersection point of these new, shifted, curves is obtained when $\mu'_S(P = P'_{\text{coex}}) = \mu'_F(P = P'_{\text{coex}}) = \mu'_{\text{coex}}$. Inserting equation (B.2) into this equality yields an expression for the change in the coexistence pressure due to a shift of the reference free energies of each phase,

$$
\delta P_{\text{coex}} \equiv P'_{\text{coex}} - P_{\text{coex}} = \frac{\delta f_{\text{ref},S} + \delta f_{\text{ref},F}}{\left| \left(\frac{\partial \mu_S}{\partial P}\right)_{\text{coex}} + \left(\frac{\partial \mu_F}{\partial P}\right)_{\text{coex}} \right|},
\tag{B.3}
$$

where the errors in f_{ref} are added together. Equation (B.3) is used to estimate the uncertainties in the coexistence pressure, δP_{coex}, for a given temperature and system. The error in the coexistence chemical potential follows from (B.2):

$$
\delta \mu_{\text{coex}} \equiv \mu'_{\text{coex}} - \mu_{\text{coex}} = \left(\frac{\partial \mu_{\{S,F\}}}{\partial P}\right)_{\text{coex}} \delta P_{coex} + \delta f_{\text{ref},\{S,F\}},
\tag{B.4}
$$

which gives two estimates of $\delta \mu_{\text{coex}}$ that should be consistent.

The error in the coexistence densities are then obtained from the $P_{\{S,F\}}(\rho)$ curves,

$$
\delta \rho_{\text{coex},\{S,F\}} = \frac{\delta P_{\text{coex}}}{\left| \frac{\partial P_{\{S,F\}}}{\partial \rho} \right|_{\text{coex}}},
\tag{B.5}
$$

where the denominator is the slope of the $P_{\{S,F\}}(\rho)$ curve at $P = P_{\text{coex}}$. The errors in the coexistence free energies and potential energies are obtained in a similar manner.

The previous analysis was performed at constant temperature. For the triple point parameters a change in the reference free energies will also result in a change in T^*_{tp}. For that reason, the error was estimated by explicitly shifting the free energies curves at low T^*, in each phase, up and down and separately, and repeating the calculations of §3.8 to obtain the triple point parameters. The statistical errors of these reference states were $\delta f^*_{\text{ref},F} \approx 0.0007$ on the fluid side and $\delta f_{\text{ref},S} \approx 0.002$ on the solid side, for all systems. The range of the different triple point temperatures, pressures, chemical potentials and densities obtained in this manner was used to estimate the uncertainties in these quantities, which are presented in Table 3.5.